Autonomous Mission Design in Extreme Orbit Environments

by

David Allen Surovik

B.S., Texas A&M University, 2011

M.S., University of Colorado, 2013

A thesis submitted to the

Faculty of the Graduate School of the

University of Colorado in partial fulfillment

of the requirements for the degree of

Doctor of Philosophy

Department of Aerospace Engineering Sciences

2016

This thesis entitled:
Autonomous Mission Design in Extreme Orbit Environments
written by David Allen Surovik
has been approved for the Department of Aerospace Engineering Sciences

_____
Prof. Daniel J. Scheeres

_____
Prof. Elizabeth Bradley

_____
Prof. Eric Frew

_____
Prof. Jay McMahon

_____
Prof. Nisar Ahmed

Date _____

The final copy of this thesis has been examined by the signatories, and we find that both the content and the form meet acceptable presentation standards of scholarly work in the above mentioned discipline.

Surovik, David Allen (Ph.D., Aerospace Engineering Sciences)

Autonomous Mission Design in Extreme Orbit Environments

Thesis directed by Prof. Daniel J. Scheeres

An algorithm for autonomous online mission design at asteroids, comets, and small moons is developed to meet the novel challenges of their complex non-Keplerian orbit environments, which render traditional methods inapplicable. The core concept of abstract reachability analysis, in which a set of impulsive maneuvering options is mapped onto a space of high-level mission outcomes, is applied to enable goal-oriented decision-making with robustness to uncertainty. These nuanced analyses are efficiently computed by utilizing a heuristic-based adaptive sampling scheme that either maximizes an objective function for autonomous planning or resolves details of interest for preliminary analysis and general study. Illustrative examples reveal the chaotic nature of small body systems through the structure of various families of reachable orbits, such as those that facilitate close-range observation of targeted surface locations or achieve soft impact upon them.

In order to fulfill extensive sets of observation tasks, the single-maneuver design method is implemented in a receding-horizon framework such that a complete mission is constructed on-the-fly one piece at a time. Long-term performance and convergence are assured by augmenting the objective function with a prospect heuristic, which approximates the likelihood that a reachable end-state will benefit the subsequent planning horizon. When state and model uncertainty produce larger trajectory deviations than were anticipated, the next control horizon is advanced to allow for corrective action — a low-frequency form of feedback control. Through Monte Carlo analysis, the planning algorithm is ultimately demonstrated to produce mission profiles that vary drastically in their physical paths but nonetheless consistently complete all goals, suggesting a high degree of flexibility. It is further shown that the objective function can be tuned to preferentially minimize fuel cost or mission duration, as well as to optimize performance under different levels of uncertainty by appropriately balancing the mitigation paradigms of robust planning and reactive execution.

Dedication

To my future robot overlords.

Acknowledgements

My path through graduate school doubtlessly would have been far less pleasant and productive without the outstanding guidance of my advisor Dan Scheeres; I thank him for his generosity with his time and advice, for his patience and understanding during my inevitable stumbles, and for simply having provided me with the opportunity to try in the first place. The remainder of my thesis committee also receive my sincerest thanks for their interest and insight regarding my research, as well as for immensely beneficial and encouraging discussions regarding my job search and career decisions.

This work also would not have been possible without the extremely generous support of the NASA Space Technology Research Fellowship, which not only kept me well-fed but also sent me all over the world to talk about space robots with other ~~nerds~~ scholars. NASA employees Chris D'Souza, Steve Broschart, and Shyam Bhaskaran all proved to be effective and relentlessly friendly mentors, and the Rosetta shadow navigation team were simply a pleasure to work with.

My deep appreciation also goes out to the many motley members of CSML for tons of useful advice and ideas, and for keeping me just the right amount sane through a combination of solidarity and indefatigable goofiness — if you're reading this, congratulations on beginning your dissertation, but I'd advise you to reference a better example than mine.

I also must thank AK, CL, LB, SK, and SAG for further camaraderie and emotional support in matters of every kind and for just making my life richer and altogether more fun. Lastly and most fundamentally of all I want to thank my family, who have always believed I could do anything, but who I know would always love and support me even if I never managed to prove them right.

Contents

Chapter

Bibliography   **117**

Appendix

Tables

Table

Figures

Figure

Chapter 1

Introduction

1.1 Motivation

Asteroids and comets pose numerous opportunities and threats that motivate their increasing focus as space exploration destinations. Being composed of pristine material from the early ages of the solar system, these small celestial bodies contain vital clues about the formation of the planets and the origins of organic compounds and other necessary ingredients for life. Their stores of water, precious metals, and other natural resources could alternatively be exploited for the development of space infrastructure, such as refueling stations, or for use on Earth. Of more pressing concern is the threat of impact posed by near-Earth objects, whose potential for devastation is evidenced by the recent Chelyabinsk event, the Tunguska event, and extinction events in the fossil record.

Interest in these two classes of objects has thus far resulted in several planetary science missions including flybys, impactors, rendezvous, touch-and-go sampling, and soft landing. The first successful rendezvous with a small body was conducted by NASA's NEAR-Shoemaker spacecraft at asteroid Eros in 2000; the craft also executed a soft landing, though this was not part of the designed science operations [1]. Material sampling was first achieved in 2005 by JAXA's Hayabusa spacecraft at asteroid 25143 Itokawa [2]. In 2011, NASA's Dawn spacecraft rendezvoused with the large asteroid 4 Vesta, beginning a protracted period of extensive study, and Roscosmos launched an unsuccessful sample-return mission to the small Martian moon Phobos. The first comet rendezvous and landing were achieved in 2014 by ESA's Rosetta spacecraft and its lander Philae at Comet 67/P Churyumov-Gerasimenko (hereafter termed 67/P) [3].

Sustained interest in these classes of objects is evidenced by JAXA's recently-launched Hayabusa 2 mission and NASA's soon-to-launch OSIRIS-REx mission, both of which will conduct rendezvous and touch-and-go sampling at asteroids. The AIDA mission concept, a joint effort between ESA and NASA that would entail rendezvous with a binary asteroid and assessment of a kinetic impactor's deflective capability, is currently undergoing extensive study [4]. Two of the five semifinalist proposals for NASA's 13th Discovery-class mission would visit asteroids, while a third would survey the Solar System to discover as-yet unknown hazardous objects; several other submitted proposals also targeted small bodies. Whether for the ultimate purpose of study, exploitation, or mitigation, missions to these objects would benefit greatly from an enhanced ability to conduct operations at close proximity.

1.1.1   Conventional Methods

Traditional approaches to space mission design are rooted in Kepler's discovery that orbiting bodies travel along conic sections with the central gravitating body positioned at one focus. The integrability of Keplerian motion allows for any orbital state to be immediately associated with its conic section, an easily-described one-dimensional path through the six-dimensional orbit state space. Of these unchanging orbits, which compose the entirety of possible ballistic motion, a small number can then be selected and pieced together using impulsive thrust maneuvers to take a spacecraft from one desired state to another.

In many scenarios, the difference between the actual dynamical environment and the ideal Keplerian approximation — where the only force is that of a spherical or point-mass central body's gravity — is relatively small. For example, Earth's polar radius and its equatorial radius differ by only about 1%, and the gravitational pull of the moon is a dozen orders of magnitude lower than that of the Earth for a geosynchronous satellite. For most Earth-orbiting missions, the shape and orientation of the osculating conic changes only gradually and can be adequately accounted for via linear perturbation methods and averaging theory. This further assures that a "safe" orbit, i.e., one that does not impact the central body, will remain safe over a long time horizon and that all other

states on the osculating conic will be closely approached in the near future. During preliminary design of interplanetary missions a "patched conic" approach, where each leg of the journey is modeled as a Keplerian problem with a different central body, can be applied effectively. These approximations are sufficiently accurate such that a higher-fidelity solution appropriate for use in an actual mission can later be obtained from a differential correction process.

1.1.2   Unconventional Aspects

However, missions geared to the close study of small celestial bodies such as asteroids and comets face constant exposure to strong perturbations away from Keplerian motion, driven by highly nonspherical gravity fields produced from irregular mass distributions as well as proportionally significant effects of third-body gravitation and solar radiation pressure (SRP). These conditions generally result in rapid divergence of true motion away from conic section approximations, which are thus no longer an apt basis for even short-term trajectory prediction [5, 6]; as a result, traditional mission design methods can no longer be applied effectively. No longer remaining near a simple one-dimensional manifold, chaotic behavior arises that can lead the spacecraft across diverse dynamical regimes in an unintuitive and highly nonperiodic manner. Combined with an associated high sensitivity to error, this makes accurate long-term predictions impossible and introduces the risk that off-nominal conditions could rapidly result in mission failure.

Consequently, past asteroid rendezvous missions NEAR-Shoemaker and Hayabusa were conducted primarily in more distant orbits with longer stability horizons; forays into dangerous close-proximity regimes for high-value operations were brief, exhaustively planned, and comparatively fuel-intensive [2, 7]. Likewise, the lowest orbit radius of Rosetta during its nominal mission was about five times larger than the max radius of the central body — close-study was the purview of its lander, Philae, which was deployed on a high-energy landing trajectory in order to minimize the influence of non-Keplerian forces. This mission paradigm of thorough and conservative preparation for a single critical task will be repeated in the approaching OSIRIS-REx mission for a single touch-and-go sampling task [8].

Unfortunately, despite the weak nominal accelerations present at small bodies, the fuel cost of continually overpowering the natural dynamics to simplify trajectory design can become excessive for longer-duration close-proximity operations [6, 9]. This motivates the leveraging of the natural system dynamics in order to enable ambitious mission concepts, a prospect that would require extensive tool development for accurately and rapidly exploring the complex mission design space and identifying efficient and innovative trajectories [10]. Consequently, a need for advanced trajectory design tools and GNC capabilities to meet the challenges of these complex and unintuitive regimes is well-recognized [11]. As will be discussed later, this capability might have benefitted the design of the deployment trajectory for the Philae lander, whose energetic touchdown resulted in a large rebound and ultimate landing at an unfavorable distant location after energy dissipation and anchoring systems failed.

1.1.3   Modern Trends

Due to the high cost and latency of remotely operating an interplanetary mission from Earth, an autonomous online implementation of such design techniques is highly desirable [12]. Problems encountered by the Hayabusa mission illustrate the drawbacks of insufficiently developed autonomous capabilities — its touch-and-go sampling operation met limited success, returning far less material than planned, while an unexpected interaction between autonomous and human-issued commands resulted in the deployed science package MINERVA escaping the system rather than landing as intended [2, 13]. Improved autonomy could help prevent such mishaps while alleviating much of the the frequent operational demands upon interplanetary communication systems and human navigators. Additionally, improved mission returns could be obtained by enabling expedient pursuit of unforeseen scientific opportunities in an "agile science" paradigm [14].

Perhaps most fundamentally, heightened autonomy could bolster abilities to mitigate rapid error growth in a timely and effective manner, a prospect reflected by the growing trend toward computational techniques for guidance and control. By replacing feedback control policies that track a reference trajectory with more algorithmic procedures that re-solve the trajectory design problem

online, unprecedented performance and capability can be achieved. Such computational guidance techniques have recently been formulated for astrodynamics applications such as aerocapture [15, 16], powered descent [17, 18], and station keeping [19].

1.2   Academic Context

Several academic fields have developed techniques and explored applications that have deep connections to the problem of autonomous small body mission design. In nonlinear control, policies are formulated for tracking reference trajectories in systems with complicated dynamics and uncertainty, often with provable guarantees of stability and convergence as well as optimality with regards to a prescribed weighting of costs. More general problem definitions are addressed in robotics and AI planning, where paths are sought through configuration space representations in order to identify a suitable reference trajectory for a controller to follow. Goal states may also be more abstractly defined, and assessments of performance are frequently conducted empirically rather than mathematically, by necessity.

In astrodynamics and dynamical systems theory, the inherent dynamical structures within certain non-Keplerian systems have received extensive study along with development of techniques for their exploitation, though small body systems have thus far received less such attention and are not as conducive to highly generalizable results due to the large variety of irregular shapes that occur. Analysis techniques for these problems have also been applied that focus on outcomes with complicated relationships to the physical state in order to inform preliminary system analysis and trade-space mission design decisions.

However, these various ingredients have never before been synthesized into the type of tool that is presented in this dissertation. This section will examine relevant contributions from each related field in order to identify the aspects of the problem that can be addressed with adaptations of, or ideas from, existing work.

1.2.1   Receding Horizon Control

After a sufficient level of complexity is reached, many control problems are simply infeasibly large to solve in their entirety during online execution — the control sequence necessary for reaching the reference state might be inordinately complicated, the time span over which control is required might be long or unbounded, and computations must be frequently re-evaluated to mitigate dynamic disturbances and state uncertainty. A common recourse to these obstacles is to instead solve a temporally truncated version of the problem, optimally closing the distance to the desired state over a limited time span. This approach to reducing complexity is known as receding horizon control (RHC) or model predictive control.

Beyond its origins for regulatory control in the process industry, the advent of affordable and capable microprocessors has resulted in RHC rapidly gaining attention as an approach for controlling fast and sensitive dynamical systems [20]. Examples include highly dynamic planning problems in complex flow fields, namely those experienced by autonomous underwater and aerial vehicles due to complex ocean currents, winds, and thermal updrafts [21, 22]. It is also being studied as a tool for related high-sensitivity astrodynamics applications such as low-thrust interplanetary mission design [23], proximity operations [24], and control of swarms of spacecraft [25].

Naturally, its applicability to sensitive systems also makes RHC effective for mitigating high levels of error and nondeterminism — a trait that has been leveraged for robust spacecraft rendezvous [26] and robust nonlinear control in general [27]. The approximately impulsive nature of chemical rocket propulsion further increases the applicability of RHC to the small body spacecraft control problem by naturally creating discrete control horizons; longer horizons, i.e., less frequent maneuvers, would increase the reachability of objectives in proportion to the size of the control domain. Such a paradigm would leverage the system's unique natural dynamics rather than constantly expending operational effort to overpower them.

1.2.2   Robotics and AI Planning

Many fundamental aspects of vehicle motion planning stem from applications of autonomous ground and air vehicles that involve spatiotemporally consistent system dynamics. In these relatively simple scenarios, two positions can be linked by a straight line and statically defined goals and obstacles can be charted on a "roadmap", allowing for the path planning problem to be discretized as a graph of connections between waypoints. Favorable paths through the configuration space may then be identified using any of a wide variety of graph-search methods such as A^* or sampling schemes like Rapid Random Trees before applying trajectory smoothing to satisfy nonholonomic and differential constraints in the full, continuous system [28, 29].

More tenuous and complicated scenarios often call for application of the receding-horizon concept to the path planning problem. For ground vehicles operating in dynamic and uncertain environments, receding-horizon planning can be used to manage the growth of error in the predicted movement of obstacles by routinely re-planning safe motion over a limited time span [30, 31]. It has also been applied to mitigate computational complexity arising from time-varying logical specifications such as compliance with traffic laws and other context-dependent constraints on system behavior [32].

Another useful tool in controlling complex systems is abstraction, where cumbersome details are simplified or otherwise hidden away in a system representation such that high-level objectives may be pursued more directly. This has proved useful for regulating economic output measures, rather than state variables, in RHC for industrial processes [33]. By taking a broad view of the problem, abstraction also removes arbitrary distinctions between different solutions, thus reducing the solution set and simplifying the search problem. This benefit is evident in the path planning of robot swarms, where a specified size or centroid of the swarm could be attained by a broad family of individual position combinations and robot permutations [34]. In the highly-connected configuration space of a small body orbiter, abstraction could prove an apt idea for sidestepping arbitrary decisions such as sequencing and direction of motion during pursuit of multiple objectives.

Abstraction can also benefit path planning applications by hiding the dynamically complex intermediary details in a special representation of the problem, thus reducing computational burden. For example, by classifying thermal updrafts in a roadmap-like representation of a wind field, soaring UAVs may successfully leverage graph or tree search methods to pursue goal states [35] or information gathering objectives [36] more effectively than is possible with a higher-detail, shorter-horizon planning method.

1.2.3 Non-Keplerian Mission Design

Inherent to orbit mechanics is a spatio-dynamic relationship that is strong relative to the availability of control energy in most circumstances. In other words, uncontrolled motion can lead to a wide variety of system configurations and typically serves as an important component of the path planning problem. Mission design for strongly non-Keplerian systems such as the much-studied circular restricted three-body problem (CR3BP) thus frequently hinges upon accurate knowledge of natural periodic orbits that sparsely populate the phase space — these structures are the most feasible resource for planning long-term motion. Given this knowledge, transfers from one body to another at low control costs can be formulated by exploiting the intersections of the stable and unstable manifolds eminating from initial and final periodic orbits [37, 38] or of the low-thrust-reachable sets stemming from those manifolds instead [39].

Automated techniques have been extensively used for preliminary design of certain classes of missions in non-Keplerian systems, such as gravity assist flyby sequences for interplanetary missions obtained via Monte Carlo tree search [40] and genetic algorithms [41]. The latter technique has also briefly been investigated for small body mission design under some simplifying assumptions [42]. More elaborate low-energy transfer sequences can be found via search algorithms designed specifically for the well-characterized CR3BP, leveraging either analytically-based rules of thumb [43] or a precomputed database of orbits and manifold intersections, which can be modeled as waypoints and connections in a graph search [44]. This strategy has also been modified for realtime implementation by more coarsely discretizing the database of connections between state space

regions, which serves in tandem with a heuristic to ease the computational cost of searching for a solution, and then refining the resultant transfer sequence to higher fidelity via differential correction [45].

All of these applications, however, require separate tools or knowledge solving each individual leg of the problem, i.e., either precomputed solutions to sub-problems or lots of computing resources (time or power) for solving them. Moreover, they are formulated to target specific final states or orbits, which does not readily accomodate the aforementioned process of abstraction for defining high-level objectives. This could potentially be achieved by pairing the graph-based method with a framework for associating periodic orbits with higher-level goals, but this problem itself would be highly nontrivial, would not account for phasing requirements, and might be hindered by limited existence of such orbits close to the body surface. Thus, although automation of mission design is demonstrated, the specific methodologies might not translate effectively to the problem of close-proximity operations at small bodies.

1.2.4   Design-Space Mapping and Analysis

Exhaustive design-space analysis has long been common recourse to design questions with non-integrable relationships between parameters and costs/objectives. Key decisions can be repre-sented by a "map" between a small number of design variables and one or more associated output measures. When visualized, this data product can greatly facilitate human comprehension for high-level cost/benefit analysis and other insights about the nature of the system.

As nominal trajectories are conventionally designed in full long before a space exploration mission is even launched, this computationally intensive approach has frequently been applied to astrodynamics problems. Perhaps the best known example is the "porkchop plot", which relates two highly influential mission variables — the dates at which the origin is departed and at which the target is reached — to the energy costs necessary for completing an orbit transfer, which are obtained by Lambert's method or another solution technique. However, design-space mapping is also useful for informing many other decisions. In the three-body problem, "periapse maps" chart

the physical locations of close passes achieved by families of low-energy trajectories that pass near one of the bodies [6], which is useful for applications such as ballistic landing on binary asteroids [46]. Alternately, low-energy transfers from one body to another can be designed by parameterizing the domain in terms of the arrival conditions at a target periodic orbit and checking the backward-propagated periapse altitude at the departure body [37]. Mapping can also illuminate other system properties such as stability and divergence [47, 48, 49] and even transport rates between nearly-invariant sets, e.g., regarding the asteroid population in the Sun-Jupiter system [50].

Conceptually simple but analytically intractible outcomes such as impact and escape have also been charted for subsets of initial conditions in the CR3BP [51]. By defining this subset purely in terms of velocity, this analysis has been used to represent reachable outcomes for a spacecraft at a specific initial state with the ability to execute a single impulsive maneuver [52]. Reachability analysis has previously received relatively little use in astrodynamics, as it is most appropriate for more temporally-constrained scenarios rather than preliminary design. However, mathematical studies of reachability under Keplerian dynamics have been conducted for informing certain operations for missions that are already underway. These have included missile interception [53], fuel-limited rendezvous and conjunction avoidance [54, 55, 56], and object correlation with unobserved maneuvers under general dynamics [57].

While exhaustive and computationally burdensome grid-based sampling is the norm for mapping nonintegrable design spaces, several of the aforementioned examples have sought to reduce this cost with tools such as adaptive mesh refinement and clustering [48, 49, 50, 52]. Indeed, sampling-based approaches to robot motion planning could be viewed as numerically efficient reachability analysis tools [28, 58, 59], albeit applied directly to the configuration space in most cases. This suggests that existing automated search techniques could be useful in the context of design-space analysis for orbital trajectory design.

1.3   Contributions and Outline

Thesis Statement: *In order to achieve sets of abstract mission objectives at **strongly non-Keplerian small-body systems** with uncertainty, tools and concepts from **AI and robotic motion planning** are leveraged to conduct efficient automated search and analysis of the **abstract reachability map** for designing individual spacecraft maneuvers sequentially in a **receding-horizon** scheme.*

1.3.1   Research Overview

Trajectory design is in essence re-posed as a control problem in which the reference to be tracked is the output of multiple layers of abstraction — the system is a mission that must be driven from "incomplete" to "complete". The plant consists of a robust predictive model that translates prospective control inputs into conservative estimates of high-level outcomes under characteristic uncertainty levels. Because of the non-analytic nature of the model, the control law is computational, consisting of a heuristic search method applied to the abstract reachability map that relates the full control domain to a decision variable. This law selects and implements a single impulsive control input that is predicted to produce preferable behavior over a limited time horizon; however, this short-term progress is also balanced against heuristic-assessed long-term prospects in order to improve convergence to mission completion and reduce net costs.

1.3.2   Expanded Reachability Concept

Reachability maps have recently been applied to chart properties such as divergence rates and safety status in the CR3BP [51, 60, 48]. In order to produce a more comprehensive analysis suitable for informing mission operations, the approach is expanded in this dissertation and associated publications [61, 62] to also include more general mission outcomes including goal fulfillment and performance measures that govern automated planning. Further, divergence rates are combined with initial uncertainty levels to ultimately provide thresholds of robustness to error, in terms of safety and goal outcomes alike. These increasingly abstract outputs are described in Chapter 2 along with an appropriate selection of small-body mission scenarios and their physical dynamics.

A formal description of the reachability map concept is given in Chapter 3; control domains in both 2D and 3D, some of which include a timing parameter, are also detailed along with ways of effectively visualizing the data for use in preliminary mission design or in the development and calibration of online planners. To tie the reachability concept back to the well-trodden territory of two-body orbit dynamics, analytical reachability solutions are derived and plotted for some outcomes under Keplerian motion about a finite spherical body. Lastly, fundamental similarities and differences between the characteristics of Keplerian and non-Keplerian maps are illustrated.

1.3.3 Partitioning and Searching Maps

The basic anatomy of the numerical reachability analysis method applied in this dissertation is inherited from one of the aforementioned studies of the CR3BP. This previously applied technique approximated the continuous map by sampling discrete points from the domain and constructing a mesh to allow inference of results across finite areas. For numerical efficiency, this mesh was adaptively refined by successively conducting additional sampling at regions identified by a heuristic as most relevant to the desired data product. By applying a mesh element area-based heuristic, an uneven sample of initial conditions was produced such that final conditions had a roughly uniform distribution [48]; impact and escape regions were later delineated by instead using mesh edge-based heuristics [60, 52].

A full description of this component and the numerous improvements and extensions relative to the preexisting incarnation are given in Chapter 4 and publications [61, 63]. Runtimes were first drastically improved by a fresh and careful implementation of the method via a combination of C++ and Matlab, allowing 3D analyses to be conducted at usefully high resolutions under reasonable compute times. Increased sophistication of the heuristic refinement process was developed to facilitate efficiency not only for the previous application of partitioning maps for visualization, but also for alternate usage in rapidly locating the maximum of an objective function during online planning. This was achieved through volume-wise weight renormalization of the simplex set along with the leveraging of concepts such as gradient climbing and simulated annealing.

1.3.4   Applications of Single-Horizon Analysis

Enabled by the efficient search and partitioning techniques, diverse types of reachability analyses are conducted in Chapter 5 to illustrate potential applications, also represented in publications [61, 64]. These include close-range observations; landing prospects in terms of location, speed, and impact angle; and attainment of periodic motion for routine observations or holding patterns. Of additional interest are time-parameterized planning domains as well as phase space divergence/chaoticity rates, paramount for predicting error growth.

1.3.5   Receding-Horizon Framework

Completion of extensive goal sets generally requires sequences of many spacecraft maneuvers, each individually designed with the tools discussed above. However, a naive receding-horizon control law that only considers short-term outcomes could converge unreasonably slowly and impair long-term performance. Chapter 6 relates work done in publications [63, 65, 66] to address these pitfalls by constructing a decision function that balances short-term achievements against long-term prospects, which are represented by a heuristic that operates on control-horizon end states similarly to "cost-to-go" functions that are commonly used to ensure stability and convergence in nonlinear control. Formulating effective heuristics is eased by the high level of phase-space connectivity, which allows diverse regions to be accessed and large swathes of outcomes to be achieved under a single control input.

In complement to the degree of robustness ensured by the single-horizon planning process, uncertainty mitigation is bolstered by a "reactivity" paradigm. When the online estimated value of deviation exceeds the degree of robustness of the nominal trajectory, the algorithm reacts by implementing another control input ahead of schedule. This receding-horizon scheme amounts in essence to low-frequency closed-loop tracking of a manifold defined by abstract goals.

1.3.6   System Analysis

Properties, behaviors, and performance of the autonomously controlled system are analyzed in Chapter 7 and publications [66, 67]. These traits are first assessed in terms of variation in the physical system and the mission requirements to reveal a transition from determinism to stochasticity as the plant becomes increasingly complex. The uncertainty mitigation paradigms of robustness and reactivity are then compared, along with variation of the level of error itself to help reveal the limits of the automated planner. Finally, alternate formulations of the decision function are used to demonstrate the increased performance and reliability provided by prospect heuristics as well as the capacity to reduce total mission cost in terms of fuel and duration.

1.3.7   Project Summary

After prescription of appropriately formulated mission scenarios, implementation of the trajectory planning scheme comprises two categories of tasks. The conceptual framework corresponds to a set of diverse software tools whose development and synthesis had to be undertaken in a computationally efficient manner. With this foundation in place, the assurance of high-quality mission solutions hinges upon careful design of heuristics both for increasing the effectiveness of the reachability search within each control horizon and for modifying the decision function in a manner that bolsters long-term performance. The successes, limitations, and future avenues of inquiry resulting from this research effort are detailed in Chapter 8 to conclude the dissertation.

1.3.8   Contribution Summary

The ultimate contribution of this dissertation is the synthesis of a diverse set of tools and concepts into a unified approach to mission design and online mitigation of error. Viability of this method stems from the synergistic interactions of its constituent parts in the specific context of the intended application, whereas each on its own might appear untenable. For example, the receding-horizon planner converges in large part thanks to the high degree of connectivity of goal regions via uncontrolled motion through the phase space, which is attributable to the combination

of non-Keplerian orbit dynamics with the abstraction of goal definitions; RHC planning would appear less sensible as a method of reaching a pre-defined science orbit or trajectory. The control scheme of intermittent, impulsive maneuvers was simultaneously sufficient for taking full advantage of this connectivity — thanks to the low cost of imparting proportionally large effects at low-mass bodies — and low-dimensional enough to counterbalance the complexity of the dynamics and make the computational demands of sampling-based reachability analysis surprisingly feasible.

As further development continues for more conventional small body operational strategies such as hovering [68, 69, 70] and stabilizing frozen orbits [71, 72], it is intended that the reachability-based receding-horizon planning method presented here and in publications [61, 62, 63, 64, 65, 66, 67] provides an initial demonstration of an alternative approach to mission design and online execution for efficiently fulfilling ambitious science objectives in these challenging systems.

Chapter 2

Predictive Model

Central to the sampling-based planning scheme is a predictive model that, provided a control input, can be numerically propagated to determine the outcome in terms of high-level mission objectives and requirements. The model consists of three different stages that each handle conceptually distinct questions about the system behavior:

(1) Where does the spacecraft travel through physical space?

(2) What are the mission-level consequences of the trajectory?

(3) How favorable or unfavorable are those consequences?

The first question is answered by the physical dynamics of the system and the second by the mission formulation; the answer to the third is not prescribed but rather must be designed. Each model stage will be detailed in the following three sections.

2.1   Physical System

First and foremost, the physical dynamics of the system are of pivotal importance given that the control philosophy applied is to leverage natural motion rather than laboriously overpower it. After normalizing by its mass, the evolution of the spacecraft's position $\mathbf{r} = (x, y, z)$ and velocity $\dot{\mathbf{r}}$ are described in terms of a set of accelerations $\mathbf{a}_i$.

$$\ddot{\mathbf{r}}(\mathbf{r}, \dot{\mathbf{r}}, t) = \sum \mathbf{a}_i(\mathbf{r}, \dot{\mathbf{r}}, t) \tag{2.1}$$

Explicit dependence upon time, i.e., non-autonomous dynamics, is necessary when modeling non-synchronous forces such as solar radiation pressure and general third body gravitation.

2.1.1   Reference Frame

In general, most forces, science objectives, and safety constraints depend on the body-relative state of the spacecraft. Expressions for these values are then most naturally expressed in a body-fixed frame. As is an accurate approximation for the considerable majority of small body systems [6, 73], the frame applied here reflects a minimum-energy rotation state, where the body has constant angular velocity $\boldsymbol{\omega} = \omega\hat{\mathbf{z}}$ oriented about its axis of greatest inertia. This frame rotation is accounted for by centripetal and coriolis accelerations, combined into a single acceleration term:

$$\mathbf{a}_{frame} = -\,\boldsymbol{\omega} \times (\boldsymbol{\omega} \times \mathbf{r}) - 2\boldsymbol{\omega} \times \dot{\mathbf{r}} \tag{2.2}$$

2.1.2   Full Body Gravity

Other than in the case of planetary satellites, non-Keplerian motion near small bodies generally arises most strongly and with the most nuance from the body's irregular gravity field. This acceleration depends not only on the gravitational parameter μ and the distance to the body's center of mass, but also heavily upon its mass distribution and relative orientation. Traditionally, spherical harmonic expansions are the most common approach to modeling irregular gravity; however, this infinite series approximation is only convergent for orbit radii that are larger than that of the body's highest peak. Accordingly, two alternate closed-form descriptions are used to allow accurate results during close-proximity operations.

2.1.2.1   Triaxial Ellipsoid

As the simpler of the two alternatives, the uniform-density triaxial ellipsoid model requires only three additional parameters beyond the standard gravitational parameter μ: the ellipsoid's principal radii α, β, and γ. This can be used to model a highly elongated body, but nonetheless implies symmetry about three planes. Such an approximation is sufficiently accurate for early-stage

design at roughly ellipsoidal bodies such as Phobos and 1999 KW4 Alpha/Beta, but is a poor match for others like "dog bone" shaped asteroid Kleopatra and sharp-angled asteroid Golevka. Contact binaries like 67/P can be somewhat closely approximated as two ellipsoids; others like Itokawa would suffer larger errors due to the proportion of mass in the "neck" region, the contact point between the two distinct lobes.

The triaxial-ellipsoid gravitational potential $U_{triax}(\mathbf{r}; \alpha, \beta, \gamma)$, acceleration $\mathbf{a}_{triax} = \nabla U_{triax}$, and Jacobian $\nabla^2 U_{triax}$ can all expressed in closed form by elliptic integrals, which can be evaluated for any location external to the body surface via a standard numerical recipe [6, 74]; further details may be found in Appendix A.1. Altogether, the triaxial model is sufficient for the purpose of demonstrating the relationship between highly nonspherical mass distribution and non-Keplerian dynamics at a fundamental level without incurring large computational expenses.

2.1.2.2   Polyhedron

Far greater accuracy and generality can be achieved by instead using a uniform-density polyhedron as the shape model, making it invaluable for thorough preliminary design as well as for online planning at non-ellipsoidal bodies. This model describes a closed body surface using a set of triangular facets, generally derived from sets of photographs of the object from many angles. The gravitational potential $U_{poly}(\mathbf{r}; \mathcal{P}_\nu)$, acceleration $\mathbf{a}_{poly} = \nabla U_{poly}$, and its Jacobian $\nabla^2 U_{poly}$ are computed from a polyhedral shape model $\mathcal{P}_\nu$ defined by a set of ν vertices and $2\nu - 4$ faces under an assumption of constant density and total gravitational parameter μ [6]; further details may be found in Appendix A.2.

However, as numerical operations must be performed for each individual polyhedron element, the computational burden becomes much higher than that of the triaxial ellipsoid model at resolutions ν that are large enough to provide a useful level of accuracy. Other potential shortcomings include the assumption of homogeneous density — likely untrue especially for rubble pile asteroids — and the proliferation of parameters making dynamic estimation infeasible.

2.1.3 Third Bodies and SRP

The influence of tidal accelerations $\mathbf{a}_{3B}$ from the parent body ranges from significant for near-Earth asteroids to dominant for close-orbiting planetary satellites, and is given in terms of the primary's gravitational parameter μ_{3B} and body-frame position $\mathbf{r}_{3B}$ by

$$\mathbf{a}_{3B}(\mathbf{r}, t) = -\mu_{3B}\left(\frac{\mathbf{r} - \mathbf{r}_{3B}}{|\mathbf{r} - \mathbf{r}_{3B}|^3} + \frac{\mathbf{r}_{3B}}{|\mathbf{r}_{3B}|^3}\right) \tag{2.3}$$

For tidally locked natural satellites, the mean motion n of the orbit about the primary body is synchronous with the rotation rate and $\mathbf{r}_{3B}$ is constant. Otherwise, $\mathbf{r}_{3B}(t)$ is found by applying the rotation matrix $C_{BO}(t)$ to the value $\mathbf{r}_{3B,O}$ as defined in the frame of the central body's orbit about the third body.

$$\mathbf{r}_{3B}(t) = C_{BO}\left([\boldsymbol{\omega} - n\hat{\mathbf{z}}]\, t\right)\mathbf{r}_{3B,O} \tag{2.4}$$

Similarly, the matrix $C_{BN}(t)$ rotates the inertial Sun-pointing vector $\hat{\mathbf{r}}_{S,N}$, which is approximated as constant over time scales of interest, into its body-frame expression $\hat{\mathbf{r}}_S(t)$ for use in the statement of the acceleration due to SRP $\mathbf{a}_{SRP}(t)$. This term's magnitude a_{SRP}, which depends on spacecraft characteristics and the distance to the Sun, is significant at small near-Earth asteroids and may be approximated as constant if the spacecraft is assumed to keep its solar arrays Sun-pointing as often as possible.

$$\hat{\mathbf{r}}_S(t) = C_{BN}\left(\boldsymbol{\omega}t\right)\hat{\mathbf{r}}_{S,N} \tag{2.5}$$

$$\mathbf{a}_{SRP}(t) = -a_{SRP}\hat{\mathbf{r}}_S(t) \tag{2.6}$$

2.2 Abstract Outcomes

The second stage of the model interprets the physical motion through phase space in terms of mission-level outcomes $\mathbf{y}$. These values reflect compliance with sets of operational bounds for safety, practicality, and science activities, along with other intermediary measures that may be used as ingredients in the objective function governing autonomous decision-making. Each element y_i

can be either real-valued or Boolean, and can depend on the time history $\tilde{\mathbf{x}}(t)$ of the state via, e.g., an integrated value or a maximum taken over some time span.

2.2.1   Safety Constraints

Crucially, impact of the central body must be avoided unless it is part of a prescribed science activity. This Boolean failure criteria, `Impact`, is detected by checking whether the spacecraft position is interior to the central body $\mathcal{B}$.

$$\texttt{Impact} = (\mathbf{r} \in \mathcal{B}) \tag{2.7}$$

$$= \begin{cases} \left(\frac{x^2}{\alpha^2} + \frac{y^2}{\beta^2} + \frac{z^2}{\gamma^2} \leq 1\right) & \text{if } \mathcal{B} = \mathcal{B}(\alpha, \beta, \gamma) \\ \left(\nabla^2 U(\mathbf{r}) == 4\pi\right) & \text{if } \mathcal{B} = \mathcal{B}(\mathcal{P}) \end{cases} \tag{2.8}$$

For a real-valued indicator of impact risk, the altitude is also tracked:

$$\rho_{\mathcal{B}} = \min \rho(\mathbf{x}, \mathcal{B}) \tag{2.9}$$

This denotes the shortest range to any point on the triaxial ellipsoid or polyhedron $\mathcal{B}$.

Though not strictly critical from a safety perspective, it is generally practical to remain relatively close to the central body so that the science objectives are kept within reach. A second Boolean failure criteria introduced to reflect this is termed `Escape`; however, it does not correspond to escape in the Keplerian sense since it cannot be determined *a priori* whether a trajectory will return to the body vicinity in finite time. Instead, a simple orbit radius bound r_{esc} is enforced:

$$\texttt{Escape} = \left(\mathbf{r} \cdot \mathbf{r} > r_{esc}^2\right) \tag{2.10}$$

This usefully allows motion to be permitted for short durations in regimes that could conceptually be classified as escaping, e.g., beyond Phobos' Hill sphere, which lies quite close to the body surface. Conversely, orbits that appear bounded over long time spans but stray far from the central body before returning can be excluded as impractical.

2.2.2   Objectives

Counter to the Boolean failure criteria above, which must always evaluate to false, objectives are posed as real-valued variables y_i to be maximized. Three categories of objectives are studied, the first two of which represent commonly desired science activities while the third serves as an extension of an operational tactic more traditionally studied for non-Keplerian missions.

2.2.2.1   Close-Range Imaging

For the bulk of the study of the autonomous planning algorithm, goal fulfillment is modeled as the accumulated time spent satisfying geometric and phasing conditions prescribed for imaging points of interest (POI) $\mathbf{R}_i$ on the body surface. Each i'th observation task — multiple tasks may share a target — is defined as the simultaneous fulfillment of upper (a^+) and lower (a^-) bounds of several measures $a(\mathbf{x}; \mathbf{R}_i)$ for a duration Δt_g. These comprise the spacecraft's target-relative range ρ_i, co-elevation θ_i, azimuth φ_i, and solar phase angle ψ_i, all of which are computed from the target-relative position $\boldsymbol{\rho}_i = \mathbf{r} - \mathbf{R}_i$ as

$$\rho_i(t) = \sqrt{\boldsymbol{\rho}_i(t) \cdot \boldsymbol{\rho}_i(t)} \tag{2.11}$$

$$\theta_i(t) = \cos^{-1}(\hat{\boldsymbol{\rho}}_i(t) \cdot \hat{\mathbf{u}}_i) \tag{2.12}$$

$$\varphi_i(t) = \tan^{-1}\left[\frac{\hat{\boldsymbol{\rho}}_i(t) \cdot \hat{\mathbf{e}}_i}{\hat{\boldsymbol{\rho}}_i(t) \cdot \hat{\mathbf{n}}_i}\right] \tag{2.13}$$

$$\psi_i(t) = \cos^{-1}(\hat{\boldsymbol{\rho}}_i(t) \cdot \hat{\boldsymbol{\rho}}_s(t)) \tag{2.14}$$

where $(\hat{\mathbf{e}}, \hat{\mathbf{n}}, \hat{\mathbf{u}})_i$ are the east-north-up basis vectors of the target's local frame.

For successful observations to occur, all observation sub-measure bounds must be satisfied simultaneously, i.e.,

$$\texttt{Imageable}_i = \left(a^- < a(t) < a^+\right) \ \forall \ a \in \{\rho, \theta, \varphi, \psi\}_i \tag{2.15}$$

This must be sustained for a duration Δt_g, after which point the observation task is considered

complete. The completion status is integrated from completion rate

$$\dot{g}_i\left(\mathbf{r}, t\right) = \begin{cases} 1/\Delta t_{g,i} & \text{if } \texttt{Imageable}_i \text{ and } \left(g_i < 1\right) \\ \\ 0 & \text{otherwise} \end{cases} \tag{2.16}$$

such that $g_i \in [0, 1]$. Total progress across all observation tasks is tracked using $g = \sum_{i=1}^{n_g} g_i$, such that $g \in [0, n_g]$, with $g == n_g$ as the criterion for mission completion.

2.2.2.2   Landing

A second science objective is also considered: ballistic deployment of science payloads to the body surface, in which case the control domain represents impulses imparted to the released payload instead of to the main spacecraft. In this scenario, $\texttt{Impact}$ is a required condition rather than a failure criterion.

Beyond merely reaching the body surface, a number of additional considerations are modeled to predict the payload landing accuracy and performance. The distance ρ_k of the impact location $\mathbf{r}_{imp}$ from the k'th desired landing location $\mathbf{R}_k$ can be checked, e.g., to enforce compliance with some maximum bound ρ_{max}.

$$\rho_k = \|\mathbf{r}_{imp} - \mathbf{R}_k\| \tag{2.17}$$

The body-frame impact speed v_{imp} and the angle γ_k between the impact direction and the target's surface-normal direction $\hat{\mathbf{n}}_k$ are also likely to be of interest:

$$v_{imp} = \|\dot{\mathbf{r}}_{imp}\| \tag{2.18}$$

$$\gamma_k = \cos^{-1}\left(\hat{\mathbf{n}}_k \cdot \dot{\mathbf{r}}_{imp}/v_{imp}\right) \tag{2.19}$$

Generically, a goal function might then consist of any sort of combination of these values

$$g_k = g_k\left(\rho_k, v_{imp}, \gamma_k; \rho_{k,max}\right) \tag{2.20}$$

When producing a data product for a human planner more information might be retained by using, for example, $g_k = 1/\left(1 + w_\rho \min|\rho_k|\right)$ and considering v_{imp} and γ_k separately.

2.2.2.3   Periodic Motion

Either as part of a periodic science operation — such as observation of time-varying surface phenomena — or as a safe holding pattern during which to conduct extended communications or deliberation, periodic orbital motion may be another desirable objective. Quantifying how nearly periodic a reachable trajectory is begins by defining a plane with normal vector $\hat{\mathbf{n}}$ computed as the in-track direction of the initial condition.

$$\hat{\mathbf{n}}_0 = (\hat{\mathbf{r}}_0 \times \hat{\mathbf{v}}_0) \times \hat{\mathbf{r}}_0$$

This plane, illustrated in Figure 2.1, contains both the initial position (the 0'th crossing) and the origin while also maximizing the transverse component of the initial velocity. Subsequent crossings of the plane are detected by tracking the quantity

$$c(t) = \mathbf{r}(t) \cdot \hat{\mathbf{n}}_0 \tag{2.21}$$
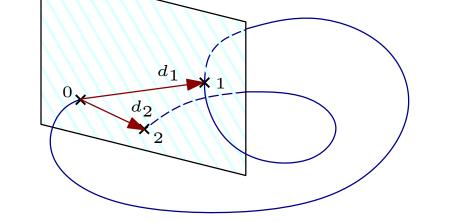
Figure 2.1: Poincare map of a sampled orbit; the minimum distance d between crossings can be used as a measure of how nearly periodic the orbit is.

The event $c(t_2) > 0 > c(t_1)$ indicates that a crossing, $c(t^*) = 0$, occurs in the positive direction at some intermediate time $t^* \in (t_1, t_2)$. By interpolation or bisectional search, a nearly

exact crossing state $\mathbf{x_j^*} = \mathbf{x}\left(\mathbf{t}^*\right)$ and corresponding crossing distance $d_j = \|\mathbf{x_j^*} - \mathbf{x_0}\|$ are obtained for each $j'th$ occurrence of the crossing condition. The orbit $\mathbf{x_i}(t)$'s measure of periodicity is finally computed as

$$g = \frac{1}{1 + \min\{d_j\}}$$

2.2.3   Intermediary Measures

Beyond the direct specifications of mission success, many additional useful quantities can be derived from the phase-space state and trajectory for use in the planning process. Variables $b \in B$ for assessing future reachability prospects could be as simple as orbit radius $r = |\mathbf{r}|$, osculating Keplerian elements, or Jacobi energy J.

Furthermore, error growth can be predicted by tracking divergence rates along a sampled trajectory, while near-misses of favorable outcomes can be quantified to better inform heuristic search of the reachability map.

2.2.3.1   Divergence and Robustness

Trajectory-relative deviations are linearly approximated from the state transition matrix Φ, numerically propagated along with the trajectory itself. Its integrand is the Jacobian matrix representing the sensitivity of the force model $\mathbf{f}$ to changes in $\mathbf{x}$. For either an elliptical or a polyhedral gravity model, this is easily obtained as a side-product of force computations with little additional effort [6].

$$\Phi(t; t_0) = \int_{t_0}^{t} \frac{d\mathbf{f}}{d\mathbf{x}}\bigg|_{\mathbf{x}(\tau)} d\tau = \begin{bmatrix} \phi_{\mathbf{rr}}(t) & \phi_{\mathbf{rv}}(t) \\ \phi_{\mathbf{vr}}(t) & \phi_{\mathbf{vv}}(t) \end{bmatrix} \tag{2.22}$$

Using submatrices of Φ, the linearized position deviation time series $\boldsymbol{\Lambda}\left(t\right)$ is expressed in terms of initial condition deviations:

$$\boldsymbol{\Lambda}(t) = \phi_{\mathbf{rr}}(t; t_0)\delta\mathbf{r}(t_0) + \phi_{\mathbf{rv}}(t; t_0)\delta\mathbf{v}(t_0) \tag{2.23}$$

The worst-case deviation magnitude Λ possible under initial position and velocity deviation magnitudes σ_r and σ_v is then obtained using the maximum eigenvalues of the submatrices:

$$\Lambda(t) = \lambda_{max}\left(\phi_{\mathbf{rr}}(t)\right)\sigma_r + \lambda_{max}\left(\phi_{\mathbf{rv}}(t)\right)\sigma_v \tag{2.24}$$

One use of deviation measurements is simply to distinguish between regions where errors grow rapidly (or cheap maneuvers can cause large orbit changes) and those where they do not.

By leveraging the abstraction-based problem formulation, the information can alternately be translated directly into a worst-case effect on outcomes of interest. This is done by first introducing a parameterizable robustness margin d. A simple, constant definition $d(t) = \zeta$ is used as a baseline for comparison with the more motivated, time-varying definition $d(t) = \eta\Lambda(t)$ that implies robustness to η standard deviations of error. The worst possible influence of a position deviation d upon objective fulfillment is then represented by reducing the acceptable bounds (a^+, a^-) of each objective sub-measure $a \in A$ accordingly, relative to the midpoint value $a^* = (a^+ + a^-)/2$

$$a^{\pm} = a^* \pm \Delta^d a \tag{2.25}$$

where the expression $\Delta^d a$ relates a sub-measure's deviation to a position deviation of magnitude d. For observation sub-measures, this espression takes the following forms:

$$\Delta^d \rho = \Delta\rho - d \tag{2.26}$$

$$\Delta^d \theta = \Delta\theta - d/\left(\rho^* - \Delta^d\rho\right) \tag{2.27}$$

$$\Delta^d \varphi = \Delta\varphi - d/\left[\left(\rho^* - \Delta^d\rho\right)\sin\left(\theta^* - \Delta^d\theta\right)\right] \tag{2.28}$$

$$\Delta^d \psi = \Delta\psi - 2\sin^{-1}\left(d/(2\rho)\right) \tag{2.29}$$

These values are subsituted into Eq. 2.32 to shrink the acceptable sub-measure value range as functionally plotted in Figure 2.2 and visualized in the mission scenario illustrations of Section 2.3 for purely spatial measures. Similarly, the reaction criterion for d-robust planning can be stated as

$$\texttt{Danger}\,(\mathbf{r}, d) = \left(\rho_{\mathcal{B}}(\mathbf{r}) - d < \rho_{\mathcal{B}}^-\right) \tag{2.30}$$

with a cushion parameter $\rho_{\mathcal{B}}^-$ introduced to accommodate uncertainty in the model of the body surface.

Finally, an additional criterion is introduced based upon a simple threshold of predicted deviation:

$$\texttt{Expire} = (d > d_{max}) \tag{2.31}$$

As the effects of deviations on abstract outcomes are already accounted for above, this criterion will be used merely to improve computational efficiency by terminating some propagations early. For example, setting d_{max} to be the smallest dimension of any goal region saves the effort of computing motion beyond the time at which robust goal fulfillment becomes impossible.

2.2.3.2   Gradients of Intermediary Measures

Generally, science objectives and failure criteria are ultimately interpreted in a Boolean sense — impact either did or did not occur and observation requirements either were or were not fulfilled. While this is appropriate for classifying a single trajectory, it ignores underlying information that could be useful during informed sampling of the continuous design space of possible trajectories. Exploiting this continuous structure could be especially vital when control sets that achieve a given objective are very small relative to the size of the control domain.

To achieve this, a real-valued measure $q_a \in [0,1]$ of the quality of the spacecraft state in terms of a generic observation sub-measure a is constructed. This function of the actual deviation $\delta(a) = |a - a^*|$ is parameterized by the midpoint value a^*, the allowable deviation $\Delta^d a$ shrunken by the robustness margin, and a new parameter that greatly broadens the set of control inputs for which nonzero outputs are attained: the extended deviation ∇a.

$$q_a(t) = \begin{cases} 1 & \text{if } \delta a(t) < \Delta a \\ \frac{\delta a(t) - \Delta a}{\nabla a - \Delta a} & \text{if } \Delta a < \delta a(t) < \nabla a \\ 0 & \text{if } \delta a(t) > \nabla a \end{cases} \tag{2.32}$$

The continuous nature of this quality function will play a pivotal role in aiding an efficient search of the reachable set of decision values, i.e., scores. Figure 2.2 shows how the shape of $q_a(a)$ is influenced by mission requirements (a^+, a^-) and design parameters ζ or η and ∇a. In all cases, ∇a
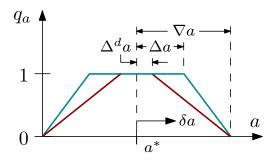
Figure 2.2: Metric quality function defined by mission requirements and planner design parameters.

is set to maximally extend the gradient, i.e., $\nabla \rho = r_{esc}$ and $\nabla a = 180°$ for all angular quantities.

Completion of an objective requires all its component measures to satisfy their prescribed bounds simultaneously. This criterion is scalarized as the overall quality measure

$$q = \frac{1}{\#A} \left(\sum_{a \in A} q_a^{e_q} \right)^{1/e_q} \tag{2.33}$$

such that $q = 1 \iff q_a = 1 \ \forall \ a \in A$ regardless of the choice of e_q, another search design parameter which merely distorts the slope of $q(A)$ in the regime $q < 1$.

The value q is assessed for each of the n_g observation tasks and a scalar measure $Q \in [0, 1]$, the instantaneous maximum amount by which any objective's quality measure exceeds its completion status, is used as an overall indicator of chances for goal completion.

$$Q(t) = \max_{i=1}^{n_g} \{ \max(q_i(t) - g_i(t), 0) \} \tag{2.34}$$

High maxima of $Q(t)$ imply that a trajectory closely approaches the goal region for a task that has not yet been completed. By computing these maxima over segments preceeding or following prospective arc end time t, with t_h as the time horizon to which the trajectory was propagated, two other useful series are produced:

$$\overleftarrow{Q}(t) = \max_{\tau \in (t_0, t)} Q(\tau) \ , \qquad\qquad \overrightarrow{Q}(t) = \max_{\tau \in (t, t_h)} Q(\tau) \tag{2.35}$$

A large value of missed quality $\overleftarrow{Q}(t)$ therefore suggests that a small difference in the imparted $\Delta\mathbf{v}$ could place the spacecraft on a trajectory that fully satisfies objective constraints. Conversely, a large prospective quality $\overrightarrow{Q}(t)$ reflects that the forthcoming planning cycle may afford chances for objective completion via some $q_i == 1$, which implies the criterion $\texttt{Imageable}_i$. However, the extended phase space field $Q(\mathbf{x}, t)$ may have many maxima below unity; i.e., the selection of $\Delta\mathbf{v}$ to attain $q == 1$ is a non-convex problem.

2.3   Test Cases

A series of increasingly challenging test cases have been used throughout the development of the planning algorithm, most of which correspond to actual small bodies that have been targeted by robotic exploration missions: the near-Earth asteroid Itokawa, Mars' small, low-orbiting planetary satellite Phobos, and the short-period comet 67/P Churyumov-Gerasimenko. Itokawa, the target of the only completed asteroid sample-return mission to date, presents a highly triaxial shape and low mass, such that the influence of SRP is significant. Phobos, conversely, is less triaxial and much more massive, with dominant perturbations instead caused by the tidal forces of its low-altitude orbit about Mars. Combined with scientific interest, its extreme dynamical properties have motivated studies of various classes of trajectories for manned or unmanned exploration missions [9, 75]. Comet 67/P is a contact binary with an especially unusual shape exhibiting a large amount of concavity; near perihelion, this body produced significant outgassing, however this force category was not included in the analysis.

The basic physical properties of these bodies are listed in Table 2.1 along with relative measures of non-Keplerian influences and the search domain bounds used to generate illustrative reachability maps. The SRP acceleration and the spin rate are given in terms of the minimum surface gravitational acceleration $g_\alpha = |\mathbf{g}(\alpha\hat{\mathbf{x}})|$ and the critical spin rate $\omega_* = \sqrt{g_\alpha/\alpha}$ that would cause centripetal shedding of mass under the absence of cohesive forces and external influences. Standard reachable domain designation reflects a reference orbit radius of twice the mean central body radius $\bar{R} = (\alpha\beta\gamma)^{1/3}$, a maximum maneuver magnitude corresponding to the Keplerian escape

velocity, and a prediction time horizon of 2.5 times the osculating circular orbit period associated with the reference orbit radius.

Table 2.1: Dynamical model parameter values

		Itokawa	Phobos	67/P	
Principal axes†		$0.54 \times 0.29 \times 0.21$	$27 \times 22 \times 18$	$4.1 \times 3.3 \times 1.8$	km
				$2.6 \times 2.3 \times 1.8$	km
Density		1.9	1.9	0.47	g/cm^3
Spin period		12.1	7.65	12.4	hr
Third body	3B	Sun	Mars	Sun	
Axis ratios†	$\alpha : \beta : \gamma$	$2.6 : 1.4 : 1$	$1.5 : 1.2 : 1$	$2.3 : 1.8 : 1$	γ
				$1.4 : 1.3 : 1$	γ
Spin rate	ω	0.29	0.36	0.28	ω_*
3B gravitation	μ_P	5.6×10^{19}	6.0×10^7	2.0×10^{17}	μ
3B distance	$|\mathbf{d}|$	8.3×10^8	850	1.1×10^8	R
3B mean motion	n	negligible	1	negligible	ω
SRP acceleration	a_S	0.026‡	negligible	negligible	g_α
Domain size	Δv_{max}	0.092	9.0	variable	m/s
Time horizon	t	18	17	Expire	hr

† Values for 67/P reflect two distinct lobes; model uses polyhedral shape.
‡ Approximate value for the Hayabusa spacecraft at perihelion

Mission scenarios are formulated by combining the above physical models with sets of objectives from the categories outlined in Section 2.2.2 — close-range observations, deployment of payloads to target sites, and repetition of motion. These test cases are summarized in Table 2.2 below.

Scenarios Ito-Easy and Pho-Easy are plotted in Figure 2.3. Large conical observation zones are designated for five points of interest, with bounds consisting only of maximum viewing distances comparable to the central body mean radius and minimal viewing co-elevations in the range of $25° < \theta^- < 40°$. Long imaging durations Δt_g are also used for these tasks, with the end effect of producing smooth variation of g over large regions of the search domain to produce reachability maps that clearly illustrate the abstract reachability concept.

The sequence of cases Sphere, Half-Ito, and Ito-Hard are designed to reveal the ultimate impact of non-Keplerian dynamics on the behavior of the complete receding-horizon planner. These

Table 2.2: Test Case Mission Scenarios

Scenario	Dynamics	Objectives	Figure
Generic	α:β:γ ellipsoid w/ 3B	observation, periodicity	not shown
Ito-Easy	Itokawa	easy observation set	2.3
Pho-Easy	Phobos	easy observation set	2.3
Sphere	1:1:1 ellipsoid	observation clusters	2.4
Half-Ito	1.64:1.12:1 ellipsoid	observation clusters	not shown
Ito-Hard	Itokawa	observation clusters	2.4
Pho-Hard	Phobos	hard observation set	2.4
67/P-Obs	67/P	observation clusters	2.5
67/P-Land	67/P	deployment set	2.6

Figure 2.3: Easy observation sets for Ito-Easy and Pho-Easy test cases.

effects are isolated by defining the observation tasks consistently in terms of target latitude, longitude, and surface normal. Figure 2.4 shows the Sphere and Ito-Hard scenarios, with much smaller observation distances of about $\bar{R}/4$. Four tasks are assigned per surface target location: one from within $\theta^+ = 20°$ of the surface normal, and three from between $\theta^- = 30°$ and $\theta^+ = 60°$ with additional azimuthal constraints producing evenly spaced $60°$ segments. Lighting geometry bounds $\psi^\pm$ that translate to an acceptable phasing window that lasts 20% of the rotational period are optionally included as well. Observation sub-measure requirements must be simultaneously satisfied for a span of $\Delta t_g = 2$ minutes. This figure also shows the test case Pho-Hard, with slightly larger

$$(a) \qquad\qquad (b) \qquad\qquad (c)$$
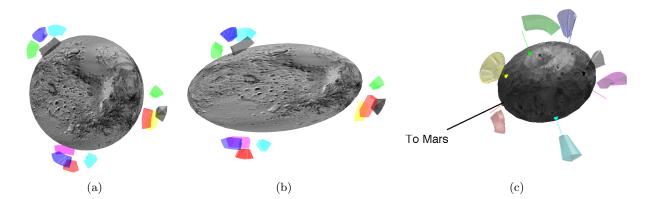
Figure 2.4: Clustered observation sets for (a) Sphere and (b) Ito-Hard test cases; Half-Ito, not pictured, correspons to an intermediary state of elongation. (c) Pho-Hard test case.

observation regions, increased imaging durations of 7 minutes, and 20% to 30% phasing windows.

The case 67/P-Obs is shown in Figure 2.5; observation targets correspond to three of the candidate landing sites considered by for ESA's Philae lander, namely the actual target Site J on the smaller lobe of the comet, the backup Site C on the perimeter of the larger lobe, and an earlier candidate Site A on the inner surface of the larger lobe. Other than a scaling up of $\rho^\pm$, observation task clusters for each site are generated identically to those of the case Ito-Hard, including phasing requirements; this affords close views with moderate shadows to best reveal surface features. The figure shows both the high-resolution $\nu = 2500$ polyhedron used as a truth model and the low-resolution $\nu = 64$ polyhedron used for fast online planning. Shrunken observation zones in the

second subfigure demonstrate the difference of $\Delta^d a$ under a significant robustness margin d.

Finally, Figure 2.6 illustrates the payload deployment test case 67/P-Land. Three landing sites are selected to provide diverse challenges in deployment trajectory design:

- **Site J**, the location targeted for Philae's deployment in the Rosetta mission, lies on the "head" of the comet; local geometry is convex at coarse resolution, and the surface normal direction $\hat{\mathbf{n}}_J$ is roughly parallel with the site's large-magnitude position vector $\mathbf{R}_J$.

- **Site C**, the runner-up candidate site for Philae, lies on the opposite lobe at a similar distance from the center of mass. However, its surface normal $\hat{\mathbf{n}}_C$ is more nearly perpendicular to its position vector $\mathbf{R}_C$.

- **Site N**, which was not a candidate site in the Rosetta mission, is located on the northern half of the comet's "neck". Highly convex local geometry makes it difficult to reach, while its close proximity to the center of mass implies higher impact velocities.

Impact distance from each target is bounded to be no greater than $\rho_{max} = 150$ m for a successful landing, combined with an impact angle restriction of $\gamma_{max} = 30°$.

(a) (b)
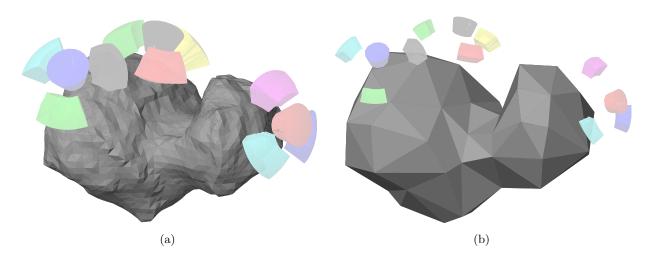
Figure 2.5: Body and goal region geometries for (a) "truth" polyhedron with nominal objective measure ranges Δa and (b) low-resolution prediction polyhedron with reduced objective measure ranges $\Delta^d a$.
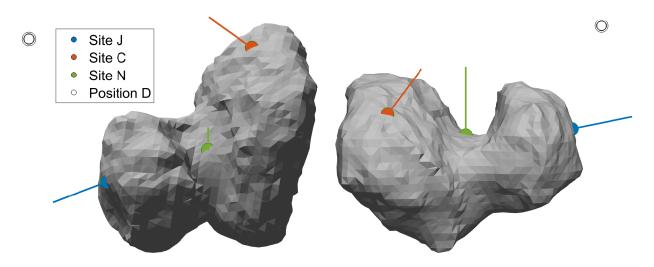
Figure 2.6: Two views of the three surface locations targeted for payload depoyment.

Chapter 3

Abstract Reachability

Abstract reachability analysis poses this central question: what mission-level outcomes can be accomplished under the given control authority? The main ingredients of such an analysis are a description of the control method, a definition of "mission-level outcomes", and a causal relationship that links the two. Under natural motion, this relationship is readily described via the development of the predictive model in Chapter 2.

This chapter will begin by detailing an appropriate control paradigm that easily accommodates a reachability analysis approach based upon natural, ballistic motion. Variations on the implementation of this control method will then be described in order to allow the examination of trade-offs between the dimensionality and parameterization of the reachability search problem relative to its computational burden and the overall performance of the planning algorithm. Beginning with the analytically solvable Kepler problem, example reachability maps will be derived and illustrated for increasingly abstract mission-level outcomes. Finally, numerically computed maps for non-Keplerian systems under finite time horizons will be contrasted against the simple Keplerian examples to illustrate the characteristics and challenges of sampling-based planning in the targeted problem.

3.1   Control Scheme

Reachability stems directly from the form and bounds of a control parameter $\mathbf{u}(t)$ present in the system's dynamics. Due to the nonintegrable nature of the small body mission problem, the

results of a continuous domain of control inputs cannot be determined analytically. Time-varying $\mathbf{u}(t)$, such as the continuous force of a low-thrust engine with unconstrained slewing, would further exacerbate the curse of dimensionality in the search of the mission design space Fortunately, a highly discretized control strategy — intermittent execution of impulsive-thrust maneuvers — is conventional and appropriate for small body exploration missions. This drastically reduces the size of the control space to a degree that it becomes feasible to search numerically. Several characteristics of these systems justify the intermittent impulse approach, foremost the low speeds of even close-proximity orbits due to weak gravitational fields. The Keplerian circular orbit speed at two mean radii about asteroid Eros is about 5 m/s; for comet 67/P the equivalent value is less than 50 cm/s and for asteroid Itokawa it is less than 10 cm/s. This allows drastic changes to the spacecraft's orbital path to be imparted at fuel costs that are miniscule compared to the cost of reaching and rendezvousing with the body, typically several km/s.

Such weak gravitational fields may also bring to mind alternate control strategies; however, these carry with them other downsides. A frequent-impulse scheme, i.e., hovering or otherwise merely overpowering the natural motion of the system, could prove appropriate for focused short term operations but would become fuel-prohibitive relatively quickly. In some scenarios, plume impingement upon the body surface could also become a factor. A low-thrust control scheme, conversely, might simply lack the thrust levels to respond decisively to rapid error growth, in addition to increasing the complexity of the planning problem. Both of these strategies could also complicate the spacecraft's ability to simultaneously operate science subsystems, particularly due to associated pointing constraints. Furthermore, undue noise would be introduced into the process of orbit determination and system parameter estimation. In light of these drawbacks, the intermittent impulse scheme is identified as both the most practical to implement and the most straightforward to study with reachability analysis.

3.2   Outcome Mapping

Given a control scheme, reachability analysis next requires a mapping from control inputs to elements of the outcome space. The impulsive control scheme described above provides a direct correspondence between control inputs and initial conditions. Thus, the first stage of the mapping is the operation of the natural physical dynamics F, i.e., integration under the force model of Eq. 2.1, upon the attained initial conditions $\mathbf{x}_0 = \mathbf{x}(t_0)$ to output a trajectory through phase space, $\tilde{\mathbf{x}}(t; t_0)$, with tilde denoting that the variable includes trajectory history since epoch t_0. For brevity, this epoch will frequently be omitted from notation.

$$F : (t_0, \mathbf{x}_0) \longrightarrow \tilde{\mathbf{x}}(t) \tag{3.1}$$

$$\tilde{\mathbf{x}}(t) = \{\mathbf{x}(\tau)\}_{t_0 \leq \tau \leq t} \tag{3.2}$$

The second mapping stage then utilizes the mission specifications G, composed of equations from Section 2.2, to evaluate the physical trajectory in terms of abstract quantities of interest, which are collected in the outcome vector $\mathbf{y}$.

$$G : \tilde{\mathbf{x}}(t) \longrightarrow \mathbf{y}(t) \tag{3.3}$$

These abstract outcomes may include any measurement or quantity of interest that isn't merely a state/configuration of the system, including time-integrated quantities that depend not only on a trajectory's current state but also its history.

Outcome states $\mathbf{y}$ then reveal the mission-level trade space for decision-making. Such an information product can be used by a mission designer during preliminary analysis and is analogous to certain approaches and analyses that have received attention in the past. Most well-known, "pork chop" plots relate two design variables — departure and arrival dates — to the minimal fuel cost of an orbit transfer to a targeted state, e.g., via Lambert's method. A variant of this approach has also been studied for designing low-energy transfers from the Earth to the Moon, with alternative design parameterizations of the departure state and a broader set of output measures including travel time and injection altitude [37]. Other authors have selected Cartesian subspaces to obtain

broad pictures of stability [47] and impact [51] in the CR3BP, both quantities being of interest for the autonomous planning algorithm.

Finally, for autonomous planning, the outcomes $\mathbf{y}$ need to be appropriately interpreted by scalar objective functions for each type of decision to be made. This is done with the planner H, producing a score vector $\mathbf{s}$ whose contents are essentially second-order outcomes of the control input.

$$H : \mathbf{y}\left(t\right) \longrightarrow \mathbf{s}\left(t\right) \tag{3.4}$$

Individual score values s_i will be described during discussion of the planner's design in Chapter 6 — the scalar score notation s and scalar usage of the term "score" will refer to the decision function and its value for a given input. Lastly, the score vector time series $\mathbf{s}(t)$ is reduced to an individual score state $\mathbf{s}'$ via a timing process T that acts to maximize the decision variable across time.

$$\left(s'; t'\right) = \max_t s\left(t\right) \tag{3.5}$$

$$\mathbf{s}' = \mathbf{s}\left(t'\right) \tag{3.6}$$

Altogether, the predictive model that relates initial states (translatable directly from control inputs) to decisions is structured as

$$(t_0, \mathbf{x}_0) \xrightarrow{F} \tilde{\mathbf{x}}(t) \xrightarrow{G} \mathbf{y}(t) \xrightarrow{H} \mathbf{s}(t) \xrightarrow{T} \left(t', \mathbf{s}'\right) \tag{3.7}$$

This model can thus be composed as a single mapping M, or a time-reduced map M' that reflects each input's best possible outcome.

$$M = H \circ G \circ F \tag{3.8}$$

$$M' = T \circ M \tag{3.9}$$

$$M' : (t_0, \mathbf{x}_0) \longrightarrow \left(t', \mathbf{s}'\right) \tag{3.10}$$

3.3   Reachable Domains

Given time-dependence in some quantities of interest, such as solar phasing, the entirety of possible system configurations is described by the extended phase space $(\mathcal{T}, \mathcal{X})$. Thus, the complete

realm of possible outcomes is obtained from $G \circ F : (\mathcal{T}, \mathcal{X}) \longrightarrow \mathcal{Y}(t)$, where $\mathbf{y} \in \mathcal{Y}$. For the 3DOF nonautonomous systems of interest, this initial condition space has $\dim(\mathcal{T} \times \mathcal{X}) = 7$.

In order to reduce the problem description to a computationally feasible level and aid accessibility to human interpretation, a lower-dimensional subset of possible initial conditions is used. As is appropriate for online planning, these reduced planning domains $\mathcal{D} \subset (\mathcal{T}, \mathcal{X})$ reflect the initial conditions that are reachable from a nominal state using the available control set $\mathcal{U}$. Then, the mapping processes M' can conceptually be applied to relate the admissible controls to full sets of reachable trajectories $\tilde{\mathcal{X}}$, sets of attainable mission results $\mathcal{Y}$ and scores $\mathcal{S}$ and finally the best attainable scores $\mathcal{S}'$.

$$(\mathcal{U}; t_0, \mathbf{x}_0) \xrightarrow{F} \tilde{\mathcal{X}}(t) \xrightarrow{G} \mathcal{Y}(t) \xrightarrow{H} \mathcal{S}(t) \xrightarrow{T} (\mathcal{T}', \mathcal{S}') \tag{3.11}$$

$$M' : (\mathcal{U}; t_0, \mathbf{x}_0) \longrightarrow (\mathcal{T}', \mathcal{S}') \tag{3.12}$$

Here, $\mathcal{T}'$ represents the set of final epochs that maximize the decision score s. The steps of the continuous-set mapping process are illustrated in Figure 3.1 assuming a control domain $\mathcal{U}_{sph}$ to be described next.
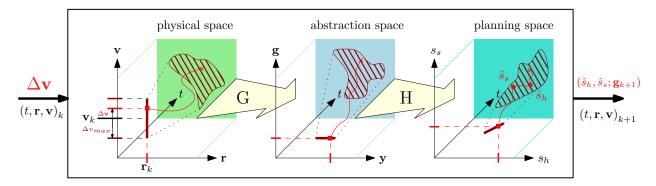
Figure 3.1: Illustration of the mapping process from an initial domain, defined by the state $(t_0, \mathbf{x}_0)$ and the control set $\mathcal{U}_{sph}$, through the space of abstract outcomes and ultimately to scores that govern automated decisions.

3.3.1 Planning Domains

As previously discussed, control authority consists of the selection of some impulsive thrust maneuver $\Delta\mathbf{v}$ to execute at some time Δt defined relative to the initial epoch. Beginning from a broad definition of admissible control sets,

$$\Delta t \in \Delta\mathcal{T} = (0, \Delta t_{max}) \tag{3.13}$$

$$\Delta\mathbf{v} \in \Delta\mathcal{V} = \left\{\Delta\mathbf{v} \in \mathbb{R}^3 \;\middle|\; \Delta\mathbf{v} \cdot \Delta\mathbf{v} \leq \Delta v_{max}^2 \right\} \tag{3.14}$$

a first cut is made to define the control domain and full reachable domain from a given nominal trajectory $\mathbf{x}(t)$ as

$$\mathcal{U}_{full} = \Delta\mathcal{T} \times \Delta\mathcal{V} \tag{3.15}$$

$$\mathcal{D}_{full}\left(\mathcal{U}_{full}; \mathbf{x}\left(t\right)\right) = \left(t_0 + \Delta\mathcal{T}, \mathbf{r}\left(t_0 + \Delta\mathcal{T}\right), \mathbf{v}\left(t_0 + \Delta\mathcal{T}\right) + \Delta\mathcal{V}\right) \tag{3.16}$$

However, because $\mathcal{U}_{full}$ is still large with $\dim\left(\mathcal{U}_{full}\right) = 4$, additional pruning of the design space is necessary in order to further reduce its dimensionality. Two options are considered for defining an online planning domain $\mathcal{U}_{sub} \subset \mathcal{U}_{full}$ with $\dim\left(\mathcal{U}_{sub}\right) = 3$, a level of dimensionality that will be demonstrated as numerically manageable in later results.

First, by selecting $\Delta t = 0$, the spherical velocity-space control domain $\mathcal{U}_{sph}$ and reachable domain $\mathcal{D}_{sph} = (\mathbf{r}_0, \mathbf{v}_0 + \Delta\mathcal{V})$ are defined. $\mathcal{U}_{sph}$ will be the most extensively used domain in later online planning analyses, with timing decisions handled instead by the process T. However, an alternate search domain $\mathcal{U}_{cyl} = (\Delta\mathcal{T}, \Delta\mathcal{V}_\perp\left(\hat{\mathbf{n}}\right))$ will also be tested to explore the utility of the temporal degree of freedom, instead sacrificing one degree of freedom within the velocity domain defined by the vector $\hat{\mathbf{n}}$.

$$\Delta\mathcal{V}_\perp\left(\hat{\mathbf{n}}\right) = \left\{\Delta\mathbf{v} \in \Delta\mathcal{V} \;\middle|\; \Delta\mathbf{v} \cdot \hat{n} = 0\right\} \tag{3.17}$$

A useful convention is to parameterize $\hat{\mathbf{n}}$ in the radial, in-track, cross-track (RIC) frame such that

$$\hat{\mathbf{n}} \in \left\{\hat{\mathbf{R}}, \hat{\mathbf{I}}, \hat{\mathbf{C}}\right\}, \qquad \mathbf{R} = \mathbf{r}, \qquad \mathbf{C} = \mathbf{r} \times \mathbf{v}, \qquad \hat{\mathbf{I}} = \hat{\mathbf{C}} \times \hat{\mathbf{R}} \tag{3.18}$$

which introduces dependence of $\hat{\mathbf{n}}$ upon $\mathbf{x}(t)$.

3.3.2   Visualization Domains

Further dimensional reduction can be useful for visualization, whether by using a domain $\mathcal{U}_{disk} = \Delta\mathcal{V}_\perp(\hat{\mathbf{n}})$ or $\mathcal{U}_{shell} = \Delta\mathcal{V}_\circ(v)$, with

$$\Delta\mathcal{V}_\circ(v) = \left\{ \Delta\mathbf{v} \in \Delta\mathcal{V} \ \big| \ \Delta\mathbf{v} \cdot \Delta\mathbf{v} = v^2 \right\} \tag{3.19}$$

defining a spherical shell in velocity space — a level set of fuel cost. For this object, the Mollweide equal-area map projection can be used.

Finally, 3D domains such as $\mathcal{U}_{sph}$ and $\mathcal{U}_{cyl}$ can be visualized with standard perspective-based projection. In general, this merely results in a view of the outer surface of the domain, but interior details can be accessed by only plotting subdomains $\mathcal{U}_{chunk}$ based upon Boolean filtering rules that operate on the outcome set.

$$\mathcal{U}_{chunk}\left(\mathcal{Y}'; \texttt{Filter}\right) = \left\{ \mathbf{u} \in \mathcal{U} \ \big| \ \texttt{Filter}\left(\mathbf{y}'(\mathbf{u})\right) \right\} \tag{3.20}$$

For example, setting $\texttt{Filter} = \texttt{Impact}$ would return only those regions of the control domain whose constituent inputs $\mathbf{u}$ result in satisfation of the $\texttt{Impact}$ criterion.

3.4   Keplerian Analysis

As a stepping stone to understanding the structure of reachability maps for non-Keplerian systems, results under Keplerian mechanics are investigated first. For many useful properties and outcomes, the structure of these maps is fixed and represents an infinite time horizon. The plots of this section are all obtained analytically — closed-form expressions for level curves of various properties in the initial velocity space are all derived in Appendix B. Analyses reflect planar maneuvering prospects at a finite spherical central body with radius R and an initial spacecraft orbit radius r; velocity is normalized such that when oriented perpendicular to the initial radius, unity speed produces a circular orbit.

3.4.1   Keplerian Element Level Sets

Because Keplerian elements remain constant in pure two-body motion, single-impulse reachable orbits can be fully described by analytically mapping from initial velocities to these elements. Figure 3.2 shows the straightforward relationship between initial velocity and semimajor axis from Eq. B.1 — because initial position cannot be instantaneously changed by controls, the orbit energy and therefore the semimajor axis varies directly with the initial speed, producing concentric level sets about the origin. Less trivial is the eccentricity, whose level curves (Eq. B.4) emanate from a
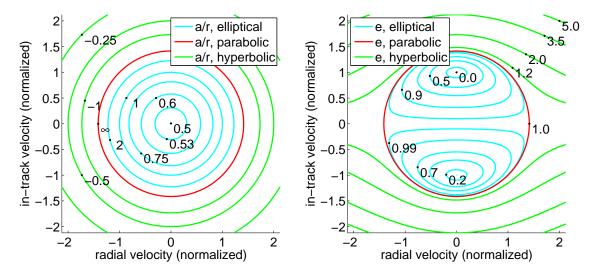
Figure 3.2: Level curves of normalized semimajor axis and eccentricity within the normalized initial velocity space.

pair of circular ($e = 0$) orbit points — prograde at $(0, 1)$ and retrograde at $(0, -1)$ — to a single circle of radius $\sqrt{2}$, the family of parabolic orbits, centered about the origin. Eccentricity in the hyperbolic regime grows rapidly as additional in-track velocity is added, and slowly with changes in radial velocity.

As seen in Figure 3.3, level curves of argument of periapsis (Eq. B.5) emanate radially from the circular orbit points, at which the quantity is undefined. The combination of this information with the previous two plots reveals the relative costs and the degrees of independence for changing different Keplerian elements from a given initial state.
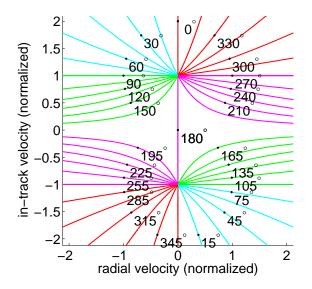
Figure 3.3: Level curves of argument of periapsis within the normalized initial velocity space. Singular points at (0,1) and (0,-1) are prograde and retrograde circular orbits.

3.4.2   Safety Constraints

The safety terms outlined in Section 2.2.1 are easily related to Keplerian elements. Impact occurs if and only if an orbit's radius of periapsis is lower than the spherical central body radius R, and escape occurs when eccentricity reaches unity or greater. Figure 3.4 shades in the regions for each of these criteria; when overlap occurs, the failure criterion to occur first takes preference. Bounds of impact sets are computed from Eq. B.6 and are parameterized by the ratio R/r, the normalized proximity of the initial state to the central body. The second plot shows level curves for speed and flight path angle at radius of impact R; these are obtained from Eqs. B.8 and B.7. The two quantities are seen to vary mostly independently from each other except when the radial component of the initial velocity is small.

3.4.3   Goal Rendezvous

Finally, the problem of transfering to target points above the central body is illustrated. Two parameters set the location of the target in the inertial plane: β describes its radius while θ gives the spacecraft-body-target angle. Families of successful transfers are plotted in Figure 3.5 for fixed
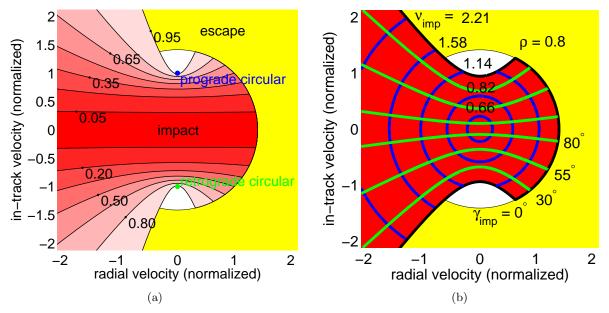
Figure 3.4: Analytically-derived outcome maps under Keplerian dynamics. (a) Level curves of grazing impact as a function of orbit radius normalized by body radius; shading interior to curves indicates incident impact. (b) Level curves of impact velocity (blue lines) and impact angle (green lines).

β, varied θ and vice versa. It can be seen that goal-fulfillment options are much broader if the spacecraft is permitted to use trajectories that would later result in failure if no further actions were taken. However, these results are difficult to extend to applications where the target is not inertially fixed, as is the case for body-relative observations.

3.5   Non-Keplerian Qualities

This section will present numerous examples of reachability maps for non-Keplerian systems with the purpose of emphasizing fundamental qualitative differences caused by perturbations away from Keplerian motion. In keeping with the focus upon the general dynamical phenomena of these systems and the broad occurrence and meaning of structural complexity in their maps, precise specifications of the problem setups are omitted. Safety outcomes will be the primary results of interest as they are the most general and are sufficient for demonstrating most non-Keplerian phenomena of concern; more objective-oriented analyses and discussions are contained in Chapter
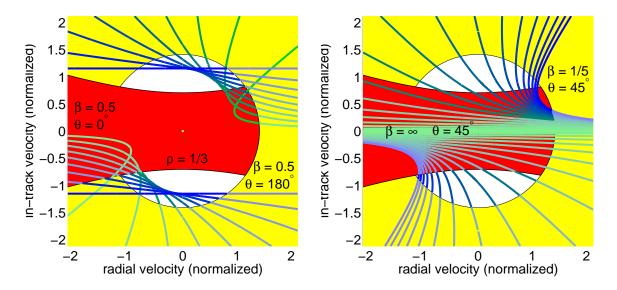
Figure 3.5: Analytical reachability of goal locations as a function of their angular displacement and radius. Left: radius fixed, angle varied. Right: angle fixed, radius varied. Faded lines signify occurrence of failure condition before attainment of goal.

5 following the discussion of map computation in Chapter 4.

3.5.1   Adding Perturbations

Because all trajectories in Keplerian systems are conic sections, equivalence between states and conics was used in determining features of the Keplerian reachability map in the previous section, whose features are valid for an infinite time horizon. However, trajectories in strongly perturbed systems are generally nonperiodic, and their propagation for numerical reachability sampling can only be conducted over a finite time interval. Figure 3.6 compares a mathematically derived map with a numerically generated one for the same finite-sphere Keplerian system. General structure appears identical, but the impact region of the numerical map is truncated in the positive radial velocity direction due to its finite time horizon combined with the growth toward infinity of the periods of outbound orbits as eccentricity approaches unity.

As nonsphericality is the dominant source of perturbations in low orbits for a large share of small-body systems, an initial look at non-Keplerian map structure is produced in Figure 3.7 by

(a) Analytical, infinite horizon   (b) Numerical, finite horizon
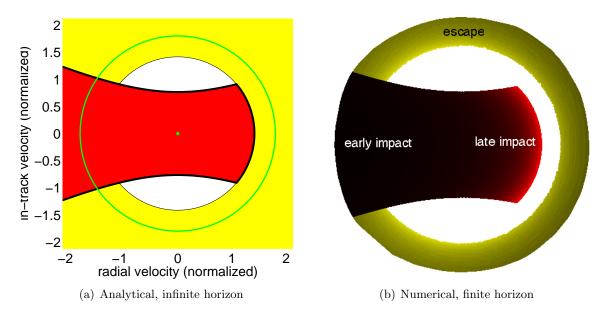
Figure 3.6: Outcome maps for failure scenarios in the Kepler problem.

incrementing the triaxiality of a central body that is initially spherical and has uniform rotation. A 3D view of $\mathcal{U}_{chunk}$ (Impact) is used to emphasize changes on the surface of the impact set.
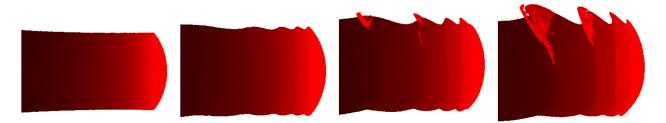
Figure 3.7: Evolution of the impact set as the triaxiality of a spinning spherical central body is incrementally increased.

After the first increment, the border of the set becomes wavy, but otherwise appears to retain its simple gradient structure of time-to-impact. However, the second triaxiality increment produces new impact families that are distinctly more brightly colored than neighboring families, which indicates a considerably longer time-to-impact. The pattern becomes pronounced after a third increment, with late-impacting families consistently growing from the lobes on one side of the set. This is suggestive of resonance effects, where an early close pass (indicated by proximity on

the map to early-impacting sets) causes a perturbation that results in impact at a later state. It is concluded that the "waves" on the early-impacting sets are a first-order effect primarily caused by the body rotating into or out of an orbit path, while late-impacting families are increasingly attributable to gravitational perturbations throughout their lifetimes rather than body orientation alone.

Next, synchronous third-body perturbations are incrementally added to this model to produce the results of Figure 3.8. This reflects the environment of small planetary satellites; synchronicity is appropriate because strong third-body gravitation generally results in tidal locking. Unlike the
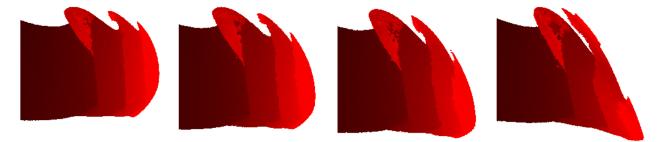
Figure 3.8: Evolution of the impact set as the third body gravitation is incrementally increased at a spinning triaxial central body.

influence of triaxiality, this perturbation appears to fundamentally alter the shape of even early-impacting orbit families. Not shown, changes to the initial condition $(t_0, \mathbf{x}_0)$ also modify the effects of both perturbations upon map structure.

Other important non-Keplerian qualities are better illustrated on 2D domains $\mathcal{U}_{disk}$. In Figure 3.9, the central body's rotation rate is incremented simultaneously with its triaxiality and the magnitude of third-body gravitation. Some of the resultant map features are very thin and finely detailed, emphasizing the high sensitivity of important outcomes to small changes in initial conditions. Additionally, the second perturbation increment produces a somewhat more complex picture than the third — this implies that the combination of perturbations can interact in diverse and unintuitive ways.

Figure 3.9: Impact and escape sets for out-of-plane maneuvers by an orbiter of a rotating ellipsoid as rotation rate, triaxiality, and third body perturbations are incremented simultaneously.

3.5.2   Extended Horizons

As mentioned before, a key difference between Keplerian and non-Keplerian reachability maps is the effect of the time horizon; for generic initial conditions, infinite-time bounds on impact and escape sets can be computed *a priori* only under Keplerian dynamics, where the periapse radius and the eccentricity are both integrals of motion. At a non-spherical body, most trajectories are nonperiodic and do not facilitate extrapolation of properties over infinite time, and there is no longer a one-to-one correspondence between periapse radius and impact. One effective illustration of this fundamental difference is actually the examination of an exception to the general rule. By zooming in on the lower "arm" feature of the final map of Figure 3.9 while simultaneously increasing the time horizon, the sequence of results shown in Figure 3.10 are generated. These maps illustrate self-similarity oriented about the center point of the zoom, which retains "safe" status even over

Figure 3.10: Successive magnified views of the lower spiral arm feature from the final map of Figure 3.9 as the time horizon is extended.

time horizons and zoom levels large enough to begin to introduce the numerical noise visible in the final panel. At the same time, the surrounding red spiral continues to grow infinitely with time, filling in more of the map and coming infinitessimaly close to the safe center point. By propagating this point's corresponding initial condition, shown in Figure 3.11, the meaning of these features becomes imminently clear; the repeating spiral is centered around a periodic orbit, and the dissimilar surounding context at the highest zoom level is because the condition does not begin on the orbit but rather travels onto it along its stable manifold. Further, the interspersed white arms of the spiral could indicate neighboring safe quasiperiodic orbits, with the unsafe gaps corresponding to resonance conditions similar to those that cause Kirkwood's gaps in the distribution of orbit periods of main belt asteroids.

(a)   (b)
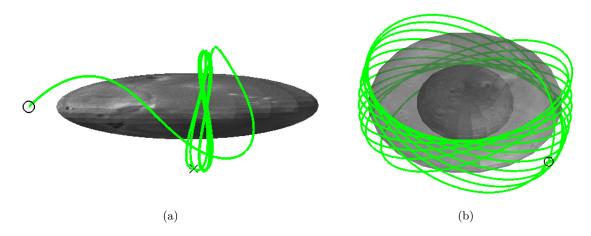
Figure 3.11: Trajectory sampled from the center of Figure 3.10's infinite spiral, shown in (a) body-fixed frame and (b) inertial frame. The orbit arrives at a Lyapunov periodic orbit from along its stable manifold.

More generally, most non-Keplerian reachability prospects do not correspond to periodic orbits or stable manifolds. Figure 3.12 shows a broader picture of reachability under extended-time analysis. The short-horizon result of subfigure (a) resembles the findings of Figure 3.7; the Keplerian impact set is distorted with wavy lobes and attached late-impacting families. However, increasing the time horizon by a factor of five fills in much of the safe zone with later occurrences of impact and escape. The largest remaining families of safe orbits are either near the early-escaping
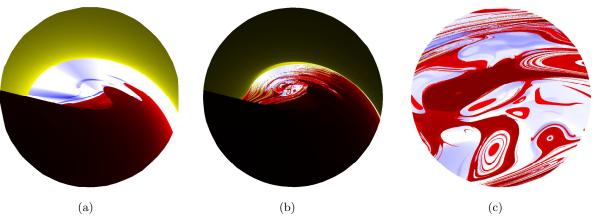
Figure 3.12: Radial/in-track objective reachability map with (a) short time horizon and (b) long time horizon for motion in the Ito-Easy test case. (c) magnifies a complex region of the long-horizon result.

set, implying eccentricities just below unity and long orbit periods, or near the center point of the map, which reflects an osculatingly circular orbit state. A zoomed view of this region reveals concentric rings of impacting sets, suggesting very complex resonance phenomena.

3.5.3   Reachability From Sensitive Structures

The above reachability analyses were conducted from typical initial orbit states; however, far more complex results can be obtained by beginning from special phase space structures. Figure 3.13 shows a $\mathcal{U}_{shell}$ reachability map for a state on the periodic orbit from 3.11, i.e., with all initial states deviated by equal-magnitude velocity perturbations. Complex effects of resonances are again apparent in the concentric sequences of impact families, whose interstitial safe regions might correspond to quasiperiodic orbits with long-term stability.

Figure 3.14 shows a sequence of $\mathcal{U}_{disk}$ maps generated for a spacecraft at the L1 point of the Mars-Phobos system. Reachability options appear more complex and diverse than any preceding analysis with a comparable time horizon. This is in keeping with the nature of hyperbolic equilibrium points in conservative systems — along with their stable and unstable manifolds, these points separate different regimes of phase space such that very small perturbations can drive the state in vastly different directions.
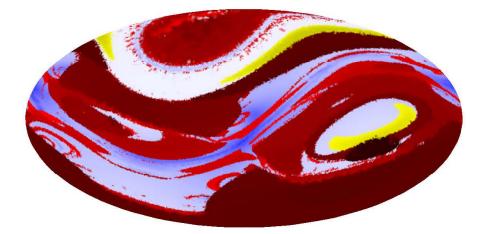
Figure 3.13: Reachability prospects in the immediate neighborhood of a periodic orbit.
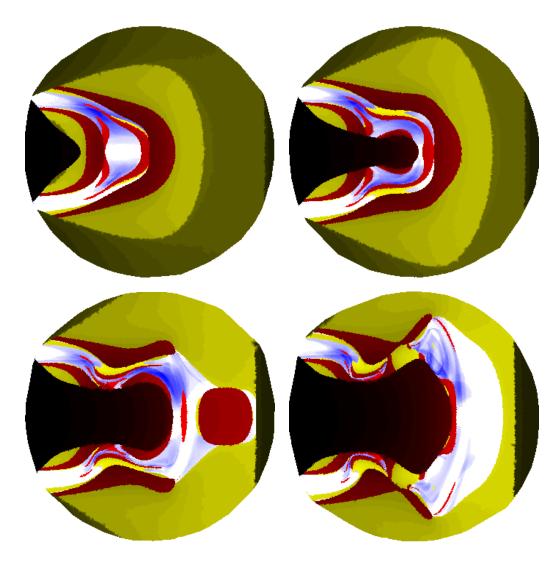
Figure 3.14: Reachability prospects from the L1 point of the Mars-Phobos system. Each disk has a different velocity magnitude in the normal direction, representing increasingly retrograde motion.

Chapter 4

Map Computation and Search

Although reachability analyses are naturally applicable to continuous control domains, results cannot be computed in continuous form for nonintegrable system models such as the small body mission problem. This chapter will address the challenges of leveraging the reachability map concept for preliminary analysis and online planning in the context of limited, discrete numerical computations. After discussing the inference of information across continuous volumes based upon knowledge of discrete points, an adaptive refinement method is introduced that boosts computational efficiency by focusing numerical sampling at useful locations. Then, the formulation of heuristics that govern the bias of the sample distribution is explored in depth, including features inspired by hill-climbing algorithms and simulated annealing. These tools are shown to produce data products for either usage paradigm that vastly outperform a naive grid-search approach for equivalent computational effort.

4.1   Discrete Approximation

Due to nonintegrability, the continuous-domain map $M'(\mathcal{U})$ cannot be computed in its entirety. Instead, numerical propagations of only a finite number N of discrete control points $\{\mathbf{u}_i\} \in \mathcal{U}$ provide $M'(\mathbf{u}_i) = \mathbf{s}'_i$ for $i = 1, 2, \ldots, N$. Knowledge of the outcomes for this discrete sample can then be used to infer continuous structure across the map.

Two types of strategy for making this inference are tesselation and triangulation. In tesselation, individual points define finite regions that collectively fill the the full domain without

overlapping. Triangulation conversely uses $n+1$ sampled points to define vertices of n-dimensional shapes called simplices, e.g., triangles for $n = 2$ and tetrahedra for $n = 3$, which likewise fill the domain without any redundant coverage. This is selected as the preferred approach as it associates a given test point with multiple sampled points, inherently providing a framework for interpolating values that vary continuously.

4.1.1   Mesh Elements

The list of simplices, which when combined with the list of sampled points is termed the "mesh" $\mathcal{M} = (\{\mathbf{u}_i\}, \{V_j\})$, is computed via Delaunay triangulation in order to minimize the occurrence of sharp angles. Each simplex V_j consists of $n + 1$ vertex IDs, i.e., $V_j = (i_{j,1}, i_{j,2}, i_{j,3}, i_{j,4})$ for $n = 3$. The flow of a set of initial states resulting from one of these control-domain volume elements under the physical dynamics F can be conceptualized as the propagation of a tube through phase space. If certain properties are common between points that bound the element, they can thus be inferred to also apply to points on the interior as the resulting trajectory must remain inside the tube. Real-valued outcomes can also be interpolated based upon this logic.

However, such conclusions imply that outcomes are shared or similar because the propagated paths closely neighbor each other. The validity of this assumption generally correlates inversely to the size of the element; as the distance between two points increases, so does the likelihood or magnitude of outcome dissimilarity. Average element size correlates with total sample count, limiting the average accuracy of such inferences in proportion with the computational budget for sample propagation. Depending on the desired application of the computed map, it may be beneficial to increase resolution and therefore accuracy in specific regions at a cost of reduced resolution/accuracy in the remainder of the map.

4.1.2   Resolving Features

For preliminary mission design and general system analysis, visualizations are needed that illustrate the correspondence of $\mathbf{u}$ with various outcome values $\mathbf{y}(\tilde{\mathbf{x}})$ such as Boolean safety status

or real-valued goal progression. As demonstrated in Chapter 3, these outcomes may be uniform over large regions, e.g., where stability assures long-term safety for a broad family of trajectories, or may vary quite finely due to resonance effects or exacting requirements for objective fulfillment. Accurate perception of the big picture requires these features to be sufficiently resolved.

For Boolean outcomes, this means that the total volume of simplices meeting the `Border` criterion should be minimal in proportion to the total volume of the domain, where

$$\texttt{Border}\,(V;y) = \left(\exists\,(i_1, i_2) \in V \ \middle| \ y(\mathbf{u}_{i,1}) \neq y(\mathbf{u}_{i,2})\right) \tag{4.1}$$

In other words, indeterminate regions of the mesh should be made as small as possible. In the case of real-valued outcomes, variance across a simplex should be consistent between all simplices in order to map the value's gradient with uniform accuracy.

$$\texttt{Mean}\,(V;y) = \frac{1}{n}\sum_{i \in V} y(\mathbf{u}_i) \tag{4.2}$$

$$\texttt{Variance}\,(V;y) = \sum_{i \in V} \left(y(\mathbf{u}_i) - \texttt{Mean}\,(V;y)\right)^2 \tag{4.3}$$

4.1.3 Objective Maximization

Conversely, an autonomously operating spacecraft need not concern itself with globally partitioning the map and resolving all features. Nor does each output y warrant individual attention; trade-space decisions must be automated by constructing a single scalar decision function $s\,(\mathbf{y})$. What is then primarily important is to locate the maximum of this decision function across the map as accurately as possible, i.e., minimizing the difference between the best sampled value s^* and the true global maximum $\max s'\,(\mathcal{D})$.

$$(s^*; \mathbf{u}^*, t^*) = \max_{\mathbf{u} \in \mathcal{M}} s'\,(\mathbf{u}) \tag{4.4}$$

This optimal point could potentially lie in a relatively uniform map region, and many complexly structured regions in terms of some outputs y may be uniformly low scoring in terms of s; therefore, a sample distribution that works well for one usage paradigm may be poorly suited to the other.

4.2   Adaptive Mesh Refinement

The inhomogeneity of required sampling resolution for different uses motivates an informed approach to the sampling process. Adaptive sampling has been used before in dynamically similar settings [52, 76, 50] as well as more disparate applications such as finite element methods for flow fields and structural analysis. The following section will detail the heuristic used to govern sample refinement; here we will discuss the general process.

4.2.1   Initialization

Given no *a priori* knowledge of map features or the score field $s(\mathcal{U})$, the first set of sampled control inputs $\mathbf{u_i} \in \mathcal{U}$ is distributed either randomly or evenly. This sample of N_0 points is then numerically propagated until each result has reached a terminal condition – either failure or time-out/expiry. The sample set ultimately maps through associated trajectories $\widetilde{\mathbf{x}_i}(t) \in \widetilde{\mathcal{X}}(t)$ to mission results $\mathbf{y_i}(t) \in \mathcal{Y}(t)$ and score trajectories $s(t) \in \mathcal{S}(t)$ which are lastly temporally reduced by the map T and associated lifespans (s', t'). Delaunay triangulation is then used to build this sample set $\{\mathbf{u_i}\}$ into an initial mesh $\mathcal{M}_0$ consisting of a small number of large volume elements V_j.

4.2.2   Sample Incrementation

The initial N_0-sample mesh is sufficient for inferring map structure to a coarse level of accuracy. In each refinement iteration, additional samples are taken heterogeneously to preferentially increase accuracy in certain areas, with the benefit of all previously attained information. The final distribution of N_f total sample points therefore depends not only upon the sampling heuristic, but also on the number of sampling cycles and their individual sizes. A higher iteration count f permits the adaptive scheme to compound its benefits more frequently, but also requires more computational overhead through the number of meshing operations. This demand may or may not be significant relative to the total effort required for trajectory propagations, which scales only with N_f and with the duration and sensitivity of individual trajectories.

Compounding effects of the iteratively adapted sample distribution could serve to increasingly localize further samples to smaller regions, which may in turn imply a need for fewer samples in later cycles. A uniform sample increment $N_k - N_{k-1} = \Delta N \ \forall \ k$ may then not be the most effective option. The sampling scheme is instead defined by four parameters: initial sample size N_0, final sample size N_f, iteration count f, and an additional setting e_N such that

$$(N_f - N_1)/f = \left(N_k^{1/e_N} - N_{k-1}^{1/e_N} \right)^{e_N} \tag{4.5}$$

Increments then become successively larger if $e_N > 1$ or successively smaller with $e_N < 1$.

4.2.3   Simplex-wise Subdivision

Inferences of map content in unsampled regions can be made using sets of $m > 1$ sampled points. For example, in a 3D map $(n = 3)$ interpolation/triangulation could be done on an edge $(m = 2)$, a triangular face $(m = 3)$, or a tetrahedral simplex $(m = 4)$. Full-dimension simplices are used by the heuristic to allow interpolation of outcomes at any point in $\mathcal{U}$ without needing an overly cumbersome scheme using $m > n + 1$, such as splines. Furthermore, the total volume of $\mathcal{M}$ remains roughly constant during the refinement process, unlike the ever-increasing total face area or edge length — a fact that will be leveraged during heuristic formulation.

The search heuristic operates on the mesh to assign each j'th simplex a weight W_j based upon the extent to which the numerically propagated results of its vertices indicate that it contains relevant missing detail. Each simplex's largest interior sphere is computed and its center and radius are used to define a 3D normal distribution from which an additional maneuver is sampled each time the simplex's ID is drawn from a W-weighted random sample. This allows rapid gains in resolution at high-value regions even under a single refinement iteration; the heuristic cannot "saturate" as would occur in a random sampling scheme without replacement.

4.2.4   Iterative Refinement Algorithm

Adaptive mesh refinement can now be summarized as the following iterative procedure:

(1) Construct series of cumulative sample sizes.

(2) Initialize mesh with uniform or random sample of control inputs.

(3) Execute refinement sequence for each sample increment.

  (a) Propagate each new control input through the prediction model to determine its outcomes and score.

  (b) Using the full set of sampled points as vertices, triangulate a new mesh.

  — Terminate loop if final sample size is achieved.

  (c) Apply the search heuristic to weight each element based upon its properties.

  (d) Conduct a weighted random sample of element IDs from within which to sample additional control inputs.

Symbolically, this process is given in Algorithm 1 in further detail, assuming provided functions DelaunayTri for Delaunay triangulation, Grid for conducting uniform initial sampling, and SubDivide for selecting points within a simplex.

4.3   Heuristic Formulation

New sample points in the domain are selected first by selecting simplices from within the mesh, and then sampling points within those simplices. In a uniformly gridded mesh, the weighted random sampling could be conducted based upon simplex outcome properties alone, without any undesired influences present. However, the adaptive refinement process necessarily produces simplices with variation in their size and shape. When subdividing a simplex by sampling a point within it, points in larger simplices thus have less likelihood of being sampled, making the two-stage point-sampling process different from sampling a continuous domain. This effect can be normalized by by beginning the heuristic with a volume weighting term:

$$W = \text{vol}(V)\,(\ldots) \tag{4.6}$$

Algorithm 1: Iterative refinement of mesh approximating a reachability map.

1 function ReachMap $(t_0, \mathbf{x}_0, \mathcal{U}, M', W(V))$;

   Input : Initial state $(t_0, \mathbf{x}_0)$, control domain $\mathcal{U}$, model M', search heuristic $W(V)$

   Output: Mesh $\mathcal{M}_f = \left(\{\mathbf{u}_i\}_{1:N_f}, \{V_j\}_{1:(2N_f-4)} \right)$ with results $\{t'_i, \mathbf{x}'_i, \mathbf{y}'_i, \mathbf{s}'_i\}_{1:N_f}$

                                      `// recall that` $n_{\text{faces}} = 2n_{\text{vertices}} - 4$

2 $(N_1, N_2, \ldots, N_f) \xleftarrow{\text{Eq.4.5}} (f, e_N)$;   `// series of cumulative sample sizes`

3 $\mathcal{M}_0 \leftarrow \text{DelaunayTri}(\text{Grid}(N_0, \mathcal{U}))$;   `// uniform initial mesh`

4 $N_{-1} \leftarrow 0$;

5 **for** $k = 0, 1, 2, \ldots, f$ **do**

6 $\{t'_i, \mathbf{x}'_i, \mathbf{y}'_i, \mathbf{s}'_i\}_{(N_{k-1}, N_k]} \leftarrow M'\left(\{\mathbf{u}_i\}_{(N_{k-1}, N_k]}; t_0, \mathbf{x}_0 \right)$;   `// propagate each new input`

7 $\mathcal{M}_k \leftarrow \text{DelaunayTri}\{\mathbf{u}_i\}_{1:N_k}$;   `// update mesh`

8   **if** $k == f$ **then**

9 | break;

10   **end**

11 $\{W_j\}_{1:(2N_k-4)} \leftarrow W\{V_j\}_{1:(2N_k-4)}$;   `// assign weights via heuristic`

12 $\text{IDs} \leftarrow \text{WeightedSample}\{V_j, W_j\}_{1:(2N_k-4)}$;   `// weighted random sample`

13 $\{\mathbf{u}_i\}_{(N_k, N_{k+1}]} \leftarrow \text{SubDivide}\{V_j\}_{\text{IDs}}$;   `// subdivide sampled simplices`

14 **end**

If the simplex subdivision process contains no biases of its own (all interior points equally likely to be sampled), then the above weighting function would generate a flat probability distribution across the continuous domain — all points would have equal likelihood.

The next step is to design additional factors that introduce useful biases. Before considering outputs of interest, we note that the temporal horizon, i.e., $t'(\mathcal{U})$ can also vary considerably across the domain and even within small regions. Longer trajectory durations provide more opportunity for nearby paths to diverge and for interesting information to exist in the middle. Looking more closely at such regions thus aids the heuristic in locating finely-detailed structure in general, which might have otherwise been overlooked.

$$W = \text{vol}(V) \left(\underset{i \in V}{\text{mean}} \{t'_i - t_0\} \right) (\ldots) \tag{4.7}$$

Finally, a factor is needed to apply sampling bias to regions that produce outcomes of interest. As the exact form of this term will be discussed in turn for each the two map usage paradigms, the full heuristic given below states it generically as a function S of the outcomes of the vertices of the

simplex.

$$W = \text{vol}(V) \left(\underset{i \in V}{\text{mean}} \left\{ t_i' - t_0 \right\} \right) S\left(y(V)\right)^{(\ldots)} \tag{4.8}$$

4.3.1 Simulated Annealing

With a search heuristic in place, successive incarnations of the mesh may be anticipated to transition from coarse and evenly sampled at $\mathcal{M}_0$, with no correlation between sample distribution and outcome information, to a more complex and structured $\mathcal{M}_f$. This final mesh should consist of a few large elements with short-lived trajectories and uninteresting contents (large $\text{vol}(V)$, small S) and many more small elements resolving relevant details achieved on long-lived paths (small $\text{vol}(V)$, large S).

During this transition, the heuristic sampling scheme can be expected to function more effectively each iteration since it has more information at its disposal. Two mechanisms can be used to efficiently leverage this principal to gradually transition from a global search across all of $\mathcal{U}$ to localized searches in regions with nearly globally maximal scores. First, setting $e_N < 1$ metes out smaller and smaller sampling increments ΔN_k, thus being more proportional to the ever-decreasing volume of remaining areas where additional search effort might be expected to reveal a new global known maximum.

To complement the reduction of sample increment with a reduction of search scope, the simplex score S is exponentiated with a function e_S that increases as the search proceeds.

$$W = \text{vol}(V) \left(\underset{i \in V}{\text{mean}} \left\{ t_i' - t_0 \right\} \right) S\left(y(V)\right)^{e_S\left(N_k/N_f\right)} \tag{4.9}$$

This progressively amplifies the bias toward those remaining high-scoring areas in a manner closely related to simulated annealing. Figure 4.1 shows the changing relationship between simplex score S and sampling probability W under the influence of the exponent e_S as refinement progress increases, using a formulation

$$e_S\left(N_k\right) = 2^{\left(8 N_k/N_f\right)} \tag{4.10}$$
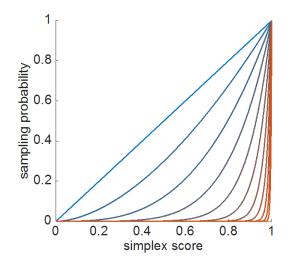
Figure 4.1: Inceasing bias toward high-scoring regions as refinement progression factor N_k/N_f increases from 0 to 1, shown as transition from blue to red probability distributions.

4.3.2 Partitioning and Smoothing for Visualization
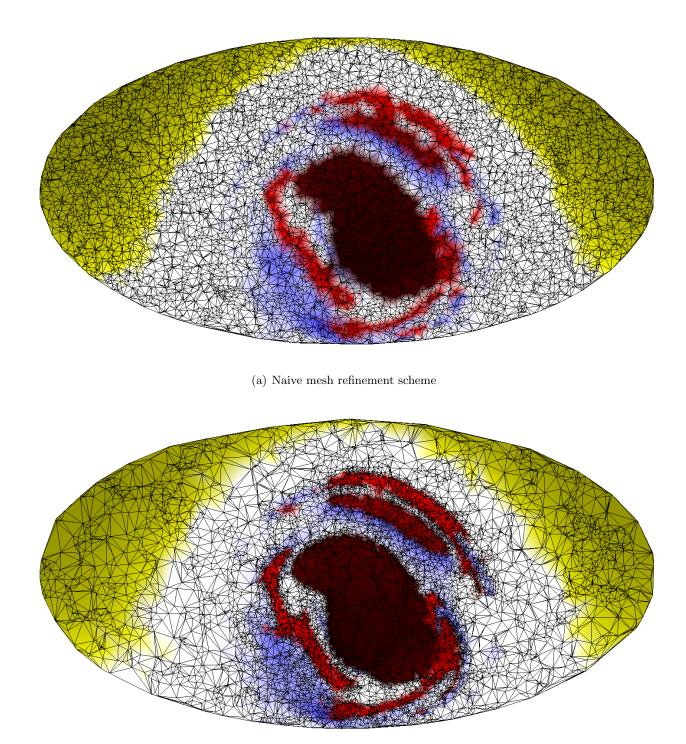
For preliminary mission design and analysis, visualizations are needed that illustrate the correspondence of $\mathbf{u}$ with various outcome values $\mathbf{y}(\tilde{\mathbf{x}})$ such as safety status, goal progression, or other informative measurements. In this case, the function $S(V)$ can be designed to increase in proportion to the variation of specified elements of $\mathbf{y}$ across a given simplex V_j, as measured in Eq. 4.3 or Eq. 4.1 for Booleans,

$$S_{vis}(V) = \texttt{Border}(V; \texttt{Impact}) + \kappa \texttt{Variance}(V; g) \tag{4.11}$$

where the weight κ can be designed to adjust the relative importance of each simplex property and normalize by the global maximum variance, i.e., with a divisor $\max_{V \in \mathcal{M}} \texttt{Variance}(V; g)$.

Figure 4.2 shows the increased clarity of features on the $\mathcal{U} \rightarrow \mathcal{Y}$ reachability map that can be attained at a fixed sample count by applying the heuristic weighting function W with the simplex scoring scheme S_{vis}. Similar improvement is seen in a different category of visualization in Figure 4.3.

(a) Naive mesh refinement scheme

(b) Heuristic mesh refinement scheme

Figure 4.2: Alternative partitioning methods applied at equal resolution to map outcomes on a $\mathcal{U}_{shell}$ domain, projected onto the plane.

(a) Naive mesh refinement scheme   (b) Heuristic mesh refinement scheme
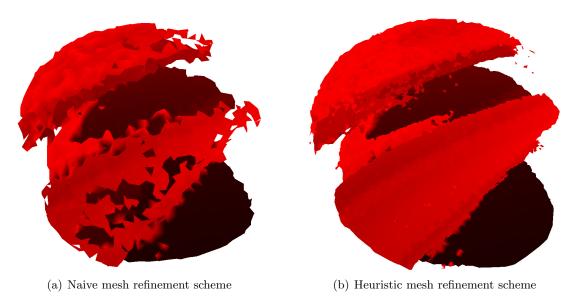
Figure 4.3: Alternative partitioning methods applied at equal resolution to compute a $\mathcal{U}_{chunk}\,(\texttt{Impact})$ domain.

4.3.3   Gradient Ascent for Online Planning

In many cases, goal fulfillment regions in the reachability map may be small enough that the initial mesh $\mathcal{M}_0$ provides no indication of their existence. This is particularly true when N_0 is very small, as may necessarily be the case during autonomous operations. It is then insufficient to construct S to merely recognize goal fulfillment — the search must be biased toward such regions even if they are not represented in the sample set. To accomplish this, additional information is needed about a trajectory's proximity to a goal region in terms of its governing sub-measure set A. Specifically, the value $\overleftarrow{Q}$ from Eq. 2.35 indicates the best quality achieved for any remaining goal over the sample trajectory's lifespan.

A level curve of $\overleftarrow{Q}\,(\mathcal{U})$ is shown in Figure 4.4 for a representative domain along with some small interior regions where $\overleftarrow{Q} = 1$ allows for goal progression, illustrating the need for gradient augmentation in the search heuristic. Note that the choice of design parameter e_q in Eq. 2.33, essentially the p-norm applied to the set of observation sub-measure qualities, distorts the field $\overleftarrow{Q}\,(\mathcal{U})$.

Gradient ascent can thus be introduced to the search for maxima of s', the decision function

designed in Chapter 6 with dependency upon g and by extension upon $\{q_a\}$, in the simplex score function

$$S_{smax} = \max_{i \in V} \left\{ s_i' + \overleftarrow{Q}_i \right\} \tag{4.12}$$

Figure 4.5 shows Monte Carlo mean results of heuristic search on a representative planning domain under the Pho-Hard system model. Clearly, much larger values of s' can rapidly be located by heuristic search than is possible with a naive search. It furthermore is clear that the gradient ascent component is responsible for a large share of these gains. An additional plot illustrates that regions of high performance compose a vanishingly small fraction of the domain's total volume. This indicates that final gains in performance are very hard-won, and shows how the gradient component smoothes out the search for these gains.
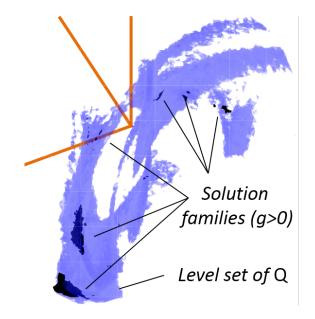
Figure 4.4: Level curves of reachable quality $Q(\mathcal{U}) = 0.75$ (light blue) and $Q(\mathcal{U}) = 1$ (dark blue) illustrating the structure exploited for augmenting the heuristic search with gradient ascent.
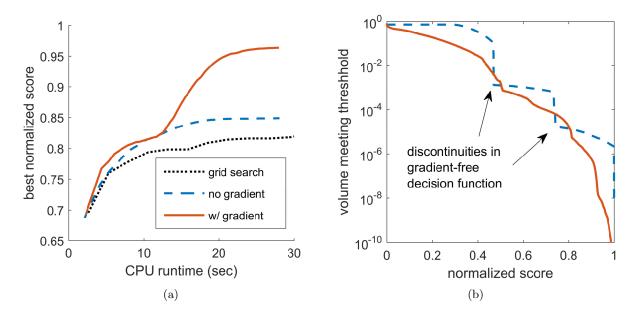
Figure 4.5: (a) Runtime performance of numerical search for maxima of $s'(\mathcal{U})$, i.e., the best-performing option in a control domain. (b) A quantitative assessment of the difficulty of the search problem.

Chapter 5

Reachability Results

Using the tools of Chapter 4, reachability-based mission analysis can be efficiently conducted in terms of the various outcomes and other measures detailed in Chapter 2. This chapter provides several such analyses using a variety of planning domains, physical environments, and objective types — a representative set of scenarios for demonstrating the utility of the maps for preliminary design, human-in-the-loop planning, or for development and calibration of autonomous reachability-based planning algorithms. These results complement those of Chapter 3, which were focused upon the fundamental properties and structure of reachable sets rather than upon specific applications of the concept.

5.1   Close-range Observations

5.1.1   Phobos - 3DOF Maneuvers

Test case Pho-Hard, the close-proximity imaging of target areas on the surface of Phobos, is analyzed under a $\mathcal{U}_{sph}$-type control domain: the initial state and maneuver time are fixed, pointing is unconstrained, and maneuver magnitude is upper-bounded. Figure 5.1 shows four different subsets of the domain. $\mathcal{U}_{chunk}$ views of the impact and escape sets reveal that a large portion of the planning domain produces failure scenarios by the end of the prediction horizon, leaving relatively few options that remain safe for multiple revolutions — an unsurprising result given previous analyses in the literature concerning stability within this system. A level set of the science return measure encloses a comparatively small volume that exhibits complex structure; a view of

all three outcome types on a $\mathcal{U}_{disk}$ subset reveals that these regions are situated in between early-impacting families and are streaked through with late-impacting ones. The contents of the $\mathcal{U}_{shell}$

(a) Impact

(b) Escape

(c) Goal

(d) All
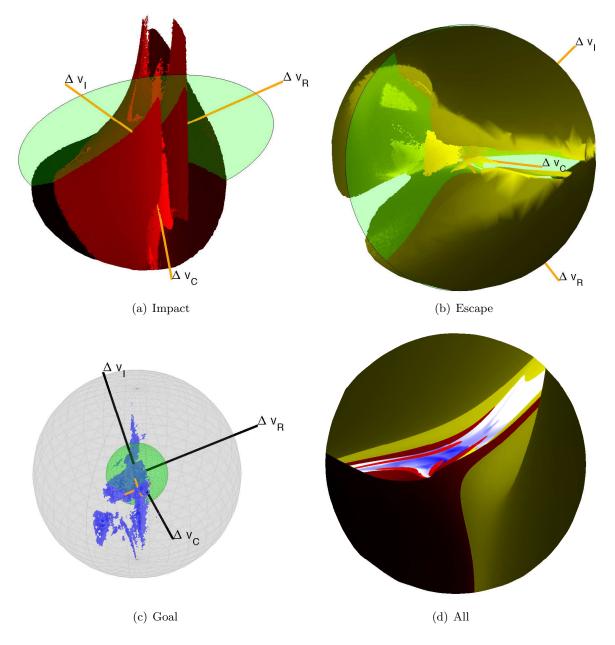
Figure 5.1: Sub-regions $\mathcal{U}_{chunk}$ of the reachable outcome map where maneuvers result in (a) impact of the body surface, (b) crossing of the escape boundary, (c) fulfillment of a decision score threshold s^*. (d) Shows the contents of radial/in-track control domain $\mathcal{U}_{disk} = \Delta\mathcal{V}_\perp(\hat{\mathbf{C}})$, marked by a green disk in subfigures (a) and (b).

domain marked by the green shell in Figure 5.1(c) are shown in a Mollweide projection in Figure

5.2 for an alternative perspective.
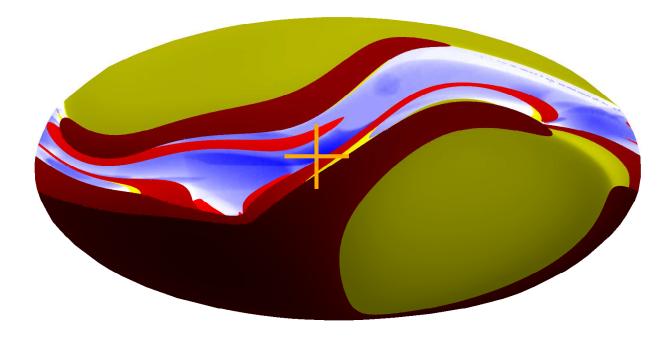
Figure 5.2: Outcome map for a control domain $\mathcal{U}_{shell} = \Delta\mathcal{V}_\circ\,(2.5\text{ m/s})$ for Pho-Easy test case, projected onto the plane. Domain correspons to green spherical shell of Figure 5.1(c).

5.1.2   Comet 67/P - Timed 2DOF Maneuvers

For a perspective on the temporal planning dimension, the 67/P test case is analyzed using $\mathcal{U}_{cyl}$-type domains: maneuver time is selectable, and thrusts can only be aimed within the in-track/cross-track plane. Three domains are mapped corresponding to polar, retrograde, and prograde pre-maneuver trajectories given in Figure 5.3; results are plotted in Figures 5.4, 5.5, and 5.6.

In all cases, resonant effects are clearly observed by alternatingly colored swaths of **u** values that correspond to impact of the two different lobes of 67/P. Furthermore, as the 2D sections reveal and as intuition implies, impact scenarios are only observed when the in-track velocity is decreased, while a sufficient increase uniformly results in escape. Goal fulfillment is not observed

(a) Rotating frame   (b) Inertial frame
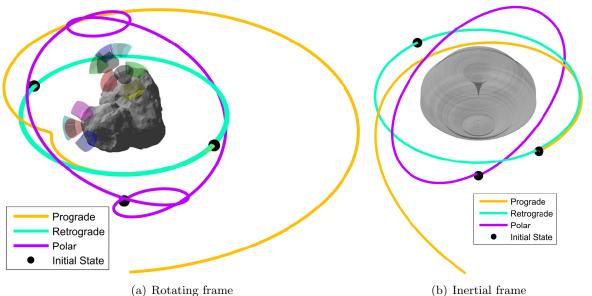
Figure 5.3: Nominal trajectories $\mathbf{x}(t)$ at Comet 67/P used to relate a time-parameterized control domain to the reachable domain $\mathcal{D}_{cyl}\left(\mathcal{U}_{cyl}; \mathbf{x}(t)\right)$ as in Eq. 3.16.

for operations in the equatorial plane as most goal regions are defined in the northern hemisphere.

In the polar orbit reachability set of Figure 5.4, the abundance of goal regions near the extrema of the timing axis indicates that goal reachability is maximal when maneuvers are executed above the south pole of the central body. This reflects the large degree of control over phasing that can be achieved by rotating the orbit plane about the polar axis, combined with the fact that all goals are defined north of the body's equator. Similarly, the corkscrew shape of the impacting sets further reflects the misalignment of the spacecraft orbit plane with the central body's rotation plane.

Conversely, the impact set for the retrograde orbit (Figure 5.5) shows fast periodicity along the time axis, indicating that several orbits are completed in the body-fixed frame even though only one is complete in the inertial frame — this also demonstrates the stability that results from the rapid averaging-out of perturbing effects. The modulation of the goal set along this axis with period one reflects the influence of the solar phasing requirement in the science specifications.

Lastly, the prograde orbit reachability map in 5.6 shows less regularity of structure due to

(a) time/in-track/cross-track domain

(b) time/in-track domain
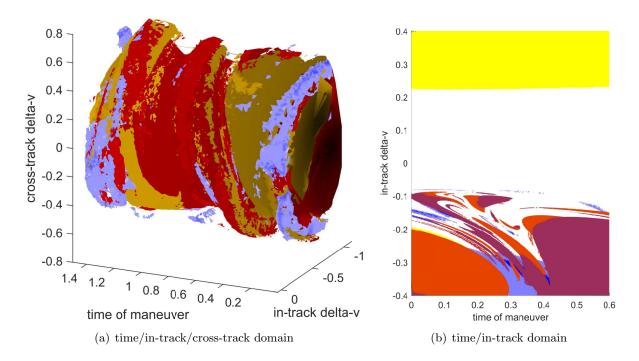
Figure 5.4: Reachability maps from the polar orbit of Figure 5.3 using control domains with timing components.

(a) time/in-track/cross-track domain

(b) time/in-track domain
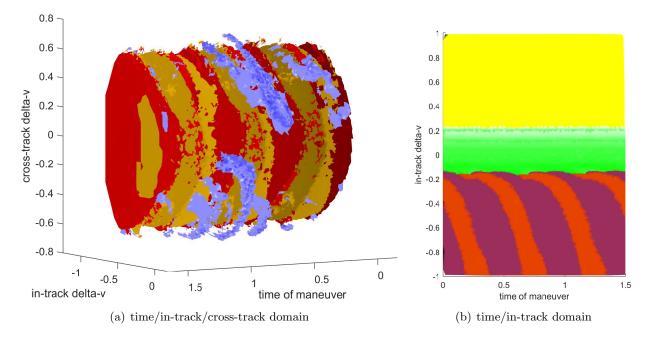
Figure 5.5: Reachability maps from the retrograde orbit of Figure 5.3 using control domains with timing components. Green/white spectrum indicates relative stability.

the strong non-periodicity of the nominal orbit, which occurs due to low-order resonance with the body's rotation. This map is also the most poorly resolved of the set due to the abundance of thin families of failure-producing control inputs that appear as the radius of the nominal orbit grows, illustrating variability in the difficulty of the search problem.

(a) time/in-track/cross-track domain   (b) time/in-track domain
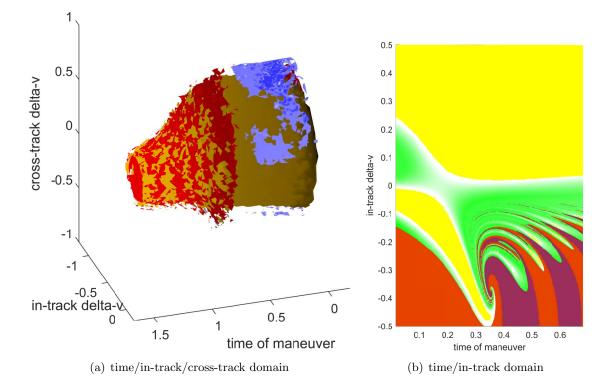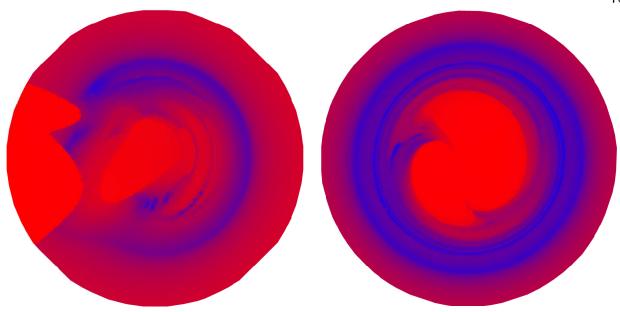
Figure 5.6: Reachability maps from the prograde orbit of Figure 5.3 using control domains with timing components. Green/white spectrum indicates relative stability.

5.2 Divergence and Expiration

The linear error growth measure $\Lambda(t)$ from Eq. 2.24 serves as a measure of divergence that is roughly equivalent to the Fast Lyapunov Indicator. In Figure 5.7, the time-to-failure is plotted on two reachable sets in the 67/P scenario with `Expire` of Eq. 2.31 included as a failure criterion; the maximum positional divergence d_{max} is selected as the smallest radius of any observation region. The prediction horizon was extended such that every trajectory eventually reached a failure criterion; the search is thus complete in the temporal dimension with regards to goal progression.

(a) Radial/cross-track domain, 135° inclined

(b) v_x/v_y domain, above north pole

Figure 5.7: Time to failure plotted on two $\mathcal{U}_{disk}$ domains at comet 67/P using $\Delta\mathcal{V}_\perp(\hat{\mathbf{I}})$ and $\Delta\mathcal{V}_\perp(\hat{\mathbf{z}})$. Inclusion of `Expire` condition illustrates divergence rates for trajectories that do not impact or escape; color scales time of expiry from short (red) to long (blue).

For the first domain, which illustrates options for departing from an inclined retrograde orbit as it crosses the equatorial plane, divergence rates vary drastically. Several islands of relatively long-term stability dot a landscape that otherwise appears largely destabilized by resonant effects. In the second domain, where maneuvers are executed from a point above the north pole, concentric rings of alternating stability and instability indicate the effects of resonance with the body's rotation rate. Toward the interior of the domain, early failure by impact occurs with dependence on phasing relative to the orientation of the central body.

5.3   Landing

Deployment of payloads to surface locations can be studied by analyzing additional properties of the terminal state when `Impact` occurs. In Figure 5.8, the entire set of deployment impulses that produce impact within 30 hours is plotted for test case 67/P-Land. Color brightness indicates time-to-impact, the longest of which occurs when the payload is deployed away from the body

but at an insufficient velocity for escape. The dark end of the trajectory family implies a strong deployment impulse directed toward the body, quickly resulting in high-speed impact; it may be inferred that a $\mathcal{U}_{shell}$ domain were produced for a very fast deployment speed, its cross section through this family would appear as a silhouette of the body shape as seen from the deployment position.
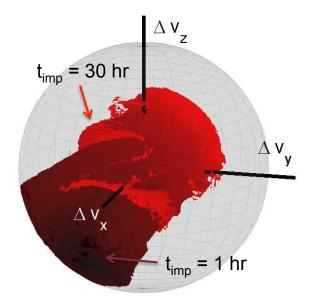
Figure 5.8: Subset of control domain that results in impact of the surface within the maximal prediction horizon for deployment test case 67/P-Land. Brighter coloration indicates longer trajectory lifespan.

Deployment impulses that produce successful landings compose a subset of the impact set; these control-domain regions, plotted in Figure 5.9, can be denoted by

$$\mathcal{U}_{chunk}\left(\texttt{Impact}_k\right) = \left\{\ \Delta\mathbf{v}_i\ \middle|\ \rho_k\left(t; \Delta\mathbf{v}, \mathbf{x}_0\right) \leq \rho_{max} \text{ with } t < t_h\ \right\} \tag{5.1}$$

with $k \in [J, C, N]$ being the index of the landing target. Each site's family exhibits a complex shape that spirals in correspondence to the interplay of the central body's rotation and the variability of the deployment trajectory's Jacobi energy. Performance measures can be seen to vary along the length of these families, whose structure is increasingly fine and complex near the low-energy origin of the control domain.

(a) impact speed

(b) impact angle
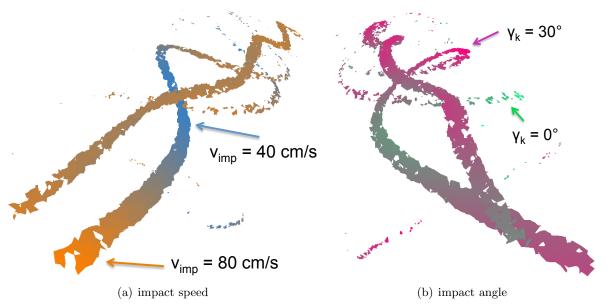
Figure 5.9: Subsets of control domain corresponding to trajectory families that result in successful deployment to one of the landing sites in scenario 67/P-Land. Coloring indicates variation of performance measures.

5.4 Periodicity

Because periodic orbits are 1D manifolds of the 6D phase space, a 3D control domain is generally insufficient for transferring directly onto one. However, nearly-periodic orbits could provide similar utility in the short-term and further GNC efforts could be spent to track a fully periodic orbit if necessary. In Figure 5.10, the periodicity measure from Eq. 2.22 is plotted on a projected $\mathcal{U}_{shell}$ domain for a Generic test case with a 4:2:1 ellipsoid; due to the limited time horizon, only orbits that repeat within two or three revolutions are detected. Bands of nearly-periodic orbit families encircle the main impact region, exhibiting occasional bifurcations. Intersections of these families with impact regions demonstrate that periodic motion could possibly be leveraged for repeating very close-proximity passes, and conversely that the physical central body may drastically reduce the existence of viable periodic orbits within the circumscribing sphere.

The $\mathcal{U}_{chunk}$ domain plotted in Figure 5.11 further demonstrates the occurrence of near-periodicity in continuous families rather than in isolated occurrences, a consequence of Hamil-
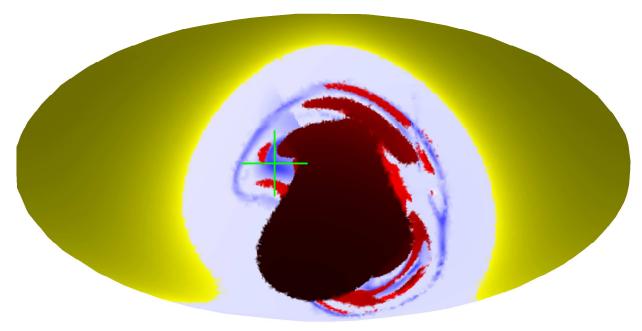
Figure 5.10: Mollweide projection of an orbit periodicity reachability map on a $\mathcal{U}_{shell}$ domain; crosshair marks a control input for inserting into a nearly periodic orbit.

tonian dynamics. Also plotted is a periodic orbit obtained by differentally correcting the initial state produced by the control input marked with a green crosshair. Figure 5.12 gives two additional periodic orbits obtained by combining reachability analysis and differential correction. The adaptive mesh refinement scheme thus holds promise both for autonomous pattern-holding operations and for greatly boosting the computational efficiency of an extensive offline brute-force search for exploitable phase space structures.

(a)

(b)
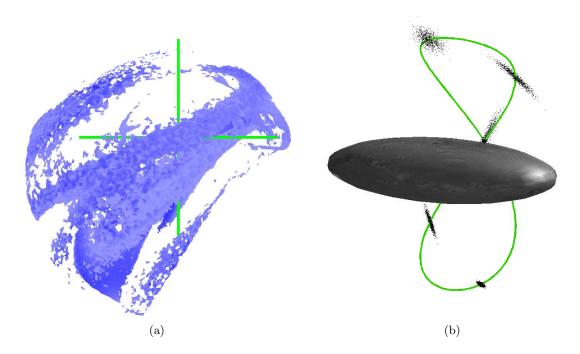
Figure 5.11: (a) Nearly-periodic families in 3D reachable domain $\mathcal{U}_{chunk}$ $(g > g^*)$. (b) Differentially corrected periodic orbit obtained from reachable via the control input marked in Figure 5.10. Point cloud propagation illustrates instability.
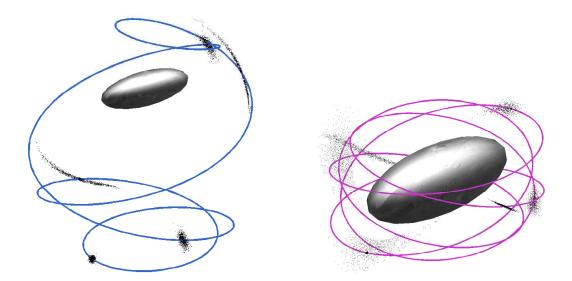
Figure 5.12: Two differentially-corrected periodic orbits obtained from initial guesses located via reachability analysis. Point cloud propagation illustrates instability.

Chapter 6

Receding Horizon Planning

The analyses of Chapter 5 illustrated various types of short-term outcomes reachable with a single control input. At the fingertips of a mission designer, these results facilitate the consideration of trade-offs between many different costs, benefits, and risks. For example, sub-optimal progress toward objectives might be accepted in order to save fuel, to reduce the growth rate of errors by favoring more stable regimes, or to maintain larger margins of safety relative to failure scenarios.

However, such decisions take on additional consequences in the context of extensive mission operations targeting large sets of objectives over many control horizons. It may at times be the case that a cheap and high-achieving maneuver leaves the spacecraft in a situation that causes long-term operations to become more burdensome, or conversely that another control option might achieve little in the short-term but facilitate more rapid progress in later cycles. Furthermore, when key science operations are relegated to relatively narrow time windows, the selection of the subsequent maneuver epoch becomes a way of independently affecting future prospects without altering the current maneuver and thus compromising progress during the current planning horizon. This choice could be particularly influential through its capacity to facilitate phasing and orbit regime changes in the next cycle through the selection of a particular radius or latitude.

Within the reachability map's motivating context as part of a receding-horizon controller, these preferences and trade-offs must be codified in a rule set (or abstract control law) that can be imposed autonomously onboard the spacecraft for online planning. Only then can its benefits be leveraged to perform a complete mission design — including many maneuvers to meet many goals

— without human input and, moreover, with an ability to promptly execute design-level responses to unforeseeable circumstances as they arise.

This chapter begins with a description of the receding-horizon problem and the hierarchy of decisions that must be made autonomously to produce a solution. Complications caused by dividing the problem into a series of control horizons are next discussed along with potential remedies. The automated reachability analysis process is then re-visited in the context of the decision hierarchy and the spacecraft's operational constraints. Finally, the development of the RHC scheme is completed by addressing the process by which planning epochs are selected, including discussion of the "reactivity" paradigm of uncertainty mitigation.

6.1   Receding-Horizon Problem

For a multi-objective campaign, mission completion is defined as attainment of $g(t_f) == n_g$, where g is the sum of all n_g objective completion fractions $0 \leq g_i \leq 1$ and the mission begins at epoch t_0 with $g(t_0) = 0$. At each k'th planning epoch, the algorithm selects a control input $(\Delta t_k, \Delta \mathbf{v}_k) \in \mathcal{U}_k$ on the basis of the score s_{k+1} that it is predicted to produce at the associated subsequent planning epoch t_{k+1}.

A complete mission thus appears as a sequence of control inputs $\mathbf{u}_k = (\Delta t_k, \Delta \mathbf{v}_k)$, each of which produces a ballistic arc $\tilde{\mathbf{x}}(t_k + \Delta t_k, t_{k+1} + \Delta t_{k+1})$. Here, Δt_k is the difference between the beginning of a previously scheduled maneuvering epoch and the actual maneuver time selected during the k'th reachability analysis; t_k are the planning epochs and $t_k + \Delta t_k$ are the maneuver epochs. When $\mathcal{U}_k$ lacks a temporal component, e.g., by using $\mathcal{U}_{sph}$, then $\Delta t_k = 0$ and the two categories of epoch are equivalent. The solution sequence provides $g_K = n_g$ while incurring cumulative fuel expenditures and elapsed time over the K total planning horizons utilized. This reflects the top-level objective of the planner:

Primary Hierarchy Level

Purpose: Fulfill all operational goals without encountering failure criteria

Value: Mission score

$$s_m(t) = \begin{cases} 0 & \text{if } \texttt{Failure}(t) \\ (1/n_g) \sum_{i=1}^{n_g} g_i(t) & \text{otherwise} \end{cases} \qquad (6.1)$$

Preference: Minimize total costs $\sum_{k=0}^{K-1} \Delta v_k$ and $t_K - t_0$.

Solution: Control input set $\{\mathbf{u}_k\}_{0:K-1}$ giving $s_m(t_K) = 1$

By describing objectives as scalar functions, such as the mission score s_m, choices can be made unambiguous and conducted automatically. However, since selecting a maneuver to directly produce $s_m = 1$ is usually not possible, additional lower-level objective functions — other scores governing intermediary actions — are necessary in service of that ultimate end. A hierarchical description of the automated decisions is thus beneficial for organizing the various priorities, concerns, and other details that become relevant at different stages of operation.

Three sub-tasks are utilized for achieving mission completion: the selection of individual maneuvers, the distribution of reachability sample points, and the designation of future planning epochs. In the dynamical description of the planner, the functions governing these decisions compose the planner:

$$H : \mathbf{y}(t) \rightarrow \mathbf{s}(t) \qquad (6.2)$$

$$= [s_m(\mathbf{y}), s_h(\mathbf{y}), s_s(\mathbf{y}), t^*(\tilde{\mathbf{y}})] \qquad (6.3)$$

The design problem then consists primarily of formulating the latter three of these functions effectively.

6.2 Far-Sighted Planning

As will be elaborated upon in the following section, the maximum single-horizon reachable objective increment $\Delta g_k = g_k - g_{k-1}$ for non-trivial mission scenarios and generic initial states is much smaller than n_g and quite possibly zero under many circumstances, creating the need for multiple control horizons. The simplistic and short-sighted approach of selecting a maneuver

purely on the basis of its resultant Δg is found in practice to quickly reveal characteristic pitfalls of receding horizon control: poor stability and convergence. This outcome is unsurprising given the underlying dynamics and the disconnectedness of various goal regions through extended phase space — the spacecraft might easily end up devoid of further prospects at the end of the control horizon when making decisions in this way.

Aspects of long-term performance must then be taken into consideration somehow during the short-term decision making process. In RHC, this is typically accomplished by including a "cost-to-go" function in the objective that approximates the remaining control effort that will be needed beyond the horizon. When system properties permit such functions to be defined to monotonically decrease across configuration space as the reference state is approached, they can be incorporated into control laws to provably provide stability, convergence, and optimality.

In the small body mission problem, the structure of the system does not facilitate such rigorous guarantees, but nonetheless provides some characteristics that can be empirically demonstrated to provide these properties in many realistic scenarios. Due to the semimonotonic nature of the mission score s_m, mission progress cannot be lost unless failure occurs. Avoidance of failure can be assured by balancing safety margins against control authority and state estimation error levels and utilizing the reactivity paradigm to be described in Section 6.5.2. Under these conditions, controller stability can be empirically demonstrated.

Convergence of the receding-horizon planner to the completion state is a more nebulous prospect but is greatly aided by the high degree of connectivity in the small body mission problem's configuration space: one or two control inputs are sufficient for reaching most orbit locations from most other orbit locations via a wide variety of paths and phasings. After the spacecraft assesses reachability options from a sufficiently broad set of locations in extended phase space, it should eventually discover opportunities to reach all but the most obscure orbit regimes and therefore any goals with feasible levels of connectivity. This process could, however, require inordinately many planning cycles, motivating the definition of a timeout criterion to discard unacceptably

slow mission solutions.

$$\texttt{Timeout} = (s_m(t_k) > s_m(t_{k-\Delta k_{max}})) \tag{6.4}$$

While an accurate formulation of cost-to-go is not possible, the connectivity of various phase space regions to goal regions can be roughly assessed via intuitively motivated measures as a way of identifying favorable locations from which to execute maneuvers. The function evaluating this property, deemed the prospect heuristic $p_h(\mathbf{x}(t))$, defines a state-space field such that its value varies along each predicted trajectory and aids the selection of the arc termination epoch t_{k+1} for placing the spacecraft at a favorable location for achieving additional progress at low cost during the subsequent planning cycle. It is formulated here as a weighted and exponentiated sum of intermediary measures b from Section 2.2.3, evaluating properties such as Keplerian elements, energy levels, divergence rates, and general body-relative geometry.

$$p_h(\mathbf{x}) = \sum_{b \in B_h} w_b q_b \left(b; b^+, b^-\right)^{e_b} \tag{6.5}$$

$$B_h \subseteq \left\{ \overrightarrow{Q}, r, e, i, l, J, \ldots \right\} \tag{6.6}$$

Secondary to the use of p_h to improve convergence rates in terms of the number of planning cycles, minimization of fuel usage Δv and elapsed time Δt is also appropriate to consider during maneuver selection. A straightforward combination of these various concerns is used to define the horizon score s_h, synonymous with the decision score s used by the planner to decide upon a maneuver to implement.

Secondary Hierarchy Level
Purpose: Balance short-term gains and long-term prospects against costs
Variable: Horizon score AKA decision score $s \equiv s_h$

$$s_h(t) = \frac{\Delta g(t) + p_h(t)}{1 + w_v \Delta v + w_t \Delta t} \tag{6.7}$$

Solution: Maneuver $(t_k, \Delta \mathbf{v_k})$ that maximizes s_h across sample set of M'.

Decision design parameters are thus the cost weights (w_v, w_t), the weights and exponents $\{w_b, e_b\}_B$ of the prospect heuristic p_h, the exponent e_q that modulates the character of extended phase-space

gradients if $\vec{Q} \in B$. Calibration of these parameters is a balancing act between short-term progress and long-term performance and prospects. Effectiveness may only be determined empirically and no conclusions can be drawn about the deficit relative to a globally optimal solution.

6.3 Reachability Constraints

As was seen in the previous section, phase-space connectivity is a vital property for enabling efficient receding-horizon planning in the small body mission problem. Connectivity between an initial condition set $\mathcal{D}\left(\mathcal{U}; \mathbf{x}(t)\right)$ and a goal region $\mathcal{G}_i$ through ballistic motion is reflected by the size of the intersection

$$F\left(\mathbf{x}\left(\Delta\mathcal{T}\right) + \left(\mathbf{0}, \Delta\mathcal{V}\right); \Delta t_f\right) \cap \mathcal{G}_i\left(t, \left\{a^+, a^-\right\}_A\right) \tag{6.8}$$

The right hand term represents the region of extended phase space that allows progress to be accumulated for the i'th goal.

$$\mathcal{G}_i = \left\{(t, \mathbf{x}) \in (\mathcal{T}, \mathcal{X}) \;\middle|\; \texttt{Imageable}_i\left(t, \mathbf{x}\right)\right\} \tag{6.9}$$

This region, defined by Eq. 2.15, is sized by the sub-measure parameter ranges (a^+, a^-). It may be finite even in the temporal dimension through time-varying parameters such as the observation phasing angle ψ. More challenging goals with strict parameter bounds thus translate to lower connectivity, and as goals are completed the likelihood of an initial condition being connected to any incomplete goal decreases.

The left hand term represents the phase space volume swept out by the initial condition set during propagation via the system dynamics F, illustrating how reachability prospects additionally depend upon the spacecraft's initial state and allotted control authority, as well as the capabilities of the predictive model in terms of time and accuracy. The sizing of ΔV is physically limited by fuel availability, but also scales the size of the search problem along with its associated computational burden. The size of the set of initial delays $\Delta\mathcal{T}$ — the duration waited before executing some $\Delta v \in \Delta\mathcal{V}$ — has a similar toll on computing resources.

The final parameter affecting the size of the connective intersection is the maximal propagation duration Δt_f. Clearly, longer-duration motion allows for a more thorough covering of the extended phase-space with a single impulse, as the image of the initial condition set sweeps out additional volume. Practical constraints crucially limit the usage of arbitrarily long ballistic trajectories, however — computational expense is roughly proportional to trajectory duration, and reachability maps become much more complex in structure as the horizon increases, requiring higher resolution sampling. Error growth also becomes problematic over long durations unless separate closed-loop guidance is also applied. Thus, Δt_f must be limited in balance with the sizing of the search domain.

Further temporal constraints arise from the nontrivial compute time necessary to execute the control/planning law each cycle. An initial margin Δt_{min} accounts for the fact that the planner should not select a subsequent maneuver epoch that would arrive before its control input can be determined, nor should it demand use of spacecraft systems for GNC overly frequently. When considering uncertainty, this minimum interval may also be necessary for allowing state estimates to converge to a reasonable level of accuracy. In complement, a second margin Δt_{end} is applied to the end of the temporal planning domain to avoid pathological reachability prospects, e.g., undue difficulty in avoiding a would-be impact scenario just beyond the end of the prediction horizon. The interval of acceptable replanning epochs, which define the **next** planning epoch t_{k+1}, can then be stated as

$$\Delta \mathcal{T}_{+1} = (\Delta t_{min}, \Delta t_f - \Delta t_{end}) \tag{6.10}$$

For simplicity, $\Delta t_{end} = \Delta t_{min}$ is used in all cases.

All of these constraints define the context of the reachability search process detailed in Chapter 4. The search heuristic itself can thus be conceived as the third level of the hierarchy of automated decisions.

Tertiary Hierarchy Level
Purpose: Sample the highest-scoring regions of the reachability map
Variable: Simplex score $S\left(y\left(V\right)\right)$, e.g., Eqs. 4.11 and 4.12
Constraint: Modest total sample size and duration due to CPU limitations
Solution: Next sample set $\{\mathbf{u}_i\}_{N_k:N_{k+1}}$, biased toward regions of $\mathcal{U}$ producing high s_h values

The search score equation is a point-wise weighting represented in the simplex weighting function of Eq. 4.12, which provides a simplex score for use in simplex-wise weighting.

Beyond compliance with physical limitations, design at this level then consists of appropriately tailoring the search domain to increase likelihood of connectivity with goal regions without becoming infeasibly large to search effectively with limited computing resources.

At very low-mass objects, where fuel is of little concern, regions within line-of-sight could be reached quickly via high-energy paths. Phasing concerns aside, this could potentially allow rapid mission completion through "ping-pong" sequences of approximately hyperbolic trajectories. For generality of results, however, we neglect this reduction and instead focus on orbit regimes with osculating eccentricity below unity

$$\Delta v_{max}\left(\mathbf{x}\right) = \sqrt{2\mu/r} \tag{6.11}$$

This paradigm is also more amenable to accommodating the aforementioned temporal margins, among other spacecraft operation constraints.

The maximal propagation duration Δt_f can be simply set as a constant or, alternatively, as a function of each individual trajectory. For example, using the `Expire` criterion from Chapter 2,

$$\Delta t_f\left(\tilde{\mathbf{x}}\right) = \min\left\{\Delta t \;\middle|\; \texttt{Expire}(\tilde{\mathbf{x}}(t_k + \Delta t))\right\} \tag{6.12}$$

This more motivated formulation provides more uniform representation of risk across the reachability map, as well as more uniform expenditure of propagation efforts — which tend to scale with dynamical sensitivity.

6.4   Epoch Designation

Given a full predicted trajectory $\tilde{\mathbf{x}}(t)$ resulting from some sampled control input, a time series is obtained for each of the three score functions.

$$(\Delta t_k, \Delta \mathbf{v_k}) \xrightarrow{M} \mathbf{s}(t) = \begin{bmatrix} s_m(t) & s_h(t) & s_s(t) \end{bmatrix}^T \tag{6.13}$$

However, each series must be reduced to a scalar to allow decision-making, and the subsequent planning epoch t_{k+1} must somehow be designated. The bottom level of the decision hierarchy meets these needs by translating from the continuous time domain t into discrete control epochs k. For each sampled control input this policy T, which was first referred to in Eqs. 3.7–3.10 applies the temporal reduction

$$(s_m(t), s_h(t), s_s(t)) \xrightarrow{T} \left(\Delta t_{k+1}, s'_m, s'_h, s'_s\right) \tag{6.14}$$

as in Eqs. 3.5–3.6 using $s_i = s_h$ via the decision process at the bottom of the hierarchy:

Quarternary Hierarchy Level
Purpose: Determine best time at which to begin next planning cycle
Operation: Reduce score time series via T map

$$s'_s = \max_t s_s(t) \tag{6.15}$$

$$\left(s'_h; \Delta t_{k+1}\right) = \max_{\Delta t \in \Delta \mathcal{T}_{+1}} s_h(t_k + \Delta t) \tag{6.16}$$

$$s'_m = s_m\left(t_k + \Delta t_{k+1}\right) \tag{6.17}$$

Solution: Scalarized scores and planning epoch t_{k+1}

A sampled trajectory may have an empty termination interval $\Delta \mathcal{T}_{+1}$ if $\Delta t_f < \Delta t_{min} + \Delta t_{end}$; in this case, $s'_h = 0$ is assigned.

6.5   Uncertainty Mitigation

Section 2.2.3.1 described a technique for modifying the predictive model to reflect the worst-case outcome under linear growth of initial positional and velocity errors. As will be seen in Chapter 7, it is ineffective and impractical to attempt to mitigate uncertainty solely by increasing

the robustness of these predictions. To effectively complement robustness by handling the occasional occurrence of larger-than-anticipated errors, the receding-horizon execution of robust plans includes an ability to react to such deviations by expediting the next planning cycle.

6.5.1   Error Sources

Apart from the planner's design parameters, the map from maneuver options to reachable scores also relies upon the initial state and the definitions of the dynamical model and mission objectives; the expected horizon score of the trajectory can be parameterized as $s_h\left(\mathbf{u}; \mathbf{x}_0, \mathcal{P}_\nu, \{a^\pm\}_A\right)$. However, under typical position and velocity errors with radial standard deviations σ_r and σ_v, the true initial state differs from that used for maneuver design by:

$$\hat{\mathbf{x}}_0 = \mathbf{x}_0 + \delta\mathbf{x} \tag{6.18}$$

$$\delta\mathbf{x} \in \mathcal{N}^3\left(\sigma_r/\sqrt{3}\right) \times \mathcal{N}^3\left(\sigma_v/\sqrt{3}\right) \tag{6.19}$$

with $\mathcal{N}$ denoting normal distributions.

Furthermore, the true flow across phase space differs from the predicted flow due to errors in the dynamical model. This thesis considers only variation of the polyhedron shape $\mathcal{P}_\nu$, while presuming that the estimated gravitational parameter μ is accurate, and no attempt to directly express deviations caused by incorrect $\mathcal{P}_\nu$ is made. Instead, operating under the assumptions that the inaccuracies of a low-resolution shape model produce a roughly stochastic effect upon motion deviation and that the true density distribution is uniform, mitigation of modeling errors is handled via adjustment of the same parameters governing mitigation of state errors.

When operating under uncertainty, the actual goal attainment $g\left(\mathbf{x}_0, \Delta\mathbf{v}\right)$ may vary from the expected value $\hat{g}\left(\hat{\mathbf{x}}_0, \Delta\mathbf{v}\right)$, jeopardizing the planner's ability to fulfill its ultimate purpose. Accordingly, this deviation will be the central focus of the mitigation techniques.

6.5.2 Reactivity

When simulating the online mission design process, reachable trajectory predictions are propagated using an estimated initial state and a polyhedral gravity model with low resolution $\hat{\nu}$. During the execution phase in between planning cycles, the truth state is propagated with high model resolution ν. State estimation error is simulated by adding noise $\delta\mathbf{x}$ from the probability distribution of Eq. 6.19 to the true state $\mathbf{x}$. Along with the nominal planned position $\mathbf{r}^*$, this produces trajectory estimate $\hat{\mathbf{x}}(t)$, online surface-range estimate $\hat{\rho}_{\mathcal{P}}(t)$ and the estimated deviation magnitude $\delta\hat{r}(t)$.

$$\hat{\mathbf{x}}(t) = \mathbf{x}(t) + \delta\mathbf{x} \tag{6.20}$$

$$\hat{\rho}_{\mathcal{P}}(t) = \min \rho(\hat{\mathbf{r}}(t), \mathcal{P}_{\hat{\nu}}) \tag{6.21}$$

$$\delta\hat{r}(t) = \|\mathbf{r}^*(t) - \hat{\mathbf{r}}(t)\| \tag{6.22}$$

The reactivity paradigm uses the latter two derived values to trigger maneuver execution in advance of the nominal control epoch t^* determined by the original plan.

A safety divert epoch t^*_{div} is determined as the first actionable time at which the robustness-cushioned `Danger` criterion of Eq. 2.30 is violated.

$$t^*_{div} = \min\left\{ t \in (t_0 + \Delta t_{min}, t^*) \ \Big| \ \text{Danger}\left(\hat{\mathbf{r}}(t), d\left(\hat{\mathbf{x}}(t)\right); \rho_{\mathcal{P},min}\right) \right\} \tag{6.23}$$

If this criterion does not occur, t^*_{div} is an empty set and no divert reaction is triggered.

Alternately, a reaction is also warranted if $\delta\hat{r}$ exceeds the tolerance d to which the robust goal-fulfillment prediction remains valid. These correction maneuvers are triggered with a slightly more complex logic dependent on the time t_g at which the planned objective fulfillment is completed:

$$t_g = \underset{t \in (t_0, t^*)}{\arg\min}\, g(t) == g(t^*) \tag{6.24}$$

$$t^*_{corr} = \underset{t \in (t_0 + \Delta t_{min}, t_g)}{\arg\min}\, \delta\hat{r}(t) > d(t) \tag{6.25}$$

If a deviation violation occurs before Δt_{min} has elapsed, it is unavoidable, and if it occurs after t_g, it is inconsequential; violations that do not fall within this time span do not trigger a reaction.

Ultimately, the applied maneuver epoch is

$$t_{k+1} = \min\{t^*, t^*_{div}, t^*_{corr}\} \qquad (6.26)$$

such that $t_{k+1} \in [t_0 + \Delta t_{min}, t^*]$.

6.6   Complete Algorithm

After time series computation of $\mathbf{s}(t)$, decisions propagate in reverse order, ascending the hierarchy. The bottom level translates sampled inputs into trajectories $\tilde{\mathbf{x}}(t_k, t_{k+1})$ with time-reduced scores $\mathbf{s}'$; these govern additional sampling of the control domain; the sampled maneuver with the highest horizon score s'_h is implemented; and the process is repeated until the mission either fails or finishes.

Algorithm 2: Receding-horizon mission planning

1   <u>function RHMP</u> $\left(t_0, \mathbf{x}_0, M, \hat{M}, W(V), \mathcal{U}(\mathbf{x})\right)$;

    Input   : Initial state $(t_0, \mathbf{x}_0)$, truth model M, erroneous model $\hat{M}$, search heuristic $W(V)$, and domain generation rule $\mathcal{U}(\mathbf{x})$

    Output: Solution profile $(\tilde{\mathbf{x}}, \tilde{\mathbf{y}}, \tilde{\mathbf{s}})_{t,K}$

2   $k = 0$;

3   **while not** (Complete **or** Failure) **do**

4      $\mathcal{U}_k \leftarrow \mathcal{U}(\mathbf{x}_k)$;   // assign control domain

5      $(\mathcal{M}, \{\mathbf{s}'_i, t'_i\}) \leftarrow \text{ReachMap}\left(t_k, \hat{\mathbf{x}}_k, \mathcal{U}_k, \hat{M}, W(V)\right)$;   // search with erroneous info

6      $(s^*_h, \mathbf{u}^*)_k = \max\limits_{\mathbf{u}\,\in\,\mathcal{M}} s'_h(\mathbf{u}; t_k, \mathbf{x}_k)$;   // select top-performing maneuver

7      $(\tilde{\mathbf{x}}, \tilde{\mathbf{y}}, \tilde{\mathbf{s}})_{t+\Delta t, f} \leftarrow M(t_k, \mathbf{x}_k, \mathbf{u}^*_k; t^*)$;   // integrate with truth state, model

8      $(\hat{\mathbf{x}}(t), \hat{\rho}_{\mathcal{B}}(t), \delta\hat{r}(t)) \xleftarrow{\text{Eqs.6.19−6.22}} \left(\tilde{\mathbf{x}}^*, \tilde{\mathbf{x}}; \hat{\mathcal{B}}, \sigma_r, \sigma_v\right)$;   // estimate deviation risks

9      $t_{k+1} \xleftarrow{\text{Eqs.6.23−6.26}} (\hat{\rho}_{\mathcal{B}}(t), \delta\hat{r}(t))$;   // reactively set replanning epoch

10     $(\mathbf{x}_{k+1}, \hat{\mathbf{x}}_{k+1}) \leftarrow (\mathbf{x}(t_{k+1}), \hat{\mathbf{x}}(t_{k+1}))$;   // advance truth/estimated states to next epoch

11     $k \leftarrow k + 1$;   // advance epoch index

12 **end**

Inputs M and $\hat{M}$ are implied to carry many parameters that may also be used outside of the predictive model, such as the erroneous body model $\hat{\mathcal{B}}$ among others. The completion criterion comes directly from the mission score while the failure criterion is composed of safety constraint

violations and the timeout check.

$$\texttt{Complete} = (s_m == 1) \tag{6.27}$$

$$\texttt{Failure} = (\texttt{Impact or Escape or Timeout}) \tag{6.28}$$

An error-free version of the algorithm is alternately shown in the diagram of Figure 6.1. The function ReachMap in line 4, which comes from Algorithm 1, is represented within the dotted lines of the diagram, where N is the running count of sampled control inputs and N_f is the desired final sample size.
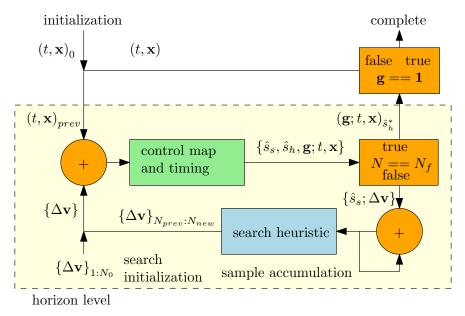
Figure 6.1: Autonomous planning algorithm for small body mission problem, formulated as receding horizon controller, assuming no uncertainty.

Chapter 7

Full-Mission Analysis

Given the receding-horizon planning framework developed in Chapter 6, this chapter will present several analyses of the complete planning tool's behavior and performance. Each uses a small Monte Carlo solution set to account for nondeterministic components of each planner — namely the weighted random sampling of mesh elements for subdivision — and random state error in many cases.

The first analysis is focused upon the influence of the system upon the qualitative properties and variability of solutions. Here, the configuration of the planner is held constant while the system dynamics and mission requirements are altered. Next, state and model error are introduced and the influence of the robustness parameter upon convergence and general behavior is checked. Finally, the robustness parameter is fixed and two other aspects of the planner are varied: the importance of the prospect heuristic is illustrated by disabling different components within it, and alternately the cost weights in the decision function are adjusted to show that total fuel cost and total mission duration can be traded off against each other.

7.1   Variation of the Problem

Qualitative evaluation of small body mission solutions generated by the autonomous planner is difficult due to the vast difference between the dynamics and mission requirements as compared to more conventional mission design problems. To facilitate an understanding of the complexity, sensitivity, and variability of solutions in the small body problem, results are shown in this section

for the sequence of problems Sphere, Half-Ito and Ito-Hard from Table 2.2, beginning with the simple Sphere baseline paired with time-invariant objective constraints. This can be analogized with the Keplerian reachability maps in Chapter 3 and the gradual increase in map structure as perturbations were added and amplified.

Non-deterministic components of the planner are found to produce diverse solution paths through the state space and goal space alike, implying high sensitivity of the planner regardless of its ability to ultimately converge to the `Complete` state.

The prospect heuristic $p_h = q_r \left(r; 2\bar{R} \right) / 2$ was selected to encourage execution of maneuvers at an orbit radius of two mean central body radii, but to value the satisfaction of this criterion lower than the completion of a single goal. Fuel usage was penalized with $w_v = 1/10$ and control domains were generated with $\mathcal{U}\left(\mathbf{x}\right) = \mathcal{U}_{sph}\left(\sqrt{2\mu/r} \right)$. Each combination of physical systems and phasing constraint was simulated from an identical initial state for a Monte Carlo set of $n = 100$ trials using a heuristic search resolution of $N_f = 5000$ samples. Neither an increased trial count of $n = 200$ nor an increased search resolution of $N_f = 25000$ were found to produce significant differences in mean performance measures for a subset of test case scenarios checked to inform the selection of nominal values.

7.1.1   Typical Mission Profiles

To qualitatively reveal the behavior of the planner under each setup, typical solutions are first examined. One such physical-space profile for the unphased Sphere case is plotted in Figure 7.1. Here, under Keplerian dynamics and purely geometric objective constraints, even the weak weighting of the cost Δv in the decision function is sufficient to produce behavior reminiscent of traditional mission design. Operations occur within a fixed inertial orbit plane — plane-changes are expensive and should be avoided when possible — with only minor changes to orbit semimajor axis for phasing. The mission is completed after seven control horizons.

As is evident in Figure 7.2, plane-changing maneuvers are occasionally selected by the planner when observation phasing constraints are added, despite the Keplerian dynamics. This is likely

(a) Body frame

(b) Inertial frame
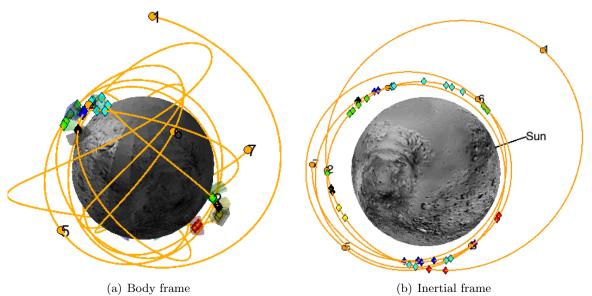
Figure 7.1: Mission profile for Sphere system without observation phasing requirements. Diamonds denote bounds of observation arcs.

attributable to the length of the time horizon employed; a highly inclined orbit at the correct radius would eventually satisfy any goal at that radius, barring special cases of certain orbit periods commensurate with the body rotation period. Nonetheless, these modifications of the orbit inclination and radius are still relatively rare and the total maneuver count increases modestly to ten.

Orbital motion about the triaxial central body necessarily involves plane-changes even in the absence of objective phasing constraints. As seen in mission profile of Figure 7.3, this occurs naturally due to the non-Keplerian dynamics; cross-track maneuver components are again minimal as in the unphased spherical case, and the maneuver count drops back to single digits.

Once phasing constraints are combined with the triaxial dynamical model, solutions become highly complex as seen in Figure 7.4. A total of 17 maneuvers are required, and large variations of the orbit plane occur over the course of the mission. Many of these are still attributable to the natural dynamics rather than the control inputs; this demonstrates the planner's adeptness at leveraging, rather than merely overpowering, the unintuitive non-Keplerian natural motion.

Ultimately, the degree of complexity of the physical-space behavior is irrelevant as long as the planner produces a goal-space trajectory from the "lower left" corner $\mathbf{g} = \mathbf{0}$ to the "upper

(a) Body frame

(b) Inertial frame
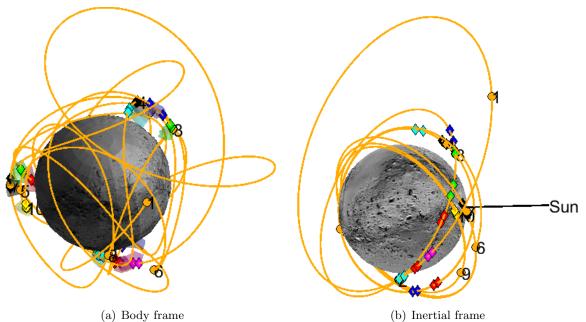
Figure 7.2: Mission profiles for Sphere system with observation phasing requirements. Diamonds denote bounds of observation arcs.

(a) Body frame

(b) Inertial frame
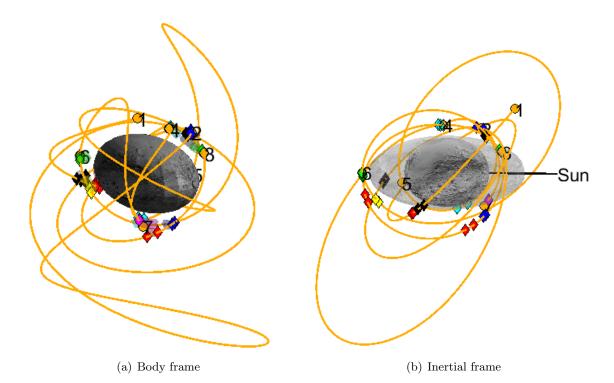
Figure 7.3: Mission profiles for Ito-Hard system without observation phasing requirements. Diamonds denote bounds of observation arcs.

(a) Body frame   (b) Inertial frame
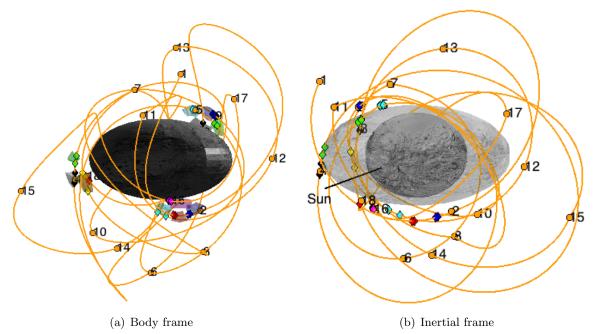
Figure 7.4: Mission profiles for Ito-Hard system with observation phasing requirements. Diamonds denote bounds of observation arcs.

right" corner $\mathbf{g} = \mathbf{1}$. This can be inferred in all of the above examples by the passage of trajectories through all geometric constraint regions in the body frame and the contemporaneous inertial-frame orientation of the spacecraft on the Sun-side of the body when phasing requirements are imposed, as revealed by the diamond markers.

7.1.2   Mission Profile Diversity

A central question about the mission design scheme is its level of determinism — the degree to which chaoticity in the physical dynamics and complexity in the abstraction dynamics cause sufficient sensitivity in the full dynamical map to produce distinct trajectories $\tilde{\mathbf{g}}$ upon repeat runs with identical initial conditions. An indicator of the diversity of a Monte Carlo set of n such trajectories is formulated using the mission score $s_m \in [0, 1]$ as the independent variable and first defining the difference trajectory for two missions i and j:

$$\delta g_{ij}\left(s_m\right) = \left|\mathbf{g}_i\left(s_m\right) - \mathbf{g}_j\left(s_m\right)\right|_1 \tag{7.1}$$

The solution diversity indicator is then defined as the average of all unique trajectory pair differences

$$\overline{\delta g}\left(s_m\right) = \left(\frac{2}{n_g}\right)\left(\frac{2}{n\left(n-1\right)}\right)\sum_{i=0}^{n}\sum_{j=i+1}^{n}\delta g_{ij}\left(s_m\right) \tag{7.2}$$

where the additional normalization divisor $n_g/2$ is the theoretical maximum solution diversity for Monte Carlo sample size $n \to \infty$.

The solution diversity indicator, plotted in Figure 7.5(a) for each test case, illustrates that more complex underlying dynamics produce a far richer set of potential solutions despite ultimate convergence to the same desired end state. In scenarios without phasing requirements, the degree of central body triaxiality exhibits a clear correlation with solution diversity. Introduction of phasing requirements raises diversity across the board, with maximally diverse results occurring for the phased Ito-Hard case. A reference diversity curve computed for a set of random walks through the goal space, constrained only to monotonically increase s_m to 1, approximates the upper bound of the diversity indicator.
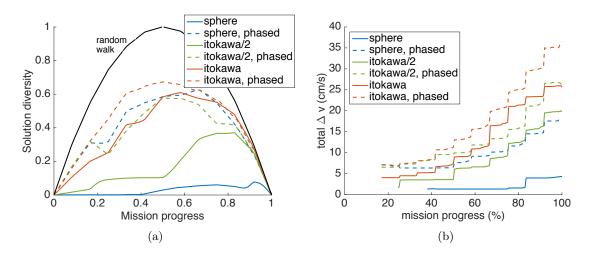
Figure 7.5: Performance variation under each combination of Sphere, Half-Ito, and Ito-Hard systems with unphased and phased observations. (a) Diversity in Monte Carlo sets of solution trajectories through goal space. (b) Mean fuel expenditure for each Monte Carlo set.

Of secondary interest are trends in control energy expenditure, plotted in Figure 7.5(b). These results show that both the complexity of the physical dynamics and the strictness of the goal specifications are associated with additional demands in control energy. However, as the

expenditure of Δv was weighted only weakly in the decision function s to avoid complications with very long-duration missions, the result is not directly indicative of the possible lower bounds of fuel costs. What is primarily indicated is that for a non-spherical body, a fixed-altitude observation pass is associated with a different orbit radius and orbit energy level depending upon the location of the observation target point. Accessing multiple such points therefore requires traveling between more diverse regimes of the physical state space than for the Keplerian equivalent of the same mission.

7.2   Uncertainty and Robustness

Next, state and model error are incorporated to compare and contrast uncertainty mitigation strategies, i.e., varied values of ζ or η to preferentially rely more so on robustness or reactivity. To isolate these effects, the 67/P-Obs problem is used in conjunction with a fixed formulation of the decision function. The function uses prospect heuristic weights at $w_r = w_l = w_{\vec{Q}}/2 = 1/4$ for quality measures regulating the radius to $2\bar{R}$ and the latitude to $-90°$ (see Figure 5.4 for motivation), with an exponent $e_{\vec{Q}} = 4$ to de-weight less promising prospective quality values. Cost weights are fixed at $w_v = \Delta v_{max}/10$ and $w_t = \Delta t_{f,max}/100$. Mitigation behavior can be made transparent by classifying each maneuver in terms of its motive and effectiveness. Four categories of maneuver are defined:

Aimless: the full nominal path is traveled, but it does not achieve any objectives.

Safety Divert: an early maneuver was executed in reaction to occurrence of `Danger`.

Correction: an early maneuver was executed to correct deviation from an objective.

Goal Progress: the full nominal path is traveled, including completion of some objectives.

The synergistic behavior of the robustness paradigm and the reactivity paradigm is first studied realistically-motivated levels of state error $\sigma_r = 10$ m, $\sigma_v = 1$ mm/s by adjusting the threshold of robustness; reactive execution picks up as much slack as necessary when predictions are insufficiently robust. Afterward, a low-robustness planner and a high-robustness planner are

each tested under increasing levels of velocity uncertainty up to $\sigma_v = 15$ mm/s in order to represent behavior under diminished navigation performance or at very small bodies where a fixed uncertainty level would be proportionally more consequential. Effects of shape model error are also briefly addressed, informing a design trade-off between the computational cost and error levels associated with the choice of predictive model fidelity.

7.2.1 Monte Carlo Solution Set

Performance for each combination of planner parameterization and error level is assessed via a Monte Carlo analysis of 50 mission trials, with variability originating both from random error values and from random elements in the limited $N_f = 1000$-sample heuristic search of the reachability map. The values set for safety requirements and control authority, i.e., $\rho_{\mathcal{P}}^-$, Δv_{max}, were sufficient to prevent any occurrences of impact whatsoever despite a generous re-planning duration $\Delta t_{min} = 3.5$ hr. Furthermore, the low control energy cost weighting w_v resulted in little variation between the mean results of total fuel costs in uncertain missions; cases with error averaged roughly 5 m/s, dropping to 2 m/s when no state error was present. These highly feasible values justify the de-emphasizing of this type of cost when calibrating the weights of the decision function. Computing time averaged about 2.5 minutes per planning cycle and peaked below 4 minutes on a 3 GHz Intel Xeon processor.

Given these outcomes, the primary indicator of performance is the total effort of applying the online mission design scheme. Total maneuver counts are used to represent effort expended by a planner since computational expense and fuel cost per planning cycle were not optimized or tuned on a per-planner basis.

Some combinations of mitigation parameter values and error levels resulted in slow convergence and inordinately extensive missions. These simulations were terminated early via `Expire` with $\Delta k_{max} = 10$. Planner effectiveness can then be inferred either from the average maneuver count per solution or from the rate of occurrence of solution timeouts, with the implication that timed-out runs would have eventually produced complete solutions with higher maneuver counts

had they been allowed to continue.

7.2.2   Varying Mitigation Parameters

Performance is first assessed as a function of uncertainty mitigation parameters, i.e., constant or divergence-scaled formulations of the anticipated deviation to which predictions are made robust. Mission completion rates and maneuver counts are both plotted in Figure 7.6 for planners that use varying levels of constant anticipated deviation $d = \zeta$ or dynamic anticipated deviation $d = \eta\Lambda$. A breakdown of the relative incidence of each category of maneuver is also given per planner. Middle-ground levels of robustness are found to produce the highest success rates and lowest maneuver counts for both types of planner. The η class of planners showed stronger performance overall, with lower maneuver counts and perfect success rates for the parameter range $0.75 \leq \eta \leq 1.5$.
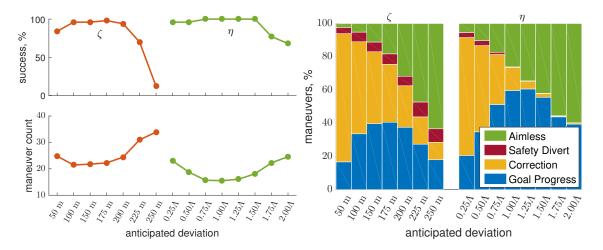
Figure 7.6: Planner performance and control behavior under a variety of error mitigation parameterizations.

Meanwhile, maneuver categorization clearly demonstrates the manner in which the uncertainty mitigation parameters influence behavior. Low η or ζ imply low robustness in that the nominal result can be lost under only a modest deviation from the planned course; low-robustness planners consequently impart many more reactive control epochs. High-robustness planners are seen to more consistently stick to the plan, but are less frequently able to formulate a plan that completes objectives. At all levels of robustness, a higher incidence of "goal progress" maneuvers

is seen for the η class of planners than the ζ class — a maximum of 60% as compared to 40% — while the share of "aimless" maneuvers is roughly unchanged.

7.2.3 Mission Profiles

Despite the high degree of variability between solution profiles within any Monte Carlo trial set, the general differences in character between alternate planner formulations can still be seen in the physical mission profiles. Figure 7.7 shows examples of this for a high-robustness planner and a low-robustness planner. Both planners produce successful missions; however, the more robust planner mostly executes maneuvers in the region most highly valued by the prospect heuristic. The less robust planner executes a similar number of maneuvers in this region, but must supplement them with many additional reactive maneuvers en-route to objectives.

The time histories of Figure 7.8 provide further behavioral indicators. Vertical bars indicating the timing of maneuvers show that the low-robustness planner almost always executes controls as frequenty as allowed when it has an objective in sight. The more robust planner maintains an orbit inclination at around 90°, as is encouraged by the prospect heuristic; the other occasinally varies into retrograde regimes. Both planners avoid prograde motion, likely due to the precarious effects of orbit resonances.

7.2.4 Varying Uncertainty Level

To reveal the interaction of the degree of robustness with the degree of error, a low-robustness $\eta = 1/4$ and a high-robustness $\eta = 1$ planner are compared in Figure 7.9 for several values of initial velocity uncertainty. Also plotted are two datasets using $\sigma_r = \sigma_v = 0$, one of which additionally uses $\hat{\nu} = \nu$, i.e., zero model error. These show that the planning scheme is extremely effective in the absence of uncertainty, attaining progress with almost every control input, and that shape model resolution reduction from 2500 vertices to 64 incurs only a minor performance penalty.

Counter to the initial result, a lower degree of robustness appears preferable under large state uncertainty. Examination of Eq. 2.24 helps to reveal the cause of this phenomenon: increasing σ_v

(a) Rotating, $d = \Lambda$

(b) Inertial, $d = \Lambda$

(c) Rotating, $d = \Lambda/4$

(d) Inertial, $d = \Lambda/4$
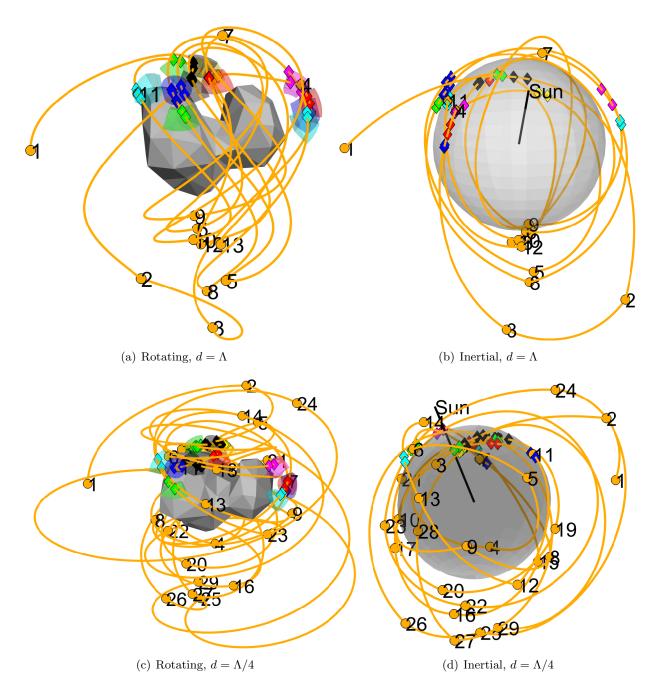
Figure 7.7: Characteristic mission profiles generated with two different levels of robustness. Diamonds indicate imaging arcs; numbered circles indicate maneuvers.

(a) $d = \Lambda$

(b) $d = \Lambda/4$
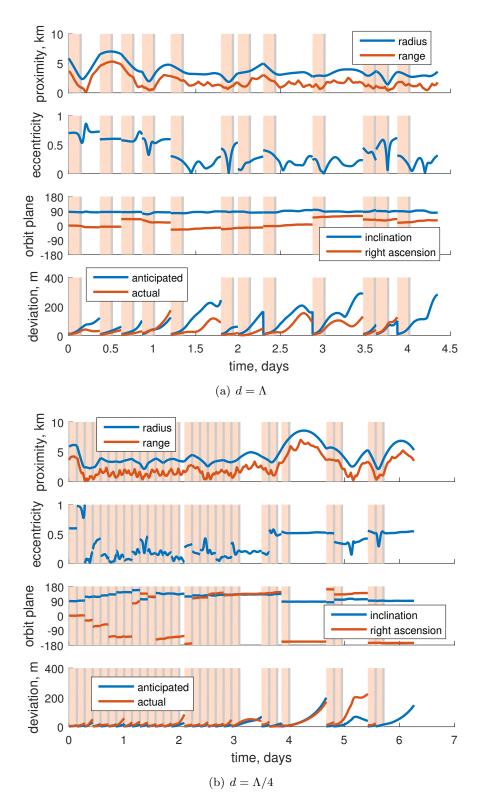
Figure 7.8: Evolution of several quantities in solution profiles generated using two different levels of robustness. Vertical bars indicate control epochs and minimum replan times.
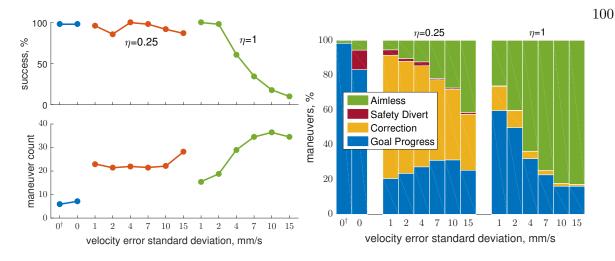
Figure 7.9: Planner performance and control behavior under varying levels of velocity error. †no model error.

has a similar negative effect upon robust reachability prospects to increasing η, so either way of producing a large product $\eta\sigma_v$ causes a dearth of opportunities for robust goal attainment. This is also reflected in the heightened occurrence of "aimless" maneuvers for the $\eta = 1$ planner, similar to the trend of Figure 7.6 under small σ_v and large η.

The high success rates of the low-robustness planner imply that sufficiently frequent correction maneuvers can effectively mitigate very large errors so long as the planner continuously targets goal progression, a behavior that is encouraged by the overconfidence that results from small anticipated deviations.

7.3   Planner Design

Having established the influence of the physical system, the mission specifications, and the interaction of uncertainty levels with mitigation paradigms, variation of the decision function of Eq. 6.7 is finally addressed. This function is re-stated below with a prospect heuristic substituted in that depends upon radius quality q_r, latitude quality q_l, and forward quality $\overrightarrow{Q}$, all of which are parameterized as in the previous example and evaluate to within the range $[0, 1]$.

$$s\left(t\right) = \frac{\Delta g\left(t\right) + w_p \left(q_r\left(t\right) + q_l\left(t\right) + 2\overrightarrow{Q}\left(t\right)^4\right)}{1 + w_v \Delta v + w_t \Delta t\left(t\right)} \tag{7.3}$$

The prospect heuristic in the numerator and the direct influence of cost penalties in the denominator are assessed separately.

Two approaches are taken to verify and tune the influence of the heuristic, with cost penalties fixed at $w_v = 0.1/\Delta v_{max}$ and $w_t = 0.01\Delta v_{max}$. First, $w_p = 0.01/n_g$ is used and the three individual components q_r, q_l, and $\vec{Q}$ are switched on or off. This data series, the first shown in Figure 7.10, demonstrates the importance of all three components: when all are present, success rates are 98% or higher, while the absence of any drops this number to the 90-95% range. When more than one heuristic is absent, the success rate drops as low as 75%, and when both q_r and q_l are omitted, no trial completes successfully. Average maneuver counts increase by a third when q_l or $\vec{Q}$ are not used, while total fuel cost rises by 15-20%. Omission of q_a does not raise these costs but is nonetheless influential upon success rate.

Secondly, with all three heuristic components present, the weight w_p is increased. At $w_p > 1/(2n_g)$, the heuristic's influence begins to overpower that of the objective sufficiently to alter the control choice $\Delta\mathbf{v}$, and the success rate plummets. At smaller w_p values, performance is seen to remain consistently favorable in all aspects except total mission duration, which increases substantially likely as a result of its very mild cost weighting. It thus appears that the prospect heuristic works best as a method of influencing maneuver timing t_{k+1} without significantly altering the choice of $\Delta\mathbf{v}$. This arises from the independence of timing relative to results in terms of the fuel cost, which is fixed for a trajectory's entire duration, and the objective increment, which generally is approximately a step function that effectively sets the lower bound of the time span upon which the maximization of the prospect heuristic is conducted.

Three additional data series reveal the influence of cost weights w_v and w_t while the heuristic weight is fixed at $w_p = 1/(4n_g)$. Findings are entirely intuitive — at modest cost weights, perfect success rates are achieved and fuel cost can be proportionally traded off against total duration. When the influence of cost terms becomes too large, success rates suffer as too many opportunities for progress are missed in favor of keeping short-term costs low. It is hypothesized that fuel costs could be driven even lower if the timeout criterion were relaxed, while a similar result in terms of

duration cost seems unlikely due to hard temporal bounds on objective reachability that arise from both the sizing of the control domain and from solar phasing requirements.

(a) prospect heuristic weights

(b) cost weights
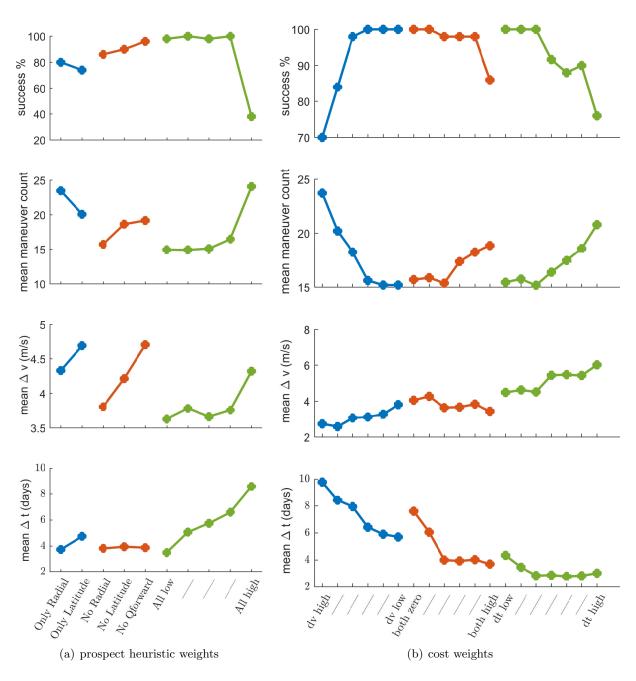
Figure 7.10: Performance results for Monte Carlo mission simulation sets using varied decision function parameters.

Chapter 8

Discussion

This final chapter is structured to interleave the specific findings of the dissertation with commentary about their broader context and implications, leading to potential avenues of future work and inquiry. Each section discusses one of the four major components of the research: the predictive model, the reachability analysis, the receding-horizon scheme, and the uncertainty mitigation features. Subsections focus upon specific aspects of each component and strive to answer three questions: what can be assessed from the available results, what assumptions and limitations must be kept in mind, and what future steps might be taken to address those factors and extend functionality? Lastly, a high-level summary of results and their contribution to the field is made in conclusion.

8.1 Problem Specifications

Successful demonstration of the autonomous planning algorithm is in significant part attributable to the manner in which the problem setup was posed in Chapter 2 and to the properties inherent in the class of systems investigated. The combination of a sampling-based planning scheme with a layer of objective abstraction allowed for both flexibility and complexity when generating solutions, while the control strategy and physical dynamics synergized effectively to allow a high degree of phase space connectivity that aided in achieving convergence and avoiding failure or pathological behaviors. This mixture of highly generalizable concepts and tools with relatively unusual system traits thus makes it difficult to predict the extensibility of the approach to dissimilar

problem domains; nevertheless, extrapolation to variations of the small body orbiter problem can be drawn with some confidence.

8.1.1   Dynamics Modeling

The "black box" nature of the sampling-based tool readily accommodates many types of physical forces that could be crucially influential in small body exploration scenarios but are not amenable to mathematical analyses. In the test cases investigated, the primary example of this was the nonanalytic gravitation of the irregularly shaped central bodies. Nonautonomous, i.e., time-parameterized, forces such as asynchronous SRP and third-body gravitation were also present in some analyses.

By conducting a single pre-integration of natural system behavior, the predictive model could readily incorporate non-principal rotation of the central body or even the complex motion of two interacting irregular members of a binary system. Nonconservative forces such as drag from comet outgassing plumes could be included and potentially even exploited to change the spacecraft's energy level without additional fuel cost. The predictive framework could also allow alternate control schemes such as low thrust applied at a constant magnitude over finite durations, under sufficiently simple time-parameterization of pointing.

This flexible paradigm is primarily limited by the computational complexity of the model components rather than their mathematical properties. Other potential hindrances can ultimately be related back to this fundamental resource. For example, the general smoothness of the utilized force functions contributed to the applicability of the hill-climbing component in the reachability set search heuristic; however, forces with stiff functional forms such as focused outgassing plumes or SRP with shadowing could likely be accommodated with an increase of sampling resolution or other enhancements to the search technique.

8.1.2   Objective Modeling

By layering high-level objectives directly on top of physical behavior, the traditional mission design question of designing a target "science orbit" compatible with high-level objectives is abstracted away in the predictive model, no longer distinct from the design of orbit transfers and correction maneuvers. This reduces the human burden in mission design in terms of locating feasible solutions as well as in assessing trade-offs between conflicting objectives — different science tasks can be quantifiably balanced against asymmetric risks and costs through the formulation and tuning of the decision function. Furthermore, it allows these high-level decisions to be made on-the-fly in response to unforeseen opportunities in an environment that changes rapidly in proportion to the time scales of interplanetary communication.

As with the modeling of physical dynamics, mission requirements and objectives could also be made more comprehensive and sophisticated, limited only by computational feasibility. Violation of constraints such as maintaining unobstructed line-of-sight with the Earth for communications and with the Sun for solar power would manifest simply as additional non-permissible regions in the control domain, along with the impact and escape sets. Alternate high-level mission goals could include global imaging coverage or frequent and minimally-controlled traversal through particularly sensitive regimes to estimate a high-fidelity system model for scientific analysis.

8.1.3   Phase Space Connectivity

The solubility of the small body orbiter problem via short-horizon sampling is facilitated by the high degree of phase-space connectivity inherent to orbital systems, where motion is the norm, stillness the exception, and attractors generally do not exist. Combining a proportionally large amount of control authority with this rich natural motion affords a high degree of reachability in close-proximity orbit regimes. As a result, challenging goal sets were found to be reliably fulfillable using simple prospect heuristics that were not tailored to the goals with much specificity.

Greater density and accessibility of objective regions corresponds to broader opportunities

for mission progress, allowing a planner to pick the least costly of multiple favorable paths. Ever more ambitious goals, with more narrowly constrained parameters and closer proximity to the body surface or other inadmissible regions, shrink the connectivity of objective-fulfilling trajectory families with some of the more desirable general classes of orbits, e.g., those whose osculating eccentricity remains low over extended time spans. This conversely decreases the ability to reach goals and minimize costs, thus impeding performance of a planning scheme that lacks provably convergent heuristics or higher-dimensional reachable sets such as would reflect prediction of multi-maneuver sequences. A finite objective set, as was used in this study, also results in a narrowing of prospects as missions progress and fewer objectives remain — indeed, most timeout occurrences in the Monte Carlo analyses of Chapter 7 occurred after a considerable majority of objectives were complete.

An alternative mission concept could involve the continuous uploading or onboard designation of new objectives, in which case steady-state planner performance could be evaluated at a conistent level of objective reachability as expressed in Eq. 6.8. Furthermore, the automatic formulation of more objective-specific prospect heuristics could serve as an improved substitute for the preferable but computationally infeasible usage of multi-step reachability search. By defining a "home manifold" orbit family associated with the prospect heuristic and assessing its connectivity with individual objectives under practical energy bounds, mission feasibility under that prospect heuristic might be judged *a priori*.

8.2   Reachability Search and Mapping

The core component of the planning algorithm — efficient numerical reachability analysis, as detailed in Chapter 4 — is also a focal point for questions of feasibility and practicality for real-world implementation. Beyond the computational cost of force and objective model evaluations, which was discussed above, runtime efficiency of the planner also hinges upon the sizing of the control domain to be searched and upon the specifics of how the search is executed. Individual optimization of each of these aspects is crucial for minimizing usage of computing resources, in

addition to the balancing of their allocation, e.g., trading off the size of the control domain covered against the accuracy with which it is resolved.

8.2.1   Reachable Domain

For the most part, the search trials in this research effort have utilized large control domains that could permit reversal of the direction of motion and access to a broad swath of osculatingly bounded energy levels; results thus represent an upper bound on the contribution of the velocity-space size of the domain to the computational burden of the search process. These large domains are well within reason for typical spacecraft maneuvering capabilities at low-mass bodies, and are also informative of other questions directly relating to the realities of the physical propulsion system, e.g., revealing the risks of under-performing maneuvers by considering outcomes across the entire range $(\mathbf{0}, \Delta\mathbf{v})$.

Converse to velocity-space bounds, the temporal bounds of predictions have a less clear hard limit on their utility. While robustly-achievable outcomes naturally have a limited lifespan via the Expire condition, this only reflects what can be achieved without corrective re-planning; further-sighted predictions can still provide beneficial information through the prospect heuristic and particularly the prospective quality $\overrightarrow{Q}$. However, long propagations incur additional computational burden not only through the integration cost per sample but also by increasing the required number of samples to resolve the ever more detailed map features that develop as the horizon is extended. This is mitigated somewhat by the continual shrinking of safe regions, but would nonetheless require an increase in the initial sample size in order to provide a sufficiently accurate starting point for the adaptive refinement process. Domain sizing in terms of both maneuver magnitude and propagation duration thus also relates directly to the effectiveness of the search heuristic, which determines the additional ground that can be covered relative to an exhaustive search of a smaller domain.

Further increases in efficiency might be attainable by using more custom-tailored domain geometries or biased initial sample distributions based upon results of the Keplerian reachability

analysis exercise of Section 3.4 and Appendix B, e.g., inversely proportional to the difference between the osculating periapse radius and the central body mean radius as a predictor of where high complexity will appear. With sufficient boosts in domain specificity and heuristic efficiency, it may even become feasible to search four-dimensional domains in real-time, i.e., timed 3DOF maneuvers. Altogether, the trade-offs between domain pruning by *a priori* assumptions and the generality/versatility of the planner is a crucial aspect to consider when optimizing computational efficiency.

8.2.2   Refinement Scheme and Tuning

A key simplification for improving the refinement heuristic's performance and reducing the required amount of tuning was the shift from edge-wise subdivision to simplex-wise subdivision. This both expanded the amount of information being utilized by the heuristic weighting function of Eq. 4.9 and provided a straightforward way of removing bias from the conversion between a set of mesh elements and the continuous control set. The de-biasing in terms of volume resulted in more consistent behavior of subdivision weight distribution, which is essentially an approximation of the objective function and is used for governing further sampling. After establishing this and additionally allowing individual simplices to be sampled multiple times per refinement cycle, performance at a fixed total sample size became far less sensitive to the sizing of the initial uninformed search and to the number of refinement iterations. Tuning was then focused primarily on the objective-centric factor of the weighting function and its exponent, which applied simulated annealing.

Despite these reductions, the number of influential parameters in the heuristic remains sufficiently large to make tuning a challenge. Tuning for high performance becomes even more difficult when attempting to design a highly generalizable heuristic — which is important as the structure and complexity of reachability maps varies drastically not only between different systems and objectives but even between different initial conditions.

The tuning process could potentially be automated and optimized using a genetic algorithm or other machine learning technique. It could also be altered to reduce total computational cost

by adapting the model fidelity used in different predictions, i.e., using a coarse shape model during initial search and later increasing the vertex count when sampling highly promising regions, perhaps in tandem with the influence of simulated annealing. Further consistency in the subdivision process might also be attained with a more systematic and distribution of sampled control points on the interior of a simplex instead of a probabilistic one.

8.2.3   Implementation and Runtime

Altogether, the level of computational efficiency achieved suggests that the sampling-based planning approach may indeed be feasible for onboard implementation — although plans using detailed models may take several minutes to compute on consumer-grade hardware, they only need to be generated once every few hours. Significant effort was dedicated to consistently reducing runtimes throughout the duration of the project's development, but considerably more efficient implementations are no doubt possible, which could help to counteract the performance hit expected from the reduced clock speeds of typical onboard processors. This uncharacteristically simulation-heavy approach to mission design is furthermore in line with the trend to utilize more computational power and algorithmic techniques in guidance, control, and automation.

It is nonetheless true that onboard computing power is highly limited on spaceflight-qualified hardware and must be shared effectively between many subsystems in order to ensure mission success. Necessary further reduction of the net usage by the planning algorithm may be be difficult, and hard guarantees of convergence times are not possible for most intended applications, though acceptable solutions are generally found early in the refinement process. Unavoidably large CPU burden might potentially be accommodated simply by increasing the Δt_{min} planning parameter to guarantee more available time, but this would have a negative impact on reachability prospects by rendering a larger set of options inadmissible.

Beyond improvements to the software implementation, large performance gains could potentially be obtained by using field programmable gate arrays (FPGAs) or other customized hardware. This approach would be amenable due to the various parallel aspects of the algorithm, such as the

independent propagations of many different trajectories, the simplex-wise calculation of refinement weights, and the facet-wise evaluation of polyhedral gravitation.

8.3   Receding Horizon Planning

The receding-horizon implementation (per Chapter 6) of abstraction-based decision-making essentially re-poses a planning task as a control tracking problem for an abstract output state, whose relationship with the physical state is hidden away in the predictive model and handled separately by the reachability search method. Because the controller functions in a discrete manner, the controlled system can be analyzed as a time-discrete system with the sequence of control epochs as the independent variable. Description of various properties of the controlled system then becomes a simpler matter.

8.3.1   Properties of Controlled System

Stability and convergence are standard properties of interest in control systems, and are often demonstrated with rigorous mathematical proofs. In RHC, the notion of recursive feasibility is a prerequisite for these; the controller must not take the system to a state at the current horizon only to find during the next horizon that long-term reachability of the goal has been lost. The abstraction-based planner is not amenable to rigorously proving these properties; however, intuitive explanations can be found in support of their empirical demonstration. Recursive feasibility follows naturally from the high degree of phase space connectivity, discussed in Section 8.1.3 — as long as the spacecraft does not get into a situation from which it cannot recover, nearly the entire phase space can be reached with a small number of control inputs. The utilized margins of error and control authority were sufficient for avoiding a single failure scenario in the entirety of the Monte Carlo simulation sets, thus achieving recursive feasibility and stability in practice. Convergence, meanwhile, is not guaranteed but is demonstrated for several planner formulations by their success rate results. Notably, the results of Section 7.1.2 imply that under sufficiently challenging predictive models, all possible solution paths through the n_g-cube goal space will be taken — this is suggestive

of a sort of pseudo-ergodic motion on some manifold of physical space that intersects all goal regions.

Attainment of desired controller properties stemmed from effective tuning of a large set of design parameters, such as those of the reachability mapping routine of Algorithm 1 and the decision function of Eq. 6.7. It also depended upon mission specifications that constrain phase space connectivity of observation regions: region size, quantity, and required accumulation time. Under uncertainty, margins of safety impose further limitations on connectivity, particularly through the minimum re-planning time. Thus, for general instantiations of the type of problem it is unlikely to be rigorously provable that convergence will occur within a finite time span, and extensive re-calibration of heuristic parameters might be required.

Far stronger reachability prospects would be afforded by a multi-horizon search, i.e., predicting outcomes for sequences of two or more control inputs. However as this essentially exponentiates the dimensionality of the control domain by the depth of the search, it is unlikely that a depth of more than two 2DOF inputs could be made numerically feasible. Possibly by using rules to expand only a small subset of samples to greater prediction depths, the additional CPU demands would scale linearly rather than exponentially. A search paradigm of this sort would begin to bear semblance to the highly influential method of Rapid Random Trees.

8.3.2   Decision Function

The prospect heuristic p_h present in the decision function essentially reflects the mission design philosophy of the planner: should the spacecraft stay closer to the body, or further? Maneuver frequently or infrequently? Choose stable or unstable paths? Orbit prograde, polar, or retrograde? Although only a small glimpse of the full heuristic design space has been explored, there is already compelling evidence that such heuristics are necessary for keeping the spacecraft on track to complete its mission. Notably, the results of Section 7.3 suggest that these heuristics are most effective when somewhat decoupled from the choice of maneuver. At low weighting $w_p \ll 1$, the result is that a maneuver is selected based upon maximization of objective progress and then the next planning epoch is designated to minimize the cost-to-go by speeding up subsequent progress. The

degree to which these decisions can be decoupled depends on the nature of the prospect heuristics; e.g., the radius quality heuristic q_a might be satisfied by very large classes of reachable trajectories and thus not influence a choice between two maneuvers linked to that orbit family.

This degeneracy in the decision function could appear to be a double-edged sword; when there is ambiguity about what the absolute best option is, i.e., maxima occur with finite volume, then it is likelier for two separate trials to result in two different decisions. Some prescriptions lead to more wildly varying results than others; for example, because nearly all trajectories cross the x-y plane, use of a latitude heuristic with $l^* = 0°$ is likely to affect only timing and never the choice of maneuver; this is not the case for $l^* = -90°$ since almost no trajectories cross the polar axis. The possibilities for formulating prospect heuristics are endless, and so the results of the completed investigations might not be indicative of the levels of high performance that may be possible. Furthermore, the decision function interacts with the other components of the algorithm, making the study of heuristics extremely difficult — for example, certain formulations might work well only with very long prediction horizons; others may require recalibrating of the reachability search due to their influence on the complexity of how the decision variable fluctuates across the reachable domain.

It is likely that custom-tailoring heuristics to specifc goals could be highly effective, e.g., by conducting backward-propagations from targets to identify regions from which they may be easily reached. This approach would certainly need to simplify the identification of this backward-reachable set by forward-propagated sample spacecraft paths in order to minimize its CPU cost. More general heuristics that have not yet received significant testing are the pursuit or avoidance of sensitive paths, a preference for certain Jacobi energy levels (which can be computed immediately from initial conditions, potentially easing search speed via *a priori* knowledge), or a preference for maximum change in phasing, i.e., true longitude. It might even be possible to retain a list of previous states that provided unpursued opportunities for goal completion, and to return to those states to once again get the unfulfilled objective in sight. Perhaps the most labor-intensive but most promising approach to heuristic design would be to do slow, offline simulations in a full 4D

search domain or even at multi-maneuver depth, pick the best solutions from those, and then apply manifold learning techniques to design heuristics that would have identified the maneuver points without the extra-dimensional knowledge.

8.4   Uncertainty Handling

Because of the high levels of state and model error and dynamical sensitivity characteristic of small body environments, a basic handling of uncertainty was paramount for demonstrating the potential of the autonomous planning algorithm. Results in Section 7.2 demonstrated that robust predictions, as described in Section 2.2.3.1, and reactive execution, as formulated in Section 6.5.2, were a versatile combination for negating varying levels of error.

8.4.1   Error Levels

Uncertainty mitigation results appeared highly promising for the types and levels of error modeled; under appropriate planner settings, reasonable performance could be obtained under uncharacteristically large state errors. It is implicated that the methods may then scale well to bodies with other sizes and densities, where the proportional influence of state estimate errors would have different consequences for uncertainty growth. Model error also appears possible to address in the planning scheme — even the especially irregularly shaped Comet 67/P could be modeled sufficiently accurately with a low-resolution polyhedron. The surprisingly small influence of this shape modeling error can likely be attributed to its rather stochastic nature.

Reality could, however, vary from the test case scenario in ways that are not so easy to extrapolate. Navigation errors may be smaller in proportion to nominal state values at larger bodies, but there could also be significantly reduced control authority depending on the fuel limitations of the mission. This would in turn reduce robust phase space connectivity and require more restrictive safety margins in order to ensure recursive feasibility. At smaller bodies, the proportionally stronger effects of navigation errors could begin to invalidate the assumption of linear error growth and trigger reactive planning more frequently than is desirable. Lastly, far more detrimental varieties

of model uncertainty might occur in real systems. Inhomogeneity of the central body's mass distribution is suspected to be likely in the case of rubble pile asteroids or porous comets, and could produce more systematic error than an inexact representation of the surface shape that nonetheless retains the correct center of mass. Some forces such as comet outgassing are also incredibly hard to model accurately; these would either impede the effectiveness of robust plans or perhaps again reduce connectivity by being labeled as keep-out zones out of necessity.

Constant improvement of navigation-related technologies, such as flash lidar, could do much to reduce the level of uncertainty in these missions. Conversely, high uncertainty could at least be leveraged as a computational advantage — reachability maps only need to be resolved to the resolution at which the uncertainty ellipses of sampled points begin to overlap. To provide limited robustness to model errors, the predicted deviation Λ could even be augmented with a third term consisting of a sensitivity matrix relating the expected deviation due to uncertainty in a small selection of model parameters.

8.4.2 Robustness Versus Reactivity

Appropriately balanced robustness and reactivity were found to produce high success rates in batches of full mission trials, although the balancing had to be adjusted based upon the level of state error present; higher error necessitates an increased reliance upon reactivity. Very low robustness implies that the spacecraft will replan as soon as possible, while high robustness implies replanning after it has reached the manifold defined by the prospect heuristic, thus aiding long-term performance. As long as sufficient reachability prospects can be maintained, robustness is prefarable to reactivity from an operational point of view: executing maneuvers at nominally planned epochs, rather than reactively, affords more stringent control over the next cycle's prospects and potentially increases the predictability of planner behavior. Furthermore, infrequent maneuvers translate to longer ballistic arcs, which provide better data for state and model estimation. This would also reduce usage of limited onboard operational resources such as processing power and pointing requirements, thus imposing less restriction on science instrument operations.

Because reactivity essentially serves as a safety net to cope with the limitations of robustness, the true hard bounds on spacecraft abilities come from its ability to react. This might be impeded when frequent correction maneuvers cause runaway growth in the state estimate, or when plan formulation time is too long relative to the error growth rate. More frequent use of computing resources would also be required in this case, and computational search demands per maneuver also increase — since the craft is essentially computing reachability of goals that it might be able to attain with a couple more correction maneuvers along the way, higher resolutions and longer propagation times are needed.

Reachability limitations in highly-robust plans might be alleviated through a re-balancing of terms in the decision function, particularly the relative weighting of near-term reachability prospects $\vec{Q}$ and generic reachability prospects p_h. This would blend the low maneuver frequency of robust planning with the far-sightedness of reactive planning. Such a formulation might be most appropriate for smaller and less dense celestial bodies, where a given level of velocity error is larger in proportion to orbital speeds, or for a spacecraft with decreased navigation abilities or imprecise propulsion systems — scenarios where robustly reaching a goal with a single maneuver is very unlikely. Finally, occurrences of unnecessary reactive re-planning might be avoided by more careful utilization of divergence information. The goal-region-shrinking method of robust planning assumes deviations are both in the worst-case direction and at the worst-case magnitude. However, during online execution, single propagations of the continuously estimated trajectory could be checked to verify whether the specific realization of uncertainty actually causes a miss of the target; if not, no correction burn is necessary.

8.5   Summary and Conclusions

This dissertation has provided the development and proof-of-concept demonstration of a new autonomous online mission design scheme based on abstraction of mission objectives and intended to allow ambitious operations and increased science returns in challenging small body systems. Feasibility aspects addressed included navigation and modeling errors, limited frequency of con-

trol cycles, and computational cost: through adaptive mapping, abstract reachability analysis was performed at a level of speed, detail, and sophistication indicative that realtime onboard implementation could be achievable. Prospect heuristics were demonstrated to serve as an equivalent of cost-to-go functions that leveraged the phase space connectivity of orbital systems to make receding-horizon planning an effective approach. All of these components working in concert were shown to successfully and consistently generate mission profiles that fulfilled sets of challenging observation goals at very close proximity to highly irregular objects, while minimizing total duration or fuel consumption and mitigating uncertainty. The rising trend of using increasingly sophisticated computational and algorithmic approaches to provide previously unattainable abilities and levels of performance in guidance and control of fast dynamic systems has thus been extended to the novel scenario of small body mission design.

Bibliography

[1] Miller, J., Konopliv, A., Antreasian, P., Bordi, J., Chesley, S., Helfrich, C., Owen, W., Wang, T., Williams, B., Yeomans, D., et al., "Determination of shape, gravity, and rotational state of asteroid 433 Eros," Icarus, Vol. 155, No. 1, 2002, pp. 3–17.

[2] Yoshimitsu, T., Kawaguchi, J., Hashimoto, T., Kubota, T., Uo, M., Morita, H., and Shirakawa, K., "Hayabusa-final autonomous descent and landing based on target marker tracking," Acta Astronautica, Vol. 65, No. 5, 2009, pp. 657–665.

[3] Ulamec, S., Biele, J., Gaudon, P., Salatti, M., Maibaum, M., Geurts, K., Fantinati, C., Lommatsch, V., Jurado, E., and Moussi-Soffys, A., "Philae: First Landing on a Comet," Lunar and Planetary Science Conference, Vol. 46, 2015, p. 1121.

[4] Michel, P., Cheng, A., Carnelli, I., A. Rivkin, C., Galvez, A., Ulamec, S., and Reed, C., "AIDA: Asteroid Impact and Deflection Assessment Mission Under Study at ESA and NASA," Spacecraft Reconnaissance of Asteroid and Comet Interiors, Vol. 1829 of LPI Contributions, Jan. 2015, p. 6008.

[5] Russell, R. P., "Survey of Spacecraft Trajectory Design in Strongly Perturbed Environments," Journal of Guidance, Control, and Dynamics, Vol. 35, No. 3, 2012, pp. 705–720.

[6] Scheeres, D. J., Orbital Motion in Strongly Perturbed Environments, chap. 2, Praxis Springer, 2012.

[7] Dunham, D. W., Farquhar, R. W., McAdams, J. V., Holdridge, M., Nelson, R., Whittenburg, K., Antreasian, P., Chesley, S., Helfrich, C., Owen, W. M., Williams, B., Veverka, J., and Harch, A., "Implementation of the First Asteroid Landing," Icarus, Vol. 159, No. 2, 2002, pp. 433–438.

[8] Berry, K., Sutter, B., May, A., Williams, K., Barbee, B. W., Beckman, M., and Williams, B., "OSIRIS-REx Touch-And-Go (TAG) Mission Design and Analysis," Proceedings of the 36th Annual AAS Guidance and Control Conference, February 2013.

[9] Wallace, M., Parker, J., Strange, N., and Grebow, D., "Orbital Operations for Phobos and Deimos Exploration," AIAA/AAS Astrodynamics Specialist Conference, Aug. 2012.

[10] Wood, L. J., Bhaskaran, S., Border, J. S., Byrnes, D. V., Cangahuala, L. A., Ely, T. A., Folkner, W. M., Naudet, C. J., Owen, W. M., Riedel, J. E., Sims, J. A., and Wilson, R. S., "Guidance, Navigation, and Control Technology Assessment for Future Planetary Science Missions, Part 1: Onboard and Ground Navigation and Mission Design," Tech. rep., Strategic Missions and Advanced Concepts Office, NASA JPL, October 2012.

[11] Quadrelli, M. B., Wood, L. J., Riedel, J. E., McHenry, M. C., Aung, M., Cangahuala, L. A., Volpe, R. A., Beauchamp, P. M., and Cutts, J. A., "Guidance, Navigation, and Control Technology Assessment for Future Planetary Science Missions," Journal of Guidance, Control, and Dynamics, Vol. 38, No. 7, May 2015, pp. 1165–1186.

[12] Starek, J. A., Aikmese, B., Nesnas, I. A., and Pavone, M., Spacecraft Autonomy Challenges for Next-Generation Space Missions, Vol. 460 of Lecture Notes in Control and Information Sciences, Springer Berlin Heidelberg, 2016, pp. 1–48.

[13] Yoshimitsu, T., Kubota, T., and Nakatani, I., "MINERVA rover which became a small artificial solar satellite," Proceedings of the 20th Annual AIAA/USU Conference on Small Satellites, 2006.

[14] Thompson, D. R., Castillo-Rogez, J. C., Chien, S. A., Doyle, R., Estlin, T., and McLaren, D., "Agile science operations: a new approach for primitive bodies exploration," Proceedings of the SpaceOps 2012 Conference, AIAA, 06 2012.

[15] Lu, P., Cerimele, C. J., Tigges, M. A., and Matz, D. A., "Optimal Aerocapture Guidance," Journal of Guidance, Control, and Dynamics, Vol. 38, No. 4, 2015, pp. 553–565.

[16] Lu, P., Brunner, C., Stachowiak, S., Mendeck, G. F., Tigges, M., and Cerimele, C., "Verification of a Fully Numerical Entry Guidance Algorithm," AIAA Guidance, Navigation, and Control Conference, 2016, p. 0377.

[17] Pinson, R. and Lu, P., "Rapid Generation of Optimal Asteroid Powered Descent Trajectories Via Convex Optimization," Proceedings of the AAS/AIAA Astrodynamics Specialist Conference, No. 15-616, Vail, CO, August 2015.

[18] Wibben, D. R. and Furfaro, R., "Terminal Guidance for Lunar Landing and Retargeting Using a Hybrid Control Strategy," Journal of Guidance, Control, and Dynamics, 2016, pp. 1168–1174.

[19] de Bruijn, F. J., Theil, S., Choukroun, D., and Gill, E., "Geostationary Satellite Station-Keeping Using Convex Optimization," Journal of Guidance, Control, and Dynamics, 2015, pp. 1–12.

[20] Mayne, D. Q., "Model predictive control: Recent developments and future promise," Automatica, Vol. 50, No. 12, 2014, pp. 2967–2986.

[21] Lapierre, L., "Robust diving control of an AUV," Ocean Engineering, Vol. 36, No. 1, 2009, pp. 92 – 104, Autonomous Underwater Vehicles.

[22] Lee, D., Longo, S., and Kerrigan, E. C., "Predictive control for soaring of unpowered autonomous UAVs," Proceedings of the IFAC Conference on Nonlinear Model Predictive Control, Vol. 4, 2012, pp. 194–199.

[23] Starek, J. A. and Kolmanovsky, I. V., "Nonlinear model predictive control strategy for low thrust spacecraft missions," Optimal Control Applications and Methods, Vol. 35, No. 1, 2014, pp. 1–20.

[24] Carson, J. and Acikmese, B., "A Model-Predictive Control Technique with Guaranteed Resolvability and Required Thruster Silent Times for Small-Body Proximity Operations," AIAA

Guidance, Navigation, and Control Conference and Exhibit, Guidance, Navigation, and Control and Co-located Conferences, American Institute of Aeronautics and Astronautics, Aug. 2006.

[25] Morgan, D., Chung, S.-J., and Hadaegh, F. Y., "Model predictive control of swarms of spacecraft using sequential convex programming," Journal of Guidance, Control, and Dynamics, Vol. 37, No. 6, 2014, pp. 1725–1740.

[26] Gavilan, F., Vazquez, R., and Camacho, E. F., "Chance-constrained model predictive control for spacecraft rendezvous with disturbance estimation," Control Engineering Practice, Vol. 20, No. 2, 2012, pp. 111 – 122.

[27] Mayne, D. Q., Kerrigan, E. C., van Wyk, E. J., and Falugi, P., "Tube-based robust nonlinear model predictive control," International Journal of Robust and Nonlinear Control, Vol. 21, No. 11, 2011, pp. 1341–1353.

[28] Lavalle, S. M., Planning Algorithms, chap. II.5, Cambridge University Press, 2006.

[29] Goerzer, C., Kong, Z., and Mettler, B., "A Survey of Motion Planning Algorithms from the Perspective of Autonomous UAV Guidance," Journal of Intelligent and Robotic Systems, Vol. 57, 2010, pp. 65–100.

[30] Du Toit, N. E. and Burdick, J. W., "Robot motion planning in dynamic, uncertain environments," IEEE Transactions on Robotics, Vol. 28, No. 1, 2012, pp. 101–115.

[31] Aoude, G., Luders, B., Joseph, J., Roy, N., and How, J., "Probabilistically safe motion planning to avoid dynamic obstacles with uncertain motion patterns," Autonomous Robots, Vol. 35, No. 1, 2013, pp. 51–76.

[32] Wongpiromsarn, T., Topcu, U., and Murray, R., "Receding Horizon Temporal Logic Planning," IEEE Transactions on Automatic Control, Vol. 57, No. 11, November 2012, pp. 2817–2830.

[33] Rawlings, J. B., Angeli, D., and Bates, C. N., "Fundamentals of economic model predictive control," Proceedings of the IEEE Conference on Decision and Control, 2012, pp. 3851–3861.

[34] Belta, C. and Kumar, V., "Abstraction and control for groups of robots," IEEE Transactions on Robotics, Vol. 20, No. 5, 2004, pp. 865–875.

[35] Chakrabarty, A. and Langelaan, J. W., "Energy-Based Long-Range Path Planning for Soaring-Capable Unmanned Aerial Vehicles," Journal of Guidance, Control, and Dynamics, Vol. 34, No. 4, July–August 2011, pp. 1002–1015.

[36] Nguyen, J., Lawrence, N., Fitch, R., and Sukkarieh, S., "Energy-Constrained Motion Planning for Information Gathering with Autonomous Aerial Soaring," IEEE International Conference on Robotics and Automation, May 2013, pp. 3825–3831.

[37] Parker, J. S. and Anderson, R. L., Low-Energy Lunar Trajectory Design, chap. 2, Wiley, 2014.

[38] Tsirogiannis, G. A. and Davis, K. E., "A two-level perturbation method for connecting unstable periodic orbits with low fuel cost and short time of flight: application to a lunar observation mission," Celestial Mechanics and Dynamical Astronomy, 2016, pp. 1–21.

[39] Dellnitz, M., Junge, O., Post, M., and Thiere, B., "On target for Venus — set oriented computation of energy efficient low thrust trajectories," Celestial Mechanics and Dynamical Astronomy, Vol. 95, 2006, pp. 357–370.

[40] Hennes, D. and Izzo, D., "Interplanetary trajectory planning with Monte Carlo tree search," Proceedings of the 24th International Conference on Artificial Intelligence, AAAI Press, 2015, pp. 769–775.

[41] Englander, J. A., Conway, B. A., and Williams, T., "Automated mission planning via evolutionary algorithms," Journal of Guidance, Control, and Dynamics, Vol. 35, No. 6, 2012, pp. 1878–1887.

[42] Noton, M., "Orbital strategies around a comet by means of a genetic algorithm," Journal of Guidance, Control, and Dynamics, Vol. 18, No. 5, 1995, pp. 1217–1220.

[43] Tsirogiannis, G. A. and Markellos, V. V., "A greedy global search algorithm for connecting unstable periodic orbits with low energy cost," Celestial Mechanics and Dynamical Astronomy, Vol. 117, No. 2, 2013, pp. 201–213.

[44] Tsirogiannis, G. A., "A graph based methodology for mission design," Celestial Mechanics and Dynamical Astronomy, Vol. 114, No. 4, 2012, pp. 353–363.

[45] Trumbauer, E. and Villac, B., "Heuristic Search-Based Framework for Onboard Trajectory Redesign," Journal of Guidance, Control, and Dynamics, Vol. 37, No. 1, 2014, pp. 164–175.

[46] Tardivel, S. and Scheeres, D. J., "Ballistic deployment of science packages on binary asteroids," Journal of Guidance, Control, and Dynamics, Vol. 36, No. 3, 2013, pp. 700–709.

[47] Villac, B., "Using FLI maps for preliminary spacecraft trajectory design in multi-body environments," Celestial Mechanics and Dynamical Astronomy, Vol. 102, No. 1-3, 2008, pp. 29–48.

[48] Komendera, E. E., Scheeres, D. J., and Bradley, E., "Intelligent Computation of Reachability Sets for Space Missions," Proceedings of the 24th Conference on Innovative Applications of Artificial Intelligence, Toronto, July 2012.

[49] Nakhjiri, N. and Villac, B., "Automated stable region generation, detection, and representation for applications to mission design," Celestial Mechanics and Dynamical Astronomy, Vol. 123, No. 1, 2015, pp. 63–83.

[50] Dellnitz, M., Junge, O., Koon, W. S., Lekien, F., Lo, M. W., Marsden, J. E., Padberg, K., Preis, R., Ross, S. D., and Thiere, B., "Transport in Dynamical Astronomy and Multibody Problems," International Journal of Bifurcation and Chaos, Vol. 15, No. 3, 2005, pp. 699–727.

[51] Utku, A., Hagen, L., and Palmer, P., "Initial condition maps of subsets of the circular restricted three-body problem phase space," Celestial Mechanics and Dynamical Astronomy, Vol. 123, No. 4, 2015, pp. 387–410.

[52] Komendera, E., Garland, J., Bradley, E., and Scheeres, D., "Efficiently evaluating reachable sets in the circular restricted 3-body problem," IEEE Transactions on Aerospace and Electronic Systems, Vol. 51, No. 1, January 2015, pp. 454–467.

[53] Vinh, N. X., Gilbert, E. G., Howe, R. M., Sheu, D., and Lu, P., "Reachable Domain for Interception at Hyperbolic Speeds," Acta Astronautica, Vol. 35, No. 1, 1995, pp. 1–8.

[54] Xue, D., Li, J., Baoyin, H., and Jiang, F., "Reachable Domain for Spacecraft with a Single Impulse," Journal of Guidance, Control, and Dynamics, Vol. 33, No. 3, May-June 2010, pp. 934–942.

[55] Zhang, G., Cao, X., and Ma, G., "Reachable domain of spacecraft with a single tangent impulse considering trajectory safety," Acta Astronautica, Vol. 91, 2013, pp. 228–236.

[56] Wen, C., Zhao, Y., Shi, P., and Hao, Z., "Orbital Accessibility Problem for Spacecraft with a Single Impulse," Journal of Guidance, Control, and Dynamics, Vol. 37, No. 4, 2014, pp. 1260–1271.

[57] Holzinger, M. J. and Scheeres, D. J., "Reachability results for nonlinear systems with ellipsoidal initial sets," Aerospace and Electronic Systems, IEEE Transactions on, Vol. 48, No. 2, 2012, pp. 1583–1600.

[58] Branicky, M. S., Curtiss, M. M., Levine, J., and Morgan, S., "Sampling-based reachability algorithms for control and verification of complex systems," Proc. Thirteenth Yale Workshop on Adaptive and Learning Systems, New Haven, CT, 30 May-1, 2005, pp. 244452–008.

[59] Elbanhawi, M. and Simic, M., "Sampling-based robot motion planning: A review," Access, IEEE, Vol. 2, 2014, pp. 56–77.

[60] Komendera, E., Bradley, E., and Scheeres, D. J., "Efficiently Locating Impact and Escape Scenarios in Spacecraft Reachability Sets," AIAA/AAS Astrodynamics Specialist Conference, Guidance, Navigation, and Control and Co-located Conferences, American Institute of Aeronautics and Astronautics, Aug. 2012.

[61] Surovik, D. A. and Scheeres, D. J., "Adaptive Reachability Analysis to Achieve Mission Objectives in Strongly Non-Keplerian Systems," Journal of Guidance, Control, and Dynamics, Vol. 38, No. 3, 2015, pp. 468–477.

[62] Surovik, D. A. and Scheeres, D. J., "Non-Keplerian Trajectory Planning via Heuristic-Guided Objective Reachability Analysis," Proceedings of the 6th International Conference on Astrodynamics Tools and Techniques, No. 08-03, Darmstadt, Germany, 2016.

[63] Surovik, D. A. and Scheeres, D. J., "Heuristic Search and Receding-Horizon Planning in Complex Spacecraft Orbit Domains," Proceedings of the International Conference on Automated Planning and Scheduling, Association for the Advancement of Artificial Intelligence Press, 2015/06/07 2015.

[64] Surovik, D. A. and Scheeres, D. J., "Planning Payload Deployment to Small Bodies via Reachability Analysis," Proceedings of the 30th International Symposium on Space Technology and Science, No. 2015-d-28, Kobe City, Japan, 2015.

[65] Surovik, D. and Scheeres, D. J., "Autonomous maneuver planning at small bodies via mission objective reachability analysis," Proceedings of the AIAA/AAS Astrodynamics Specialist Conference, No. 2014-4147, San Diego, CA, 2014.

[66] Surovik, D. A. and Scheeres, D. J., "Reactive and Robust Paradigms for Autonomous Mission Design at Small Bodies," Proceedings of the AAS/AIAA Astrodynamics Specialist Conference, No. 16-412, Napa, CA, 2016.

[67] Surovik, D. A. and Scheeres, D. J., "Abstraction Predictive Control for Chaotic Spacecraft Orbit Design," IFAC Conference on Nonlinear Model Predictive Control, Vol. 48, No. 23, 2015, pp. 178–184.

[68] Broschart, S. B. and Scheeres, D. J., "Boundedness of spacecraft hovering under dead-band control in time-invariant systems," Journal of guidance, control, and dynamics, Vol. 30, No. 2, 2007, pp. 601–610.

[69] Gaudet, B. and Furfaro, R., "Robust Spacecraft Hovering Near Small Bodies in Environments with Unknown Dynamics Using Reinforcement Learning," AIAA/AAS Astrodynamics Specialist Conference, 2012.

[70] Lee, D., Sanyal, A. K., Butcher, E. A., and Scheeres, D. J., "Almost global asymptotic tracking control for spacecraft body-fixed hovering over an asteroid," Aerospace Science and Technology, , No. 0, 2014, pp. –.

[71] Wallace, M. S. and Broschart, S., "Circular-orbit maintenance strategies for primitive body orbiters," Advances in the Astronautical Sciences, Vol. 150, 2013.

[72] Guelman, M., "Closed-Loop Control of Close Orbits Around Asteroids," Journal of Guidance, Control, and Dynamics, 2014.

[73] Prendergast, K. H., "The Effects of Imperfect Elasticity in Problems of Celestial Mechanics," The Astronomical Journal, Vol. 63, No. 1264, 1958, pp. 412–415.

[74] Press, W. H., Teukolsky, S. A., Vetterling, W. T., and Flannery, B. P., Numerical Recipes 3rd Edition: The Art of Scientific Computing, Cambridge University Press, New York, NY, USA, 3rd ed., 2007.

[75] Gil, P. J. S. and Schwartz, J., "Simulations of Quasi-Satellite Orbits Around Phobos," Journal of Guidance, Control, and Dynamics, Vol. 33, No. 3, May-June 2010, pp. 901–914.

[76] Bradley, E., "Autonomous exploration and control of chaotic systems," Cybernetics and System, Vol. 26, No. 5, 1995, pp. 499–519.

Appendix A

Gravity Models

The two gravity models utilized in the predictive dynamical model are adapted directly from [6].

A.1   Triaxial Ellipsoid

The ellipsoid's principal radii α, β, and γ are stored in decreasing order in the set $\varrho = \{\alpha, \beta, \gamma\}$. Two key quantities are first defined:

$$\phi\left(\mathbf{r}, u\right) = \frac{x^2}{\alpha^2 + u} + \frac{y^2}{\beta^2 + u} + \frac{z^2}{\gamma^2 + u} - 1$$

$$\Delta(u) = \sqrt{\left(\alpha^2 + u\right)\left(\beta^2 + u\right)\left(\gamma^2 + u\right)}$$

Next, the value $\lambda\left(\mathbf{r}\right)$ is computed as the largest real root of $\phi\left(\mathbf{r}, \lambda\right) = 0$ via Newton-Raphson iteration. Iteration counts needed for convergence are reduced by using prior time step's results as initial guesses.

The body-frame expressions for gravitational potential U and its first and second derivatives

with respect to position elements are

$$U(\mathbf{r}) = -\frac{3}{4}\mu \int_{\lambda(\mathbf{r})}^{\infty} \phi(\mathbf{r}, u) \frac{\mathrm{d}u}{\Delta(u)}$$

$$U_{r_i} = -\frac{3}{2}\mu r_i \int_{\lambda(\mathbf{r})}^{\infty} \frac{\mathrm{d}u}{\left(\varrho_i^2 + u\right) \Delta(u)}$$

$$U_{r_i r_i} = -\frac{3}{2}\mu \int_{\lambda(\mathbf{r})}^{\infty} \frac{\mathrm{d}u}{\left(\varrho_i^2 + u\right) \Delta(u)} + \frac{3\mu r_i^2}{\left(\varrho_i^2 + \lambda\right)^2 \Delta(\lambda)} \bigg/ \left[\frac{x^2}{(\alpha^2 + \lambda)^2} + \frac{y^2}{(\beta^2 + \lambda)^2} + \frac{z^2}{(\gamma^2 + \lambda)^2}\right]$$

$$U_{r_i r_{j \neq i}} = -\frac{3\mu r_i r_j}{\left(\varrho_i^2 + \lambda\right)\left(\varrho_j^2 + \lambda\right) \Delta(\lambda)} \bigg/ \left[\frac{x^2}{(\alpha^2 + \lambda)^2} + \frac{y^2}{(\beta^2 + \lambda)^2} + \frac{z^2}{(\gamma^2 + \lambda)^2}\right]$$

Numerical implementation of the potential and its derivatives employs two algorithms from [74] to calculate Carlson's elliptic integrals of the first and second kinds, which have the respective forms

$$R_F(a, b, c) = \frac{1}{2} \int_0^{\infty} \frac{\mathrm{d}u}{\sqrt{(a + u)(b + u)(c + u)}}$$

$$R_D(a, b, c) = \frac{3}{2} \int_0^{\infty} \frac{\mathrm{d}u}{(c + u)\sqrt{(a + u)(b + u)(c + u)}}$$

To convert the integral expressions of U_{r_i} into the form of R_D, $v = u - \lambda$ and $\mathrm{d}v = \mathrm{d}u$ are substituted and a new set of arguments derived from the ellipsoid of axes are used

$$U_{r_i} = -\mu r_i \frac{3}{2} \int_{\underset{v(u=\lambda) \to 0}{\overset{v(u=\infty) \to \infty}{}}} \frac{\mathrm{d}v}{\left(\varrho_i^2 + v + \lambda\right) \Delta(v + \lambda)}$$

$$\varrho_i' = \varrho_i^2 + \lambda$$

$$U_{r_i} = -\mu r_i R_D\left(\varrho_j', \varrho_k', \varrho_i'\right)$$

The potential itself can be expressed in terms of R_D and R_F using the same substitution

$$U = -\frac{1}{2}\mu \left[x^2 R_D\left(\beta', \gamma', \alpha'\right) + y^2 R_D\left(\gamma', \alpha', \beta'\right) + z^2 R_D\left(\alpha', \beta', \gamma'\right) - 3R_F\left(\alpha', \beta', \gamma'\right)\right]$$

And lastly, the Jacobian of the potential is computed using a vector $\mathbf{c}$ that scales the position by the modified ellipsoid axes

$$\mathbf{c} = \begin{bmatrix} \frac{x}{\alpha'} & \frac{y}{\beta'} & \frac{z}{\gamma'} \end{bmatrix}^T$$

$$\nabla^2 U = -\begin{bmatrix} U_x/x & 0 & 0 \\ 0 & U_y/y & 0 \\ 0 & 0 & U_z/z \end{bmatrix} + \frac{3\mu}{\mathbf{c}^T \mathbf{c}\sqrt{\alpha'\beta'\gamma'}} \left[\mathbf{c}\mathbf{c}^T\right]$$

A.2   Polyhedron

First, 3x3 projection matrices are defined for each edge e and face f using normal unit vectors $\hat{\mathbf{n}}$; computations for edge matrices depend on the normals of both adjacent faces f and f'.

$$\mathbf{E}_e = \hat{\mathbf{n}}_f \hat{\mathbf{n}}_e^f + \hat{\mathbf{n}}_{f'} \hat{\mathbf{n}}_e^{f'} \tag{A.1}$$

$$\mathbf{F}_f = \hat{\mathbf{n}}_f \hat{\mathbf{n}}_f \tag{A.2}$$

Because these matrices do not depend on the spacecraft position, they are precomputed and stored. Gravitation evaluations during propagation begin with the computation of two scalar terms:

$$L_e = \ln \frac{r_1^e + r_2^e + |\mathbf{r}_1^e - \mathbf{r}_2^e|}{r_1^e + r_2^e - |\mathbf{r}_1^e - \mathbf{r}_2^e|} \tag{A.3}$$

$$\varpi_f = 2 \arctan \frac{\mathbf{r}_1^f \cdot \tilde{\mathbf{r}}_2^f \cdot \mathbf{r}_3^f}{r_1^f r_2^f r_3^f + r_1^f \mathbf{r}_2^f \cdot \mathbf{r}_3^f + r_2^f \mathbf{r}_e^f \cdot \mathbf{r}_1^f + r_3^f \mathbf{r}_1^f \cdot \mathbf{r}_2^f} \tag{A.4}$$

The gravitational potential, acceleration, and Hessian are then obtained in terms of summations across polyhedron elements:

$$U(\mathbf{r}) = \frac{\mathcal{G}\sigma}{2} \left[\sum_{e \in \text{edges}} \mathbf{r}_e \cdot \mathbf{E}_e \cdot \mathbf{r}_e L_e - \sum_{f \in \text{faces}} \mathbf{r}_f \cdot \mathbf{F}_f \cdot \mathbf{r}_f \varpi_f \right] \tag{A.5}$$

$$\frac{\partial U}{\partial \mathbf{r}} = -\mathcal{G}\sigma \left[\sum_{e \in \text{edges}} \mathbf{E}_e \cdot \mathbf{r}_e L_e - \sum_{f \in \text{faces}} \mathbf{F}_f \cdot \mathbf{r}_f \varpi_f \right] \tag{A.6}$$

$$\frac{\partial^2 U}{\partial \mathbf{r}^2} = \mathcal{G}\sigma \left[\sum_{e \in \text{edges}} \mathbf{E}_e L_e - \sum_{f \in \text{faces}} \mathbf{F}_f \varpi_f \right] \tag{A.7}$$

During this summation, the minimal range $\rho_{\mathcal{P}}$ is also checked. Additionally, the Laplacian is computed for use in detecting impact

$$\nabla^2 U = -\mathcal{G}\sigma \sum_{f \in \text{faces}} \varpi_f \tag{A.8}$$

This quantity evaluates to 0 for positions exterior to the surface, or 4π for interior ones.

Appendix B

Keplerian Reachability

B.1   Keplerian element level sets

For repeated reachability-based maneuver planning, it is desired to map both the direct outcomes of each maneuver as well as the dynamical characteristics of the associated orbit. For a planar Keplerian system, only three parameters are required to describe the reached orbit: semimajor axis a, eccentricity e, and argument of perigee ω. Orbit inclination and right ascension are zero and undefined, respectively, while the true anomaly f at the time of the maneuver is redundant with the description of ω relative to the $\hat{\mathbf{x}}$ direction.

By normalizing the standard two-body energy equation by $2/v_{lc}^2$, the kinetic energy of a circular orbit at the initial radius r, we obtain an expression of the ratio between initial radius r and semimajor axis a in terms of the normalized velocity magnitude ν.

$$
\begin{aligned}
E &= \frac{v^2}{2} - \frac{\mu}{r} = -\frac{\mu}{2a} \\
E' &= \nu^2 - 2 = -\frac{r}{a} \\
r/a &= 2 - \nu^2
\end{aligned}
\tag{B.1}
$$

The normalized semimajor axis depends only on velocity magnitude and not upon flight path angle. Velocity-space level curves of a/r must therefore appear as concentric circles about the origin, with values of $1/2 \leq a/r < \infty$ for $0 \leq \nu < \sqrt{2}$, $a/r = \infty$ for $\nu = \sqrt{2}$, and $a/r < 0$ for $\nu > \sqrt{2}$. By computing the velocity magnitudes that correspond to these ranges of a/r we obtain the level curves plotted in Figure 3.2(a).

First find the semilatus rectum (normalized by semimajor axis) with the help of Equation B.1

$$
\begin{aligned}
p/a =& H^2/\left(\mu a\right) \\
=& \left(rv\cos\gamma\right)^2/\left(\mu a\right) \\
=& \left(\frac{r}{a}\right)\frac{r}{\mu}v^2\cos^2\gamma \\
=& \left(2-v^2\right)v^2\cos^2\gamma
\end{aligned}
\tag{B.2}
$$

This leads directly to the eccentricity e

$$
\begin{aligned}
e =& \sqrt{1-p/a} \\
=& \sqrt{1-\left(2-v^2\right)v^2\cos^2\gamma}
\end{aligned}
\tag{B.3}
$$

Level curves are obtained by solving for $\nu_x = \nu\sin\gamma$ in terms of $\nu_y = \nu\cos\gamma$ for a specified value of e. These are plotted in Figure 3.2(b).

$$
\begin{aligned}
1-e^2 =& \left(2-v^2\right)v^2\cos^2\gamma \\
1-e^2 =& 2\nu_y^2 - \nu_x^2\nu_y^2 - \nu_y^4 \\
\nu_x^2\nu_y^2 =& 2\nu_y^2 - \nu_y^4 + e^2 - 1 \\
\nu_x =& \pm\sqrt{2-\nu_y^2+\left(e^2-1\right)/\nu_y^2}
\end{aligned}
\tag{B.4}
$$

We first seek a simplified expression for the true anomaly f with the help of Eqs B.1 and B.2.

$$
\begin{aligned}
\frac{r}{a} =& \frac{p/a}{1+e\cos f} \\
1+e\cos f =& \left(\frac{p}{a}\right)\ \Big|\ /\left(\frac{r}{a}\right) = \frac{p}{r} \\
=& \left[\left(2-v^2\right)v^2\cos^2\gamma\right]/\left(2-v^2\right) = v^2\cos^2\gamma
\end{aligned}
\tag{B.5}
$$

Solving for the true anomaly requires use of inverse cosine, which has the same sign for a given radius regardless of whether the state is outbound from periapse or inbound to periapse. This

missing information can instead be gleaned from the sign of the flight path angle.

$$f = \text{sgn}\left(\gamma\right) \cos^{-1}\left(\frac{\nu^2 \cos^2 \gamma - 1}{e}\right)$$

Since the initial state is located at position $\hat{\mathbf{x}}$, the argument of periapsis ω is simply the negative of the initial state's true anomaly. Level curves of ω are found from first solving Eq B.5 for $e = \left(\nu_y^2 - 1\right) / \cos f$ and then plugging this value into Eq B.4 to obtain $\nu_x\left(-\omega, \nu_y\right)$. However ω only appears in this expression as $\cos^2 \omega$, which is ambiguous with three other angles:

$$\cos^2 \omega = \cos^2\left(-\omega\right) = \cos^2\left(\pi + \omega\right) = \cos^2\left(\pi - \omega\right)$$

Curves generated for $\omega \in [0, 90°]$ thus contained level curves for all four arguments; it was experimentally determined that the corrected value $\omega' \in [0, 360°]$ could be described by:

$$\omega' = -\text{sgn}\left(\nu_x\right)\text{sgn}\left(\nu_y\right)\omega + 180°\left(|\nu_y| < 1\right)$$

Results are shown in Figure 3.3.

B.2   Impact

The two primary criteria for mission failure are escape from and impact of the central body. Escape is straightforwardly detected via energy, corresponding to $\nu \geq \sqrt{2}$ and having no dependence on γ, as was found in the discussion of Section B.1. Development of the impact criterion is less trivial.

Beginning from $r/a = 1 - e \cos E$, we relate the initial conditions to the periapsis radius r_p,

where $r_p = r(E = 0)$ and $\rho = r_p/r$.

$$1 - e = r_p/a$$

$$e^2 = (1 - r_p/a)^2$$

$$\cancel{1} - (r/a)\,\nu^2 \cos^2\gamma = \cancel{1} - 2r_p/a + (r_p/a)^2$$

$$-\cancel{(r/a)}\nu^2 \cos^2\gamma = -2\rho\cancel{(r/a)} + \rho^2\,(r/a)\,\cancel{(r/a)}$$

$$\nu^2 \cos^2\gamma = 2\rho - \rho^2\left(2 - \nu^2\right)$$

$$= 2\rho - 2\rho^2 + \rho^2\nu^2$$

From here, the constraint between ν and γ for given ρ can be easily expressed as a function of either parameter in terms of the other:

$$\nu^2 = 2\left(\frac{\rho - \rho^2}{\cos^2\gamma - \rho^2}\right) \qquad\qquad \cos^2\gamma = \rho^2 + \frac{2}{\nu^2}\left(\rho - \rho^2\right) \qquad\qquad \text{(B.6)}$$

Alternatively, in terms of the velocity components v_x along the radius vector and v_y perpendicular to it,

$$\nu_x^2 = \frac{\rho^2 v_y^2 + 2\left(\rho - \rho^2\right)}{1 - \rho^2} \qquad\qquad \nu_y^2 = \frac{v_x^2\left(1 - \rho^2\right) - 2\left(\rho - \rho^2\right)}{\rho^2}$$

This constraint, which specifies a 1D subset of the 2D velocity space, corresponds to grazing impact when r_p is equal to the radius R of the finite-density central body.

As was seen with the level curves of argument of perigee, the term $\cos^2\gamma$ implies that when γ satisfies the grazing impact constraint for a given pair of periapse radius and velocity magnitude, so will $-\gamma$, $180 + \gamma$, and $180 - \gamma$. These four values correspond to symmetries between inbound/outbound orbit legs and prograde/retrograde orbits.

From the first version of Eq. B.6, we see that when $\gamma = 0$, the denominator is maximized (since $\rho < 1$ for impact detection) and ν is minimized, providing the slowest possible grazing impact. Increasing γ until $\cos^2\gamma = \rho$ causes $\nu^2 - 2 = 0$, which from Eq. B.1 can be seen to correspond to

a parabolic orbit. Further increase implies hyperbolic orbits with grazing-impact. Finally, when $\cos\gamma = \rho$, the denominator reaches zero; this implies that the orbiter travels on a straight line at infinite velocity to graze the central body at position $R\cos\gamma\hat{\mathbf{x}} \pm R\sin\gamma\hat{\mathbf{y}}$, completing a right triangle with hypotenuse length r and opposing side length R.

Begin with the constraint on grazing trajectories, and introduce a constant $\mathcal{I}$.

$$\mathcal{I} = \nu^2 - 2\left(\frac{\rho - \rho^2}{\cos^2\gamma - \rho^2}\right) \tag{B.7}$$

Suppose that (ν, γ) are selected to satisfy $\mathcal{I} = 0$, such that the trajectory grazes the surface. Then consider if ν is decreased slightly; now, the normalized kinetic energy is reduced such that $\mathcal{I} < 0$ and the perigee is slightly reduced to $r_p < R$. Or, if $\cos\gamma$ is decreased toward its limiting value of ρ, this increases the magnitude of the negative term and also causes $\mathcal{I} < 0$; angular momentum is removed from the system causing an increase in eccentricity. Conversely, increasing ν or $\cos\gamma$ causes $\mathcal{I} > 0$ and $r_p > R$. $\mathcal{I}$ can thus be used as a measure of impact, where as values become more negative the impacting orbits have lower and lower periapses.

A velocity-space map of grazing and incident impact is shown in Figure 3.4(a), where level curves represent grazing impact for a specified value of ρ and the shaded interior region represents incident impact for that value. Symmetry about the x axis reflects the equivalence of prograde and retrograde orbits. The level curves are also symmetric about the y axis since the impact criterion evaluates the **conic** of the executed maneuver, which can be reached on either its outbound or inbound leg; to reflect the practical reality that we are only interested in forward-time reachability, outbound trajectories on hyperbolae with $r_p \leq R$ are marked as escaping rather than impacting.

B.3   Impact Properties

A few additional properties of impacting trajectories can be examined. To compute time-to-impact, the mean anomaly M must be found with Kepler's equation after first obtaining the eccentric anomaly E. The sign of γ is used to determine whether motion is inbound or outbound

from periapse.

$$r/a = (1 - e \cos E)$$

$$E = \text{sgn}(\gamma) \cos^{-1} \left[\frac{1}{e} \left(1 - \frac{r}{a} \right) \right]$$

$$M = E - e \sin E$$

These equations can be used to find M for a generic initial state, or by multiplying the quantity r/a by ρ and using $\text{sgn}(\gamma) = -1$ they provide E_{imp} and M_{imp}, which are zero for the case of grazing impact. Time to impact is then

$$t_{imp} = \text{mod}(M_{imp} - M_0, 2\pi)/n \qquad \text{(any impact)}$$

$$t_{per} = \text{mod}(-M_0, 2\pi)/n \qquad \text{(grazing impact)}$$

Due to the complications of Kepler's equation, level curves of time to impact do not have a straightforward analyical expression; numerical results are shown in Figure 3.6(b).

The velocity at impact can be shown to be independent of the initial flight path angle, with level curves occurring at fixed radii from the origin (though whether impact does in fact occur still depends on the flight path angle per Eq. B.7).

$$R/a = \rho r/a$$

$$= 2 - \nu_{imp}^2 = \rho\left(2 - \nu^2\right) \tag{B.8}$$

Impact angle can also be constrained in a manner similar to the grazing impact criterion, through the use of Eqs. B.2 and B.8 and the constancy of p and a for a given conic.

$$\left(2 - \nu^2\right)\nu^2 \cos^2\gamma = \left(2 - \nu_{imp}^2\right)\nu_{imp}^2 \cos^2\gamma_{imp}$$

$$\cancel{\left(2 - \nu^2\right)}\nu^2 \cos^2\gamma = \rho\cancel{\left(2 - \nu^2\right)}\left[2 - \rho\left(2 - \nu^2\right)\right]\cos^2\gamma_{imp}$$

$$= 2\rho\cos^2\gamma_{imp} - 2\rho^2\cos^2\gamma_{imp} + \rho^2\nu^2\cos^2\gamma_{imp}$$

$$\nu^2 = 2\frac{\left(\rho - \rho^2\right)\cos^2\gamma_{imp}}{\cos^2\gamma - \rho^2\cos^2\gamma_{imp}}$$

Level curves of these two properties are shown in Figure 3.4(b).

B.4   Goal Rendezvous

As a simple model of the attainability of position-based mission objectives, reachability is studied for goal points fixed in inertial space. Begin with the equations for the radii r of the initial state and r_1 of the goal position, which has angular displacement θ_1 counterclockwise from the x axis.

$$r = \frac{p}{1 + e \cos f} \qquad\qquad r_1 = \frac{p}{1 + e \cos (f + \theta_1)}$$

Define $\beta_1 = r/r_1$, the inverse normalized radius of the goal state.

$$\beta_1 = \frac{r}{r_1} = \frac{1 + e \cos (f + \theta_1)}{1 + e \cos f}$$

$$\beta_1 + \beta_1 e \cos f = 1 + e \cos (f + \theta_1)$$

$$= 1 + e \cos f \cos \theta_1 - e \sin f \sin \theta_1$$

The flight path angle can be introduced from

$$\tan \gamma = \frac{e \sin f}{1 + e \cos f}$$

Replacing the sine term, the constraint becomes

$$\beta_1 + \beta_1 e \cos f = 1 + e \cos f \cos \theta_1 - [(1 + e \cos f) \tan \gamma] \sin \theta_1$$

$$= 1 + e \cos f \cos \theta_1 - \tan \gamma \sin \theta_1 - e \cos f \tan \gamma \sin \theta_1$$

Collecting in terms of $e \cos f$ and substituting from the radius equation,

$$(\beta_1 - \cos \theta_1 + \tan \gamma \sin \theta_1) e \cos f = 1 - \beta_1 - \tan \gamma \sin \theta_1$$

$$e \cos f = \frac{p}{r} - 1 = -\frac{\tan \gamma \sin \theta_1 + \beta_1 - 1}{\tan \gamma \sin \theta_1 + \beta_1 - \cos \theta_1}$$

Substituting the earlier equation for p/r, we have

$$\nu = \pm \frac{1}{\cos \gamma} \sqrt{1 - \frac{\tan \gamma \sin \theta_1 + \beta_1 - 1}{\tan \gamma \sin \theta_1 + \beta_1 - \cos \theta_1}} \tag{B.9}$$

Which tells us, for a given γ, what velocity magnitude we need in order to travel on the conic containing the point (β_1, θ_1). Level curves of this constraint are plotted in Figure 3.5.